2026-01

Interface and Crystallization Engineering þÿ F o r E f f i c i e n t P b S n M i x e d P e r Solar Cells

Yekitwork, Abebe Temitmie

BAHIR DAR UNIVERSITY

College of Science

Department of Physics

INTERFACE AND CRYSTALLIZATION ENGINEERING FOR EFFICIENT PB–SN MIXED PEROVSKITE SOLAR CELLS

By

Yekitwork Abebe Temitmie

January 2026

BAHIR DAR UNIVERSITY

College of Science

Department of Physics

INTERFACE AND CRYSTALLIZATION ENGINEERING FOR EFFICIENT PB–SN MIXED PEROVSKITE SOLAR CELLS

A dissertation submitted
to
Department of Physics, College of Science in
partial fulfillment for the requirements of the Degree of
Doctor of Philosophy in Applied Condensed Matter Physics

By

Yekitwork Abebe Temitmie

Supervisor: Dr. Amare Benor Belay
Department of Physics
Bahir Dar University, Ethiopia

Co-supervisor: Prof. Dr. Lukas Schmidt-Mende
Department of Physics
University of Konstanz, Germany

January 2026
Bahir Dar, Ethiopia

DECLARATION

The thesis entitled "**Interface and Crystallization Engineering for Efficient Pb–Sn Mixed Perovskite Solar Cells**" is my original work and has been for the degree of Doctor of Philosophy in Applied Condensed Matter Physics at Bahir Dar University, Ethiopia, under the supervision of Dr. Amare Benor and co-supervisor Prof. Dr. Lukas Schmidt-Mende at University of Konstanz, Germany. The work has never been submitted to or presented in any other university, college, or institution. As far as I am aware, the thesis does not include any content previously published or authored by another individual, except where proper references have provided.

Name: Yekitwork Abebe Temitmie

Signature: 

Date: January 2026

BAHIR DAR UNIVERSITY

College of Science

Department of Physics

Approval of the Dissertation for Defense

I hereby certify that I have supervised, read, and evaluated this dissertation entitled "**Interface and Crystallization Engineering for Efficient Pb–Sn Mixed Perovskite Solar Cells**" by Yekitwork Abebe Temitmie, prepared under my guidance. I recommend that the dissertation be submitted for oral defense.

Dr. Amare Benor _____ _____

Supervisor Signature Date

BAHIR DAR UNIVERSITY

College of Science

Department of Physics

Approval of the Dissertation Defense Result

We hereby certify that we have examined Yekitwork Abebe Temitmie's dissertation, "**Interface and Crystallization Engineering for Efficient Pb-Sn Mixed Perovskite Solar Cells**." We recommend and approve the dissertation for the Doctor of Philosophy in Applied Condensed Matter Physics.

Board of Examiners

External Examiner:	---------- Prof. Giso Hahn
External Examiner:	---------- Prof. Belayneh Mesfin
Internal Examiner:	---------- Dr. Getachew Tizazu
Chairman:	---------- Dr. Tamiru Negussie
Supervisor:	---------- Dr. Amare Benor
Co Supervisor :	---------- Prof. Lukas Schmidt-Mende

DEDICATION

Dedicated to my beloved families and friends, who have always believed in me and supported my dreams, for their staunch sacrifices, encouragement, and love. I dedicated this thesis to them.

ACKNOWLEDGEMENTS

First and foremost, I extend my deepest gratitude to my supervisor, Dr. Amare Benor Belay, who has guided me from the very beginning of my doctoral journey. His advice laid the foundation for this thesis, and his support during the early stages, both scientifically and personally, was instrumental in shaping my academic path. I am especially thankful for his encouragement during the transition to international collaboration and for his continued interest in my progress throughout the joint program. His intellectual rigor and patience have profoundly influenced my approach to research and critical thinking.

I am equally and intensely grateful to Prof. Dr. Lukas Schmidt-Mende, my supervisor during my stay at the University of Konstanz, for his invaluable guidance during the German phase of my PhD. His thoughtful feedback, openness to interdisciplinary exploration, and commitment to scientific excellence have significantly enriched this work. I sincerely thank him for welcoming me into his research group and for fostering an environment of intellectual rigor, collaboration, and innovation. I am especially thankful for the generous scholarship opportunity he facilitated and for his wholehearted support, which enabled me to carry out my research in the Hybrid Nanostructures Lab. It was an enriching experience, and I am grateful for the time I spent working with his outstanding team.

Special thanks to Dr. Azhar Fakharuddin for his foundational contributions to this thesis. His unwavering support, encouragement, and dedication, frequently going above and beyond, played an essential part in the success of my experiments. I sincerely appreciate his guidance and generosity throughout this process.

I sincerely acknowledge the substantial support of the International Science Program (ISP, IPPS Eth-03, 2020-2026) in Ethiopia, whose early investment in my academic development laid a strong foundation for my research career and enabled me to pursue advanced studies abroad. I am deeply grateful to the German Academic

Exchange Service (DAAD) and the Deutsche Forschungsgemeinschaft (DFG, German Research Foundation) for their financial support, which sustained my research and enabled me to participate in international conferences.

I would also like to express my sincere gratitude to our technician Marcus Schwamberger**,** whose troubleshooting and technical skills ensured that everything functioned effortlessly, and for his willingness to share his expertise. I extend my heartfelt thanks to Dr. Yenal Yalcinkaya and Dr. Irfan Haider for their meticulous proofreading and invaluable support throughout the preparation of this thesis.

I want to thank all members of the AG Schmidt-Mende research group for their collaborative spirit and scientific support: Daniele T. Cuzzupè, Maria Azhar, Tom Burgard, Emilia Schütz, Nicky, Stefan Schupp, Tim Mayer, Stefan Kraner, Laurenz, Tobias Seewald, Timo Raab, Elias Illing, Serena Piozzi, Ann-Kathrin, Simon Keegan, Maximilian Brochnow, and Max G., and colleagues from Bahir Dar University, Ethiopia: Asaye Gedifew, Biniam Ademe, Tigist Sisay, and Mekdes Mengesha for their friendship, cooperation, and support. Their presence has made the experience scientifically fruitful and personally memorable. I am also profoundly grateful to the staff and colleagues at Debre Markos University, Debre Markos University, and Bahir Dar University in Ethiopia, whose encouragement and contributions have been instrumental throughout my academic journey.

Finally, a heartfelt thank you to my beloved family, my wonderful husband, and my dear friend, Hagerie Fentaw, and her husband, Samson Gizachew, for their care, inspiration, and love throughout my PhD journey.

ABSTRACT

Lead-tin (Pb-Sn) mixed perovskite solar cells (PSCs) enable bandgap tuning (1.1–1.4 eV), reduce toxicity, and offer great potential for efficient all-perovskite tandem devices. Although they exhibit promising optoelectronic properties, Pb–Sn mixed perovskites still face significant challenges that limit their overall device performance. One critical issue is the loss of open-circuit voltage (V_{OC}) due to energy-level misalignment and defects arising from the coexistence of Pb and Sn within the perovskite structure. This energy-level mismatch hinders efficient charge extraction at the interfaces. At the same time, the mixed-metal-induced defects create local variations in the conduction and valence bands, leading to band tailing, bandgap fluctuations, and enhanced non-radiative recombination. Another issue is the rapid formation of the perovskite film, especially the Sn-rich phase, leading to tiny gaps where Pb and Sn atoms should be, thereby creating vacancies. Consequently, the resulting films exhibit poor interface between the perovskite and adjacent transport layers, further promoting recombination. Moreover, uncontrolled and poor crystallization of the perovskite film can create tiny gaps, pinholes, or grain boundaries, which act as shunt pathways. These key factors lead to leakage currents and a reduction in V_{OC}, consequently decreasing overall device efficiency. This thesis aims to address these limitations by using interfacial engineering and controlling crystallization kinetics.

In the first project, we improved the charge transport dynamics of the Pb-Sn perovskite $(FASnI_3)_{0.6}(MAPbI_3)_{0.4}$ using an interface engineering strategy by inserting an ultra-thin layer of poly[bis(4-phenyl)(2,4,6-trimethylphenyl)amine] (PTAA) between the commonly used hole transport layer (HTL) poly(3,4-ethylenedioxythiophene) polystyrene sulfonic acid (PEDOT: PSS) and the Pb-Sn mixed perovskite layer. This selective interfacial material effectively passivates surface defects, aligns more closely with the perovskite's valence band, and thereby enhances charge extraction. As a result, the V_{OC} was substantially improved, reaching 0.82 V, thereby increasing the power conversion efficiency (PCE) to 20.3%.

In the second project, the HTL–perovskite interface was improved by optimizing the PTAA interlayer concentration in single-junction narrow-bandgap (NBG) perovskite solar cells. This work built upon the advancements of the first project to enhance the compatibility of NBG cells within all-perovskite tandem architectures. In these configurations, the NBG sub-cell functions as the bottom cell, where efficient charge extraction and suppressed interfacial recombination are critical for maximizing device performance. By integrating this high-performance NBG cell with a wide-bandgap (WBG) top cell, a monolithic all-perovskite tandem solar cell was realized. Specifically, $Cs_{0.3}FA_{0.6}MA_{0.1}Pb(I_{0.7}Br_{0.3})_3$, which has a bandgap of approximately 1.70 eV—the system was successfully translated into an all-perovskite tandem structure, achieving a V_{OC} exceeding 2.0 V and a PCE of 25.1%.

In the third project, a gas quenching (GQ) approach is introduced as an alternative to conventional anti-solvent (AS) quenching to achieve slower crystallization, smoother perovskite films with fewer pinholes, enhanced V_{OC}, and improved PSC efficiency. The GQ approach resulted in slower crystallization and modified film quality. Devices fabricated using the GQ approach also demonstrated better performance with higher V_{OC} values. Specifically, devices prepared with the AS method achieved a champion PCE of 18.3%, whereas those prepared with the GQ method achieved a higher PCE of 19.1%.

This improvement in efficiency, combined with enhanced reproducibility and the simplicity and environmental friendliness of the GQ approach, underscores its advantages for processing NBG Pb-Sn mixed perovskite films. Therefore, the GQ method holds significant potential for application in the fabrication of NBG Pb-Sn PSCs.

Keywords: All-perovskite Tandem Solar Cells, Crystallization Engineering, Gas-Quenching, Interface Engineering, Pb–Sn Mixed Perovskites.

PUBLICATIONS AND PRESENTATIONS

Publications

Temitmie, Y.A.; Haider, M.I.; Cuzzupè, D.T.; Mercaldo, L.V.; Kraner, S.; Veneri, P.D.; Benor, A.; Fakharuddin, A. and Schmidt-Mende, L. Overcoming the Open-Circuit Voltage Losses in Narrow Bandgap Perovskites for All-Perovskite Tandem Solar Cells. *ACS Materials Letters* 2024, *6*(11), 5190-5198.

Temitmie, Y.A.; Azhar, M; Haider, M.I.; Yalcinkaya, Y.; Schütz, E. R.; Mayer, T.; Benor, A. and Schmidt-Mende, L. Gas Quenching-Mediated Crystallization for Optoelectronic-Grade Pb–Sn Perovskite Films. Solar RRL, 2025, 202500713.

Ademe, B.; **Temitmie, Y.A.**; Tizazu, G.; Abebe, A.; Ulbricht, C.; Hailegnaw, B.; Schöber, M.; Sariciftci, N.S.; Lukas Schmidt-Mende, L.; and Benor, A. Electrochemical Etching of Fluorine Doped Tin Oxide (FTO): Effects on Morphological, Electrical, Physical and Optical Properties. ACS Applied Optical Materials, 2025 (Manuscript Revised After Submission and Invited for Cover Page).

Azhar, M.; Yalcinkaya, Y.; Cuzzupè, D. T.; **Temitmie, Y.A.**; Haider, M. I.; Schmidt Mende, L. Perovskite thin-film solar cells: the gas-quenching method. Materials and Sustainability 2025.

Cuzzupè, D. T.; Franckevi˘cius, M.; Karalis, O.; **Temitmie, Y.A.**; Mar˘cinskas, M.; Azhar, M.; Getautis, V.; Malinauskas, T.; Hempel, H.; Schmidt-Mende, L. Revealing the energy level and charge dynamics interplay in mixed Pb–Sn perovskite solar cells with new phenoxazine and phenothiazine SAMs. Solar RRL, 2025, e202500768.

Ling, J.; Cuzzupè, D.T.; Din, M.F.U.; Stepura, A.; Burgard, T.; **Temitmie, Y.A.**; Majkova, E.; Omastova, M.; Jose, R.; Schmidt-Mende, L. and Fakharuddin, A.

MXene-embedded PEDOT: PSS hole-transport material for lead-free perovskite solar cells. *ACS Applied Energy Materials* 2024, *7*(17), 7152-7158.

Azhar, M.; Cuzzupè D. T.; Yalcinkaya, Y.; Haider, M. I.; Schütz, E. R.; Schupp, S. M.; **Temitmie, Y.A.**; Hooijer, R.; Aydin, E.; Schmidt-Mende, L. Impact of Antisolvent and Gas Quenching on Wrinkling in $Cs_{0.15}FA_{0.85}Pb(I_{0.6}Br_{0.4})_3$ Perovskite Films, ACS *Appl. Mater. Interfaces* 2025, 17, 42, 58501–58511.

Conferences

Sep 2025 SPP 2196 Conference (DFG), Konstanz, Germany: Overcoming the Open-Circuit Voltage Losses in Narrow Bandgap Perovskites for All-Perovskite Tandem Solar Cells (Poster presentation)

Jun 2025 13^{th} Annual Science Conference, Bahir Dar University, Bahir Dar, Ethiopia: Enhancing Open-Circuit Voltage in Narrow Bandgap Perovskites for Efficient All-Perovskite Tandem Solar Cells; (oral presentation)

May 2024 Tandem PV Workshop (DPG), Amsterdam, The Netherlands & online: participation (online attended)

Seminar

Nov 2025 Gas Quenching Technique for Efficient Lead-Tin Mixed Perovskite Solar Cells (oral presentation)

Jul 2024 Effect of Anti-Solvents on Film Quality and Performance of Perovskite Solar Cells (oral presentation)

Mar 2023 Top Passivation Strategies for High-Performance Narrow-Bandgap

Perovskite Solar Cells (oral presentation)

TABLE OF CONTENTS

LIST OF TABLES

LIST OF FIGURES

ACRONYMS AND SYMBOLS

AFM	Atomic Force Microscope
Ag	Sliver
Al	Aluminum
ALD	Atomic Layer Deposition
Al_2O_3	Aluminum Oxide
Au	Gold
BAI	Butyl Ammonium Iodide

BCP	Bathocuproine
Br-	Bromide Ion
$CaTiO_3$	Calcium Titanium Oxide
CB	Conduction Band
Cd^{2+}	Cadmium Cation
CO^{2+}	Carbon Dioxide Cation
CTM	Charge Transport Material
Cu^{2+}	Copper Cation
DMF	Dimethylformamide
DMSO	Dimethyl Sulfoxide
DSSC	Dye Sensitized Solar Cells
EL	Electroluminescence
EQE	External Quantum Efficiency
ETL	Electron Transport Layer
ETM	Electron Transport Material
eV	Electron Volt
FAI	Formamidinium Iodide
Fe^{2+}	Iron Cation
FF	Fill Factor
FTO	Fluorine doped Tin Oxide
HTL	Hole Transport Layer
HTM	Hole Transport Material
I^-	Iodine Ion
ITO	Indium doped Tin Oxide
J_{SC}	Short Circuit Current Density
J-V	Current – Voltage
MAI	Methylammonium Iodide
MgF_2	Magnesium Fluoride
MPP	Maximum Power Point
NBG	Narrow Band Gap
NiO	Nickle Oxide
NREL	National Renewable Energy Lab
OPV	Organic Photovoltaic
Pb^{2+}	Lead Cation
PbI_2	Lead Iodide
$Pb(SCN)_2$	Lead (II) Thiocyanate
PCE	Power Conversion Efficiency
PEAI	Phenethyl Ammonium Iodide
PL	Photoluminescence
PLQY	Photoluminescence Quantum Yield
PMMA	Poly (methyl methacrylate)

Poly- TPD	Poly[N,N'-bis(4-butylphenyl)-N,N'-bisphenylbenzidine]
PSC	Perovskite Solar Cells
PTAA	Poly[bis(4-phenyl) (2,4,6-trimethylphenyl) amine]
PV	Photovoltaic
RMS	Root Mean Square
SAMs	Self-Assemble Monolayers
SC	Solar Cells
SCLC	Space Charge Limited Current
SEM	Scanning Electron Microscope
Sn^{2+}	Tin Cation
SnF_2	Tin Fluoride
SnI_2	Tin Iodide
SnO_2	Tin Oxide
Sn-Pb	Tin Lead
TCO	Transparent Conducting Oxide
TiO_2	Titanium Dioxide
TRPL	Time Resolved Photoluminescence
TSC	Tandem Solar Cell
UVO	Ultra-Violet Ozone
UV-Vis	Ultraviolet-visible
VB	Valence Band
V_{OC}	Open Circuit Voltage
WBG	Wide Bandgap
WF	Work Function

1 INTRODUCTION

1.1 Motivation of the Study

Globally, energy demand increases over time due to economic development, technological advancements, population growth, climate and seasonal changes, and shifts in infrastructure and lifestyle.[1,2] To meet this need, a diverse range of energy sources is utilized, categorized into fossil fuels (such as oil, coal, and natural gas), renewable energies (such as solar, wind, hydro, biomass, geothermal, and hydrogen), and fissile materials (notably uranium and thorium).[3,4] Man-made climate change, closely linked to energy demand and consumption, is one of the most pressing global challenges of our time. Nonrenewable energy sources, particularly fossil fuels, are the primary contributors to global climate change due to their high greenhouse gas emissions. Consequently, the use of renewable energy sources is considered as a vital option to mitigate this problem while meeting our energy demand. In relation to this, renewable energy sector is experiencing rapid growth amid rising global energy demand. It represents a superior alternative to conventional non-renewable sources, offering substantial economic and strategic benefits while remaining environmentally sustainable.[5] These sources are abundant, sustainable, enhance energy security, and have minimal environmental impact.[6,7]

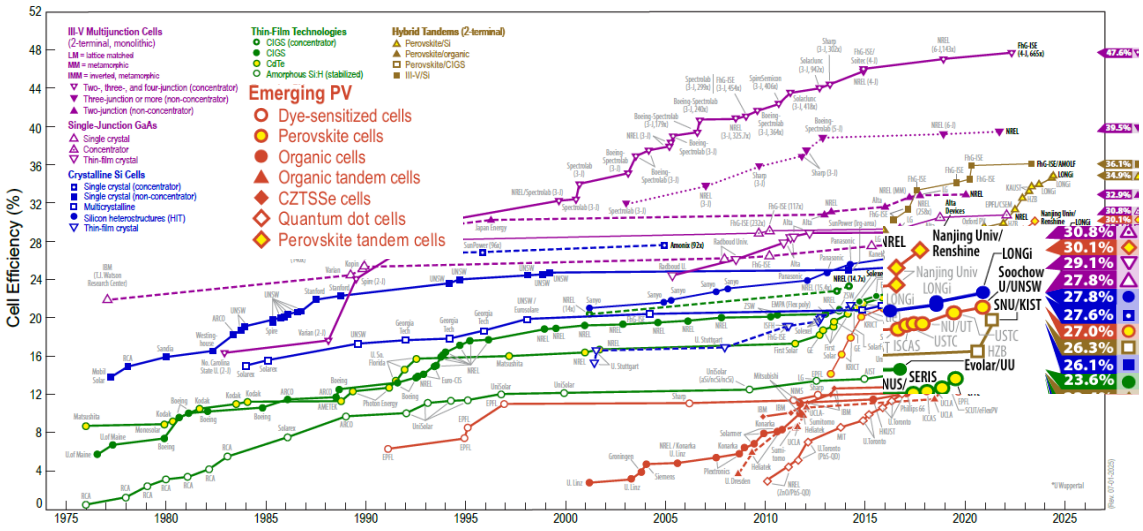

Figure 1.1*: The National Renewable Energy Laboratory (NREL) solar cell efficiency chart, taken from the 2025 report.*[8]

Among the various renewable and clean energy sources, solar energy stands out as an ideal candidate due to its abundance, free availability, and carbon emission-free nature.[9] On a clear day, the Earth receives about 173,000 terawatt-hours of energy from the sun—almost the same as the total amount of energy the world used each year before the COVID-19 pandemic.[10] This enormous supply of sunlight shows how much potential solar panels have as a clean and dependable source of electricity. Important advances in solar technology began in the early 1900s with the development of quantum theory and the discovery of the photovoltaic effect.[11] A photovoltaic (PV) device, or a solar cell, which converts solar energy into electrical energy, is fundamental to solar energy utilization. While research in this field began in the mid-20th century—most notably with the development of silicon-based devices in 1954—it has since expanded to include a wide variety of new materials. Most commercially available solar cells today are based on silicon, which is well known for its high efficiency in converting sunlight into electricity. However, challenges such as silicon's low light absorption coefficient and rigidity have driven the need to develop alternative PV technologies.[12,13] In response to these limitations, recent advancements have led to the development of next-generation solar cells, including organic solar cells,

dye-sensitized solar cells, and perovskite solar cells. Each of these technologies offers unique advantages and promising pathways toward high-efficiency, low-cost photovoltaics.[14,15]

Of these next-generation approaches, perovskite solar cells rapidly emerged as a leading technology. Their rise is driven by exceptional optoelectronic properties—such as long carrier diffusion lengths[16], high absorption coefficients,[17] lower manufacturing costs, low-temperature processing, lightweight nature, and simpler production methods, compared to traditional silicon-based cells.[18,19] The rapid evolution of perovskite solar cells is the result of transformative contributions from several key figures in the scientific community. The field was inaugurated in 2009 by Tsutomu Miyasaka, who demonstrated the first perovskite-based photovoltaic device.[20] This foundation was significantly expanded by Michael Grätzel, whose pioneering work on dye-sensitized solar cells provided the conceptual framework for early perovskite research, and Nam-Gyu Park, who was instrumental in developing high-efficiency solution-processed PSCs.[21,22] However, the rapid rise of the perovskite was catalyzed in 2012 by Henry Snaith and colleagues at Oxford University, who developed solid-state perovskite solar cells and significantly improved device architectures,[23] while Alex Jen advanced the field through interface engineering and the development of flexible devices.[24] Furthermore, the collective efforts of scholars such as Yang Yang, Edward H. Sargent, and C. Adachi have been instrumental in optimizing stability, thereby positioning PSCs as a leading next-generation technology.[25,26,27]

As shown in Figure 1.1, the power conversion efficiencies of perovskite solar cells have increased from 3.8% in 2009 to an anticipated 27.0% in 2025, approaching the record efficiency of silicon solar cells, which currently stands at 27.81%, according to a recent press release.[8] However, these high-performing perovskite devices are primarily lead-based, raising concerns about environmental toxicity and limiting their suitability for sustainable large-scale deployment. To address these challenges, partial substitution of lead with tin has

emerged as a viable strategy. Lead–tin mixed perovskites reduce the toxic lead content and enable bandgap tuning toward the infrared region. Pure lead-based perovskites, while efficient, pose toxicity concerns and have limited spectral coverage. Tin-based perovskites, on the other hand, offer lower bandgaps but face challenges in stability and reproducibility. By alloying lead and tin, researchers can engineer perovskites with tunable bandgaps in the ideal range of 1.2–1.4 eV.[28] This compositional tuning enables the integration of Pb-Sn mixed perovskites as bottom cells in all-perovskite tandem architectures, pushing the boundaries of solar cell efficiency.[29,30]

Despite their promising potential, Pb-Sn mixed perovskite solar cells continue to face several critical challenges. A primary concern is the consistently low open-circuit voltage (V_{OC}), which results from enhanced non-radiative recombination, oxidation of Sn^{2+} to the more stable Sn^{4+}, defect formation, and suboptimal energy band alignment—factors that collectively limit device performance. Furthermore, the next target highlights limitations of the conventional antisolvent method used in perovskite film formation. Specifically, Sn crystallizes much faster than Pb, leading to inhomogeneous Pb-Sn crystallization throughout the film, uneven film morphology, and poor batch-to-batch repeatability, all of which further degrade device efficiency.

To address V_{OC} losses, the first project, titled “Mechanisms and Mitigation of V_{OC} Losses in Pb–Sn Perovskite Solar Cells,” demonstrated the effectiveness of interface engineering in suppressing non-radiative recombination. A key strategy involved introducing a thin poly(triarylamine) (PTAA) interlayer between the poly(3,4-ethylenedioxythiophene): poly(styrenesulfonate) (PEDOT:PSS) and the narrow-bandgap (NBG) Pb–Sn mixed perovskite. This interfacial modification, combined with careful optimization of film morphology and device architecture, significantly improved V_{OC} and enhanced overall photovoltaic performance. The second project, titled “Impact of Improved NBG Cells in All-Perovskite Tandem Architectures,” demonstrated that integrating the improved narrow-bandgap

(NBG) perovskite with a wide-bandgap (WBG) perovskite, specifically $Cs_{0.3}FA_{0.6}MA_{0.1}Pb(I_{0.7}Br_{0.3})_3$, which has a bandgap of approximately 1.70 eV, led to significant improvements in open-circuit voltage and overall power conversion efficiency.

The third project addressed limitations associated with film formation by replacing the traditional antisolvent technique with gas quenching, which has shown considerable promise. This approach enables better control over crystallization kinetics, eliminates the need for toxic solvents, improves film uniformity, enhances reproducibility, and yields larger grain sizes, ultimately contributing to superior device performance.

1.2 Research Objectives

1.2.1 General Objective

This research aims to enhance the performance of Pb-Sn perovskite solar cells by addressing two critical challenges. First, it targets open-circuit voltage losses in narrow-bandgap absorbers used in both single-junction perovskite solar cells and all-perovskite tandem architectures. Second, it seeks to overcome the film-forming challenges of Pb-Sn mixed perovskites encountered in conventional antisolvent-quenching-based processing. The study proposes strategies to mitigate V_{OC} losses in narrow bandgap perovskite sub-cells for all-perovskite tandem solar cells and to employ a gas-quenching-based processing technique to fabricate high-quality Pb-Sn mixed perovskite films, thereby improving the efficiency of single-junction perovskite solar cells.

1.2.2 Specific Objectives

The primary objectives of this research are to:

i. Optimize the concentration of the interlayer (PTAA) between PEDOT: PSS and Pb-Sn perovskite.
ii. Fabricate narrow bandgap sub-cells using various hole transport materials,

such as PEDOT: PSS-based PSCs, PTAA-based PSCs, and PTAA/PEDOT: PSS-based PSCs to enhance V_{OC} and incorporate them into tandem architectures.

iii. Investigate the crystallization kinetics of Pb-Sn mixed perovskite films under gas-quenching conditions compared to conventional antisolvent methods.

iv. Assess the film morphology, grain size, and repeatability of perovskite films fabricated via gas quenching.

1.3 Dissertation Outline

This dissertation comprises seven chapters and discusses concerns about PSCs, including both single-junction and tandem configurations. The first chapter outlines the motivation, objectives, and structure of the dissertation.

The second chapter provides the theoretical background of solar cells, an overview of PSCs, and their working principles. Section 2.3 focuses explicitly on Pb-Sn mixed perovskites, highlighting their advantages, such as bandgap tuning, reduced toxicity, and compatibility with tandem applications, compared to pure lead- and pure tin-based perovskites. It also addresses the challenges associated with Pb–Sn mixed perovskites, including instability, energy band misalignment, tin oxidation, defects, V_{OC} losses, and uncontrolled crystallization. To overcome these challenges, researchers have employed a combination of quenching techniques, additive engineering, passivation strategies, and interface modifications. The final section of this chapter further explores two distinct all-perovskite tandem configurations, four-terminal (4T) and two-terminal (2T), by reviewing their device architectures and providing a brief comparison of their structural and operational characteristics.

Chapter 3 describes the research methods and experimental steps needed to make perovskite thin films and both single-junction and all-perovskite tandem

solar cells. Furthermore, this chapter describes the procedures for thin-film and device performance characterization applied to both configurations

Chapter 4 explores the mechanisms behind V_{OC} losses and their mitigation in Pb–Sn perovskite solar cells through interface engineering between the HTL and the perovskite. The study focuses on a Pb–Sn perovskite absorber with a narrow bandgap of 1.25 eV. Instead of using a conventional single-layer HTL, a bilayer configuration is introduced, resulting in a significant enhancement of V_{OC} and enabling the device to achieve a power conversion efficiency of 20.3%. Furthermore, this chapter provides a comprehensive characterization of the synthesized perovskite films, employing microscopic and spectroscopic techniques to assess surface morphology and topography, as well as interfacial properties, including defect states and energy-level alignment.

In tandem solar cells, the V_{OC} of the bottom cell directly contributes to the total device voltage. Therefore, enhancing the V_{OC} in Pb–Sn mixed perovskites is crucial for improving overall tandem performance, as described in Chapter 5. This chapter builds on the findings presented in Chapter 4, beginning with the optimized design of single-junction Pb–Sn mixed perovskite solar cells and progressing toward the development of all-perovskite tandem architectures. The tandem cell employs a 1.25 eV bandgap Pb–Sn mixed perovskite, combined with a conventional Pb-based perovskite with a 1.7 eV bandgap. A charge-carrier-selective bilayer strategy enables effective charge-carrier extraction, enabling the tandem structure to achieve an open-circuit voltage of 2.00 V and a power conversion efficiency of 25%.

The various challenges associated with Pb-Sn mixed perovskite solar cells, discussed in Chapter 2, directly affect their efficiency. Chapter 6 explores gas quenching as an alternative to the traditional antisolvent method for fabricating Pb-Sn mixed perovskite solar cells. This technique eliminates the need for hazardous antisolvents and enhances performance consistency. The gas-

quenching-based selective crystallization technique also helps produce high-quality films by allowing grains to grow at a controlled rate and slowing the crystallization process. These advancements ultimately enabled a power conversion efficiency of 19.1% to be achieved.

The final chapter presents the conclusions and outlooks derived from the research conducted throughout this thesis, summarizing key findings and their scientific implications. It also offers a forward-looking perspective on potential future directions for perovskite solar cell development, including opportunities for further material optimization and device engineering.

2 STUDY BACKGROUND AND STATE OF THE ART

This chapter offers a foundational overview of solar cells and metal-halide perovskites, with a particular focus on the Pb–Sn mixed compositions employed in this thesis. It begins by outlining the fundamentals of solar cells and the evolution of solar cell technologies across successive generations, highlighting their respective potentials, inherent challenges, and the rationale for selecting perovskites as promising candidates for future-generation device physics. The chapter concludes by synthesizing key theoretical frameworks and experimental findings from the literature, encompassing both single-junction Pb–Sn perovskite solar cells and all-perovskite tandem architectures.

2.1 Solar Cells

Solar cells are semiconductor devices that convert sunlight directly into electricity using the photovoltaic effect. When the solar cell absorbs photons, their energy excites electrons from the valence band to the conduction band, leaving behind holes. This procedure generates electron-hole pairs within the absorber material, typically a p-n junction. An internal electric field separates these charge carriers and drives them toward the electrodes, resulting in an electric current that can power external loads.[31] The theoretical foundation of solar cells lies in the photoelectric effect, first observed by Alexandre Edmond Becquerel in 1839 and later explained by Albert Einstein in 1905.[32,33] The first actual solar cell was developed in 1883 by *C. Fritts*, using selenium coated with a thin layer of gold, though its efficiency was less than 1%.[34] Building on these early experiments, a breakthrough came in 1954 at Bell Labs, where *D. Chapin, C. Fuller,* and *G. Pearson* created the first silicon-based photovoltaic cell**,** achieving around 6% efficiency. This year marked the beginning of practical solar technology, initially used to power satellites during the 1960s space race, where reliability and independence from Earth-based power sources were critical.[35] Following this milestone, the subsequent decades witnessed significant improvements as solar cells became more efficient and affordable, as illustrated in Figure 2.1.

2.1.1 Generation of Solar Cells

Classifying solar cells into three generations offers a distinct framework for understanding their technological development, material advancements, and performance achievements.

First-generation solar cells are silicon-based technologies, including monocrystalline and polycrystalline silicon cells. These cells rely on well-established semiconductor physics and have been the backbone of commercial photovoltaics for decades.[36] These devices are known for their superior efficiency and stability. Despite their stability and reliability, first-generation cells face limitations in material costs, energy-intensive production, and performance degradation at high temperatures.[37,38]

Second-generation solar cells, often called thin-film cells, employ semiconductor layers only a few micrometers thick, significantly thinner than those in crystalline silicon-based cells. The combination of using less material and lower-cost manufacturing processes enables manufacturers of solar panels based on this technology to produce PV panels at much lower cost. There are three types of solar cells considered in this category: amorphous silicon (a-Si), cadmium telluride (CdTe), and copper indium gallium selenide (CIGS). However, concerns over toxic elements (e.g., cadmium in CdTe) and the devices' lower efficiency and long-term stability have limited their widespread adoption.[39,40]

The third-generation solar cells represent the frontier of photovoltaic innovation, aiming to surpass the Shockley–Queisser efficiency limit through novel mechanisms and materials. This category includes perovskite solar cells, organic photovoltaics, quantum dot cells, and multi-junction tandem architectures.[41,42] These emerging technologies explore advanced concepts like hot-carrier extraction, upconversion, and intermediate band absorption to harness a broader spectrum of sunlight.[43,44]

While still facing challenges in stability, scalability, and commercialization, third-generation cells embody the future of high-performance, sustainable solar energy. Therefore, the third generation of PV technology, particularly perovskite solar cells, is regarded as the most promising, lightweight, and versatile option for photovoltaic power generation. Indeed, the most compelling features of these devices include tunability of their optoelectronic and electronic properties, solution-processability, and the low cost of their precursor materials.[45]

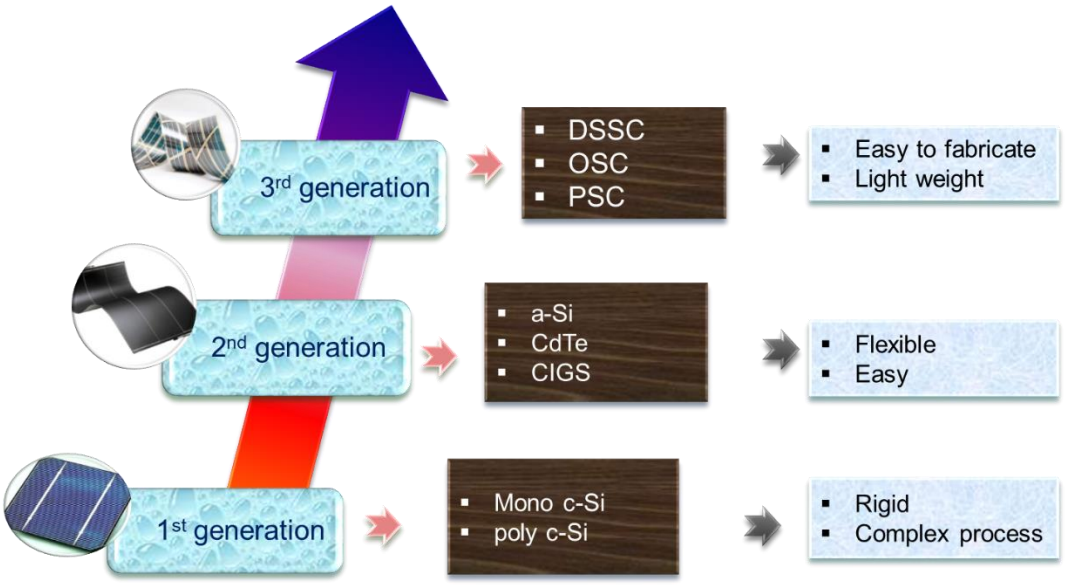

***Figure 2.1**: Three generations of solar cells illustrating the transition from conventional silicon to advanced thin-film and next-generation materials, driving the global shift toward sustainable energy solutions.*

Understanding the limits of solar cell performance requires a thorough examination of the fundamental physical principles governing their operation. These limiting factors encompass the electronic band structure of semiconductors, the position of the Fermi level, theoretical efficiency bounds such as the Shockley–Queisser limit, and loss mechanisms such as thermalization and non-radiative recombination. Each of these plays a critical role in determining a solar cell's effectiveness in converting sunlight into electrical energy.

A semiconductor's bandgap E_g is the energy difference between its valence band (maximum energy of occupied states) and conduction band (minimum energy of unoccupied states). Only photons with energies $E \geq E_g$ can excite an electron across the bandgap, initiating electrical conduction. The bandgap, therefore, determines the spectral region over which a solar cell can harvest photons for energy conversion:

$$E_g = E_C - E_V, \tag{2.1}$$

where E_C and E_V are the energies of the conduction and valence band edges, in a solar cell, the process begins with photon absorption, since only photons with energy greater than or equal to the semiconductor bandgap can excite electrons from the valence band into the conduction band. The probability of absorption determines the material's absorptivity, which depends on the absorption coefficient α(E), the thickness (d) of the absorber layer governed by the Beer–Lambert law:

$$A(E) = 1 - e^{-\alpha(E)d} \tag{2.2}$$

The interaction between the semiconductor materials in the device and incident light primarily determines current generation in a solar cell. Each material has a unique energy-dependent absorptivity α(E), which indicates how strongly it absorbs a range of photon energies. When photons are absorbed, they generate electron-hole pairs; if these charge carriers are effectively separated and guided to the electrodes, they can collect an electrical current. The resulting photogenerated current density J_{ph} depends on two main factors: the material's ability to absorb light and the spectral distribution ϕ(E) of the light source, which describes the range of photon energies and their intensities, as shown in equation 2.3.

$$J_{ph} = q \int_0^{\infty} \phi(E)\,(1 - e^{-\alpha(E)d}) dE \tag{2.3}$$

However, if the photon energy is much larger than the bandgap, the excited carriers quickly lose excess energy through phonon scattering, a process known as thermalization, and the energy lost per photon is $E_{loss} = (E_{photon} - E_g)$, which fundamentally limits the efficiency of single-junction devices. Moreover, after relaxation, carriers must be transported to the electrodes, which occurs via drift in the built-in electric field of the p–n junction.

Additionally, during carrier transport, recombination processes inevitably occur, either radiatively or non-radiatively via defect states through Auger interactions, or Shockley–Read–Hall mechanisms, as depicted in Figure 2.2. Such recombination pathways impose fundamental losses, thereby reducing both current and voltage.

Radiative recombination, which is also called band-to-band recombination, occurs when an electron in the conduction band recombines with a hole in the valence band, releasing energy in the form of a photon. This emitted photon has energy approximately equal to the semiconductor's bandgap. It is relatively unimportant in silicon because its radiative lifetime is extremely high.[46] Yet, on the other hand, there are also non-radiative recombination processes, and it can be auger or trap-assisted recombination.

Auger recombination involves three particles: an electron and a hole, which recombine via a band-to-band transition and release the energy to another electron or hole.[47] The expression for the net recombination rate is similar to that of simple band-to-band recombination, but the involvement of a third particle affects the recombination rate.[48] Shockley-Read-Hall (SRT) recombination, also named trap-assisted recombination. SRT is a two-step process that occurs when an electron falls into a trap, an energy level within the bandgap caused by a foreign atom or a structural defect. Once the trap fill, it cannot accept another

electron. In a second step, the electron occupying the trap falls into an empty valence-band state. The number of impurities and defects in the silicon determines SRH recombination.[49]

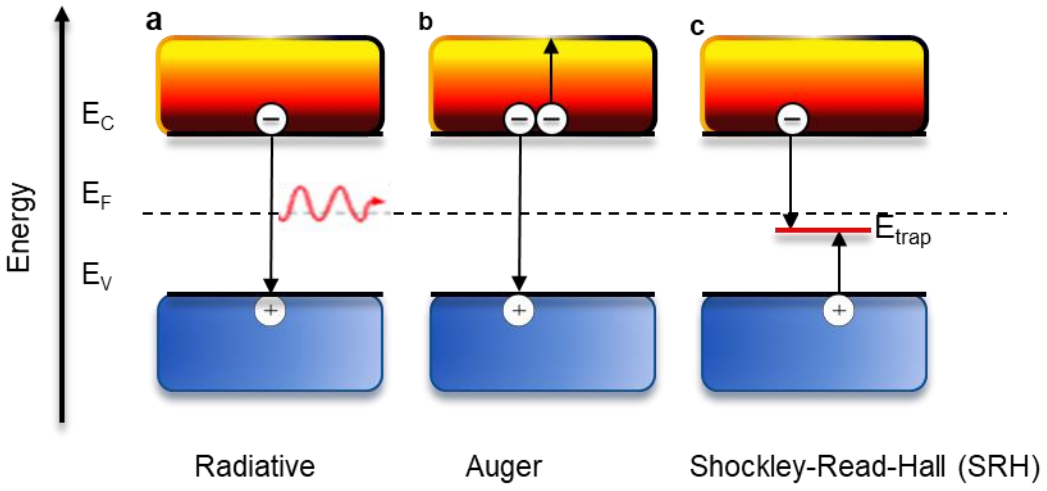

***Figure 2.2**. Schematic recombination mechanisms in a band diagram, (a) Radiative recombination and (b) Auger band-to-band decay represent intrinsic processes, (c) Shockley–Read–Hall (SRH) recombination.*

Furthermore, under illumination, the system departs from equilibrium, and separate quasi-Fermi levels for electrons and holes emerge; the splitting between them determines the maximum open-circuit voltage. The combined effects of absorption, generation, relaxation, transport, recombination, and quasi-Fermi level splitting captured in the Shockley–Queisser detailed balance limit, which predicts the maximum efficiency of a single-junction solar cell to be about 33.7% near E_g approximately 1.34 eV under AM1.5G illumination, and the current–voltage relation for a single junction cell is expressed as in question 2.4.[50]

$$J(V) = J_{ph} - J_0\left(e^{qV/kT} - 1\right), \tag{2.4}$$

where J_0 is the dark saturation current linked to recombination.

2.2 Perovskite Solar Cells

Perovskite solar cells are named after the mineral perovskite, as they share its distinct crystal structure. The original compound identified as perovskite was calcium titanate ($CaTiO_3$), discovered in 1839 by German mineralogist Gustav Rose. He named it in honor of Lev Perovski, which led to the broader family of materials sharing the same distinctive crystal structure being called 'perovskites'.[51] These compounds share a common crystal framework described by the general formula ABX_3**,** where A is typically a monovalent cation (such as methylammonium, formamidinium, or cesium), B is a divalent metal cation (commonly lead, or tin), and X is a halide anion (such as iodide, bromide, chloride or oxygen). Together, they form the characteristic perovskite lattice structure, as illustrated in Figure 2.3a and b**.** Hybrid perovskites, comprising both inorganic and organic components, were first synthesized and reported in 1978.[52] Yet, their potential as light-harvesting materials was not reported until 2009, when Kojima and co-workers demonstrated the first solar cell employing methylammonium lead iodide (MAPI) and methylammonium lead bromide (MAPBr). In this pioneering work, perovskite nanocrystals were introduced as absorbers within a dye-sensitised solar cell (DSSC) configuration, effectively replacing conventional organic dyes and achieving a power conversion efficiency (PCE) of 3.8%.[20]

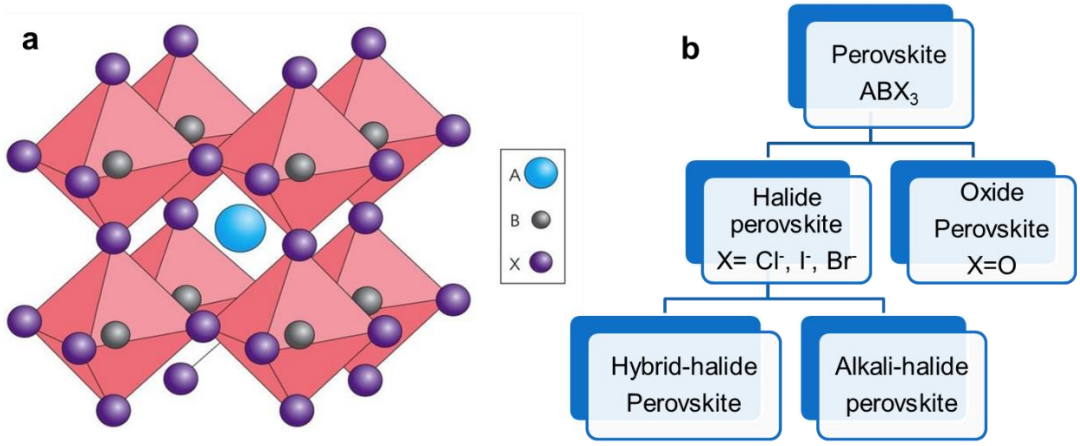

Figure 2.3: *Basic structure of ABX_3 perovskite (a) reproduced with permission from Springer Nature[53] and Schematic representation of the compositional diversity of perovskite materials, highlighting key categories such as halide-based perovskites and oxide-based perovskites (b).*

The perovskite materials structure features a body-centered lattice that may adopt hexagonal, cubic, or orthorhombic symmetry, with the positively charged A-site cation occupying the central position. As shown in Figure 2.4, for a perovskite to adopt a stable, symmetric cubic structure, the tolerance factor typically falls within 0.8-1.0. Values close to 1.0 indicate a near-perfect fit, resulting in a highly symmetric and efficient crystal lattice ideal for charge transport. Deviations below 0.8 often lead to structural distortions, such as orthorhombic or tetragonal phases, while values above 1.0 may result in hexagonal or other non-perovskite structures.[54]

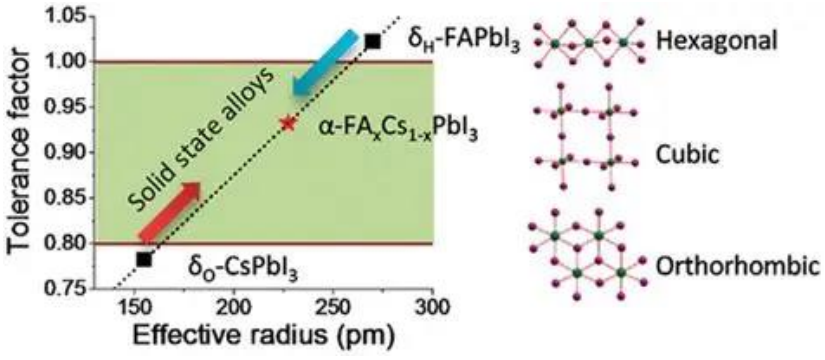

Figure 2.4*: Structural variations in perovskite materials as a function of tolerance factor reproduced with permission from reference[55], Copyright © 2015 ACS*

Specifically, a Goldschmidt tolerance factor within the appropriate range indicates that the body-centered structure is perovskite.

The Goldschmidt tolerance factor (t) is defined as follow:

$$t = \frac{r_A + r_x}{\sqrt{2}(r_B + r_X)}, \quad (2.5)$$

where r_A, $r_{B,}$ and r_X are the effective ionic radii for A, B, and X atoms, respectively. It should be within the range of $0.8 < t < 1.0$ to sustain the 3D structure.[56] The A-site cation in perovskite materials can be either inorganic, such as rubidium (Rb^+) or cesium (Cs^+), or organic, including methylammonium (MA^+, $CH_3NH_3^+$) and formamidinium (FA^+, $HC(NH_2)_2^+$). Importantly, compositional mixing of these cations is not only feasible but also beneficial, as it can substantially enhance the structural and environmental stability of the perovskite.[57]

Perovskite solar cells have emerged as one of the most promising innovations in photovoltaic technology due to their exceptional photoelectric properties, including high absorption coefficients, long carrier diffusion lengths, and tunable bandgaps.[58,59] Their low-temperature solution-based fabrication methods also enable cost-effective and flexible manufacturing.

2.2.1 Structural Configurations of Perovskite Solar Cells

This section presents the core design principles of perovskite solar cells, focusing on two primary device architectures: the planar n–i–p and the inverted p–i–n configurations, as shown in Figure 2.5. It also highlights the key functional layers essential for efficient photovoltaic operation.

In the regular (n-i-p) architecture, Figure 2.5a, the perovskite layer is deposited on electron transport layer (ETL) such as TiO_2, SnO_2, ZnO, PCBM (([6,6]-phenyl-C_{61}-butyric acid methyl ester) and a hole transport layer (HTL), Spiro-MeOTAD (2,2′,7,7′2,2′,7,7′-Tetrakis[N,N-di(4-methoxyphenyl)amino]9,9′9,9′spirobifluorene),

PTAA (poly(triarylamine)), P3HT (poly(3-hexylthiophene)) and NiO_x (inorganic alternative).[60] This design enables simpler fabrication and is well-suited for scalable techniques like blade coating and inkjet printing. However, it demands high-quality perovskite films with minimal defects to ensure efficient charge extraction and reduced recombination.

On the other hand, the inverted (p–i–n) architecture, as seen on Figure 2.5b, reverses the layer sequence, placing the HTL such as, poly(3,4-ethylenedioxythiophene) poly(styrene sulfonate) (PEDOT: PSS), PTAA, P_3CT_{-X} (X = Na, K, Rb, Cs), NiO_x, CuSCN, CuI, and CuO beneath the perovskite and the ETL with PCBM, C_{60}, ZnO, TiO_2, MoO_3, SnO_2 on top.[61] This configuration is compatible with low-temperature processing and flexible substrates, making it attractive for tandem integration. Inverted architecture exhibits reduced hysteresis and demonstrates superior interface stability, especially when utilizing organic transport layers.

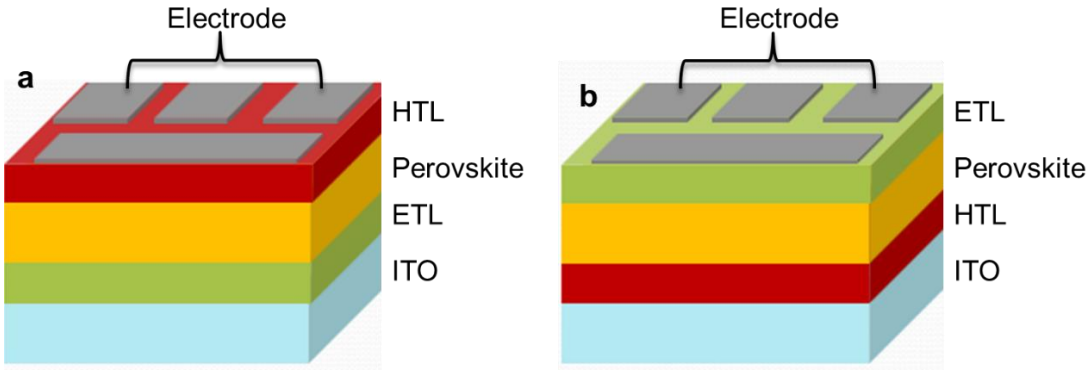

***Figure 2.5**: Typical device structure of perovskite solar cells: (a) regular (n–i–p) architecture, where the electron transport layer (ETL) is deposited beneath the perovskite absorber, followed by the hole transport layer (HTL) on top, and (b) inverted (p–i–n) architecture, where the HTL is at the bottom, followed by the perovskite layer and then the ETL.*

2.2.2 Working Mechanism of Perovskite Solar Cells

Perovskite solar cells operate by converting sunlight into electricity through a sequence of photophysical processes within a layered device structure, as discussed in the previous section. Figure 2.6 shows the general working mechanism of perovskite solar cells. In a typical perovskite solar cell, the working mechanism begins with photon absorption by the perovskite active layer, which initiates the generation of charge carriers. These carriers then undergo separation, are transported through the respective charge-transport layers, and are ultimately collected at the electrodes, representing the key sequential steps that define the device's operational process.[62] The electron transport layer, composed of n-type material, facilitates the migration of electrons from the absorber layer to the cathode. The hole-transport layer, made of p-type material, carries holes from the absorber layer to the anode. Finally, the electrodes included an anode and a cathode, including FTO, ITO, Ag, Al, Au, etc.[63]

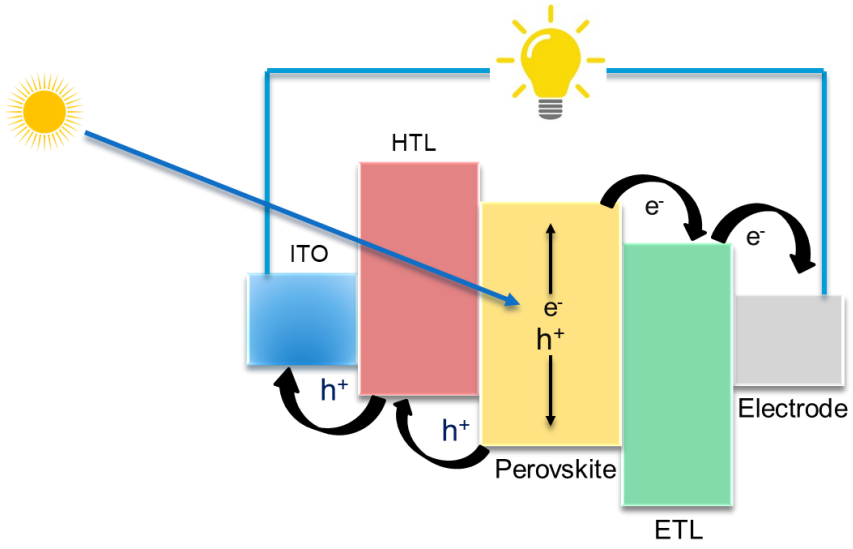

Figure 2.6: *Schematic illustration of working principle of typical p-i-n structure perovskite solar cells, with the key processes involved in light absorption, exciton generation, charge separation, and carrier transport across the full stack perovskite device layers.*

Light absorption & Exciton generation: In a first step, Perovskite materials exhibit strong absorption across the visible spectrum due to their direct bandgap and high absorption coefficients. Upon illumination, photons are absorbed in the

perovskite layer, generating electron–hole pairs (excitons).[64] These steps are governed by the material's band structure, exciton binding energy, film morphology, and optical design, all of which determine how efficiently photons are absorbed and converted into bound or free electron–hole pairs.

Exciton diffusion to the interface & dissociation: Once generated, excitons or free carriers must reach the interfaces with transport layers due to the low exciton binding energy in perovskites, these pairs readily dissociate into free charge carriers. Electrons are transported to the ETL, while holes migrate to the hole HTL. Dissociation occurs at interfaces with ETL or HTL layers, where energy-level offsets facilitate charge separation.[65,66]

Charge Transport and Collection Mechanisms

Following dissociation, electrons and holes migrate through their respective transport layers. Efficient charge transport depends on the mobility and conductivity of ETL and HTL materials.[67] These properties, combined with minimal interfacial defects and low extraction barriers, dictate the efficiency of carrier transfer across the interface. Finally, the electrodes collect the charges; these typically comprise a transparent front contact, such as ITO or FTO, and a metal or carbon-based rear contact. Early research established the use of gold and silver rear contacts to ensure high conductivity.[68] More recently, pioneers such as Henry Snaith have championed the integration of carbon electrodes as a cost-effective and stable alternative to traditional metal evaporation.[69]

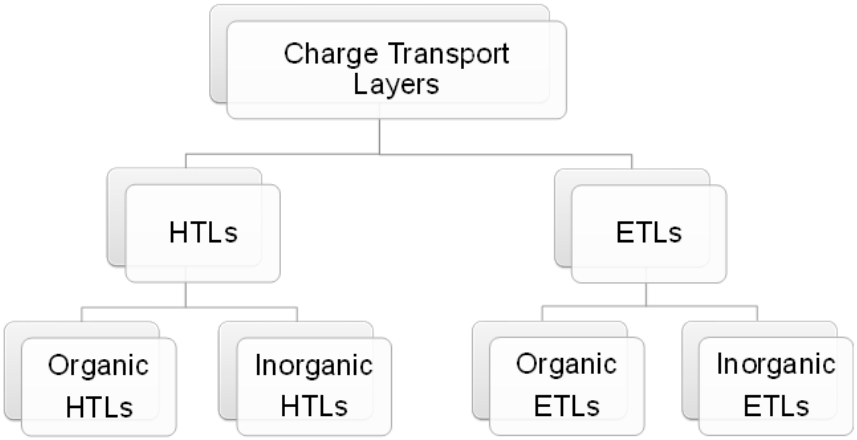

***Figure 2.7**: Overview of commonly used charge transport layers in perovskite solar cells, including hole transport layers (HTLs) and electron transport layers based on their function and compatibility with different device architectures.*

Figure 2.5 depicts the typical architecture of perovskite solar cells, which play a pivotal role in regulating carrier flow and minimizing recombination in photovoltaic and optoelectronic devices.[70] The active layer, perovskite, is sandwiched between these transport layers, HTLs and ETLs, each further subdivided into organic and inorganic categories as shown in Figure 2.7. On the HTL side, organic materials such as Spiro-OMeTAD and PEDOT: PSS are widely used for their tunable energy levels and solution-processability, while inorganic HTLs like NiO_x and CuSCN offer superior thermal stability, High mobility, excellent transparency, good chemical stability, high conductivity, perfect band alignment, and long-term durability.[71,72] Similarly, the ETL branch includes organic options like PCBM and C_{60}, known for their compatibility with low-temperature processing,[73,74] alongside inorganic ETLs such as TiO_2, SnO_2, and ZnO, which provide excellent electron mobility and band alignment.[75,76] ETLs such as TiO_2, SnO_2, or ZnO selectively extract and transport electrons toward the cathode, while HTLs like Spiro-OMeTAD, PTAA, or NiO_x enable efficient hole collection at the anode. The energy-level alignment between layers is optimized to minimize recombination and maximize charge separation, thereby enhancing device

performance. Arrows indicate the flow of photogenerated electrons and holes under illumination, emphasizing the importance of interfacial engineering and material selection in achieving high power conversion efficiency.

Key performance metrics of perovskite solar cells

This thesis evaluates the perovskite solar cell performance evaluated through current–voltage (I–V) measurements, which yield key parameters such as power conversion efficiency (PCE), open-circuit voltage (V_{OC}), fill factor (FF), and short-circuit current (J_{SC}) under a measurement of 1 sun illumination (100 mW/cm^2) as shown in Figure 2.8. During the measurement process, a bias voltage is applied to the illuminated solar cell, and the corresponding current is recorded across a range of applied voltages.

a) Short-circuit current density (J_{SC}): The amount of current generated per unit area when the perovskite solar cell is short-circuited (i.e., when the voltage across the cell is zero, V = 0 V). It represents how effectively the cell converts light into electrical current and is typically expressed in mA/cm². In practical applications, the short-circuit current (I_{SC}) is generally reported as current density, defined as the electric current per unit area:

$$J_{SC} = I_{SC} \times Active\ area\ of\ the\ solar\ cells \tag{2.6}$$

b) Open circuit voltage (V_{OC}): V_{OC} is the maximum voltage with no current flowing (i.e., the circuit is open) or no current is flowing (J_{SC} = 0 mA/cm^2), the voltage of the electrodes under illumination is neutralized due to the bias voltage. The expression for open-circuit voltage is derived by setting the net current in the solar cell equation to zero.

$$V_{OC} = \frac{nKT}{q} \ln\left(\frac{I_L}{I_o} + 1\right), \tag{2.7}$$

where n is the ideality factor of the diode, K is Boltzmann constant (1.38 x 10^{-23}J/ºK), T is the temperature, q is electron charge (1.602 × 10^{-19} coulombs), I_L is the current generated through light illumination, and I_o is reverse saturation current at which the solar cell is operating.

c) Fill factor (FF): FF quantifies how "square" the J–V curve is, indicating how efficiently the solar cell converts the available voltage and current into usable power. This parameter can be calculated via *equation 2.8.*

$$\mathrm{FF} = \frac{\mathrm{P_{max}}}{\mathrm{V_{ov}} \times \mathrm{J_{sc}}} = \frac{\mathrm{J_{max}} \times \mathrm{V_{max}}}{\mathrm{V_{oc}} \times \mathrm{J_{sc}}}, \tag{2.8}$$

where P_{max} is the maximum output power, V_{OC} is the open-circuit voltage, J_{SC} is the short circuit current, and J and V_{max} are the current and voltage at the maximum power point.

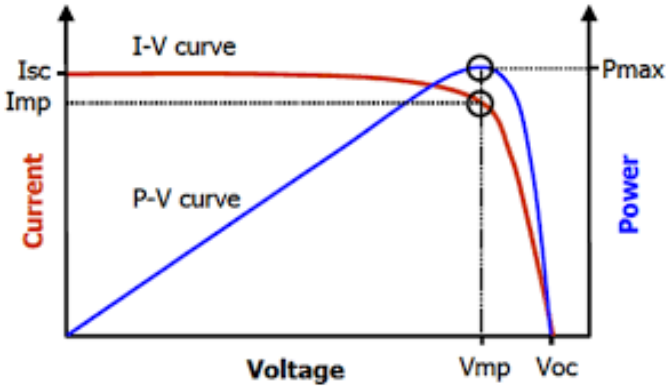

Figure 2.8*: Typical current density-voltage (I-V) and power–voltage (P-V) curve for a perovskite solar cell (red curve) under illumination and Efficiency of the perovskite solar cell for different applied voltages (blue curve). The circles mark the maximum power point. The black rectangle represents the maximum power density achieved.* Reproduced with permission from reference[77] *under license CC BY 3.0.*

d) Power conversion efficiency (PCE): PCE is the percentage of incident solar energy that is converted into electrical power. It's the most crucial figure of merit for comparing solar cell technologies. Calculated by equation 2.9.

$$PCE\ (\eta) = \frac{P_{electrical}}{P_{light}} = \frac{P_{max}}{P_{in}} = \frac{FF \cdot V_{oc} \times J_{sc}}{P_{in}}, \quad (2.9)$$

where P_{max} is the maximum electrical power output, P_{in} is the incident light power density (under 100 mW/cm² under AM 1.5G conditions), FF is the fill factor, V_{OC} is the open-circuit voltage, and J_{SC} is the short-circuit current density.
In this thesis, J–V measurements were performed on samples with an illuminated pixel area of 13.3 mm².

e) Quantum Efficiency and Quasi-Fermi Level Splitting:

Another essential set of measurements in perovskite solar cells involves the External Quantum Efficiency (EQE) and Luminescence Quantum Yield (LuQY), both of which provide critical insights into device performance and loss mechanisms. One is EQE, which quantifies the ratio of incident photons that are successfully converted into collected charge carriers at each wavelength, providing a spectral fingerprint of the device's photo response. The EQE at a specific wavelength is given by:

$$EQE(\lambda) = \frac{I_{ph}(\lambda)}{q.\Phi_{inc}(\lambda)}, \quad (2.10)$$

where $I_{ph}(\lambda)$ is the photocurrent generated at wavelength, q is the elementary charge (1.602×10^{-19}C), and $\Phi_{inc}(\lambda)$ is the Incident photon flux at a specific wavelength, which is a key performance metric.

Therefore, the total EQE, which is the device's performance across the entire solar spectrum, is the same as the total current contribution of the whole spectrum, expressed as:

$$EQE_{tot} = J_{SC} = \mathrm{q} \int EQE(\lambda)\, S(\lambda) d\lambda, \quad (2.11)$$

where J_{SC} is the short-circuit current density (A/m²), q is the elementary charge (1.602×10^{-19}C), EQE(λ) is external quantum efficiency at wavelength, and S(λ) spectral photon flux of the light source.

The second is internal quantum efficiency (IQE) which is the ratio of charge carriers collected by the solar cell to the number of photons absorbed by the cell. It isolates internal processes by excluding reflection and transmission losses, unlike External Quantum Efficiency (EQE), which includes them. The relationship between EQE and internal quantum efficiency (IQE) is given by the wavelength-dependent absorptance α(λ):

$$IQE(\lambda) = \frac{EQE(\lambda)}{a(\lambda)}, \tag{2.12}$$

where IQE(λ) is internal quantum efficiency, EQE(λ) is external quantum efficiency, and α(λ) is reflectance at wavelength λ.

Another critical analysis in perovskite solar cells is the estimation of Quasi-Fermi Level Splitting (QFLS), which reflects the maximum achievable open-circuit voltage under illumination. QFLS describes the energy difference between the electron and hole quasi-Fermi levels in a non-equilibrium state and is directly linked to the absorber's radiative recombination efficiency. It can be extracted from photoluminescence Quantum Yield (PLQY) measurements, which quantify the ratio of emitted photons to absorbed photons under solar-like excitation. In ideal cases, LuQY approaches the PLQY measured under open-circuit conditions, where all photogenerated carriers recombine radiatively. The QFLS can be estimated using the following relation:

$$QFLS = k_B T.In\left(\frac{1}{PLQY}\right) + E_g - \Delta E_{rad} \tag{2.13}$$

Here, K_B is Boltzmann's constant, T is the absolute temperature, E_g is the bandgap of the absorber, and ΔE_{rad} accounts for radiative losses due to imperfect

outcoupling or reabsorption. A high PLQY suggests minimal non-radiative losses and strong quasi-Fermi level splitting, which translates into a high V_{OC}. Conversely, a significant drop in PLQY indicates increased non-radiative recombination, often at interfaces or transport layers.

2.3 Lead-Tin Mixed Perovskite Solar Cells

This thesis focuses on Pb–Sn mixed perovskite solar cells, which offer a promising pathway toward low-bandgap absorbers suitable for tandem architectures. A key factor governing the performance of Pb–Sn mixed perovskite solar cells is the interaction between lead and tin within the absorber lattice. Variations in the Pb–Sn ratio strongly influence bandgap tuning, defect formation, and charge-carrier dynamics. To clarify these effects, the following subsection examines the impact of lead–tin alloying on the optoelectronic properties of the perovskite absorber.

2.3.1 Impact of Lead-Tin Alloying in Perovskite Absorber

I) Bandgap tuning: According to the Shockley–Queisser (SQ) limit, the optimal bandgap for single-junction solar cells is approximately 1.34 eV.[78] As shown in Figure 2.9b, conventional lead halide perovskites typically possess wider bandgaps, which fall outside this ideal range, thereby limiting their theoretical efficiency. To address this, the incorporation of tin into lead-based perovskites has attracted growing research interest, as it enables bandgap narrowing toward the SQ optimum. This compositional tuning not only enhances the utilization of the solar spectrum in single-junction devices but also facilitates the development of all-perovskite tandem architectures. Moreover, the partial substitution of lead with tin offers a pathway to reduce Pb-related toxicity during device fabrication. Mixed Pb–Sn halide perovskites thus hold significant promise for achieving higher efficiency, improved stability, and scalable integration in both single-junction and monolithic all-perovskite tandem solar cells.[79] Perovskite can be

tuned to as low as 1.2 eV by simply alloying the B-site cation (Sn and Pb) in a proper ratio. If Cs is used as the A-site cation and Br, Cl, or I is used as X, the bandgap can be tuned as high as 3.06 eV.[80]

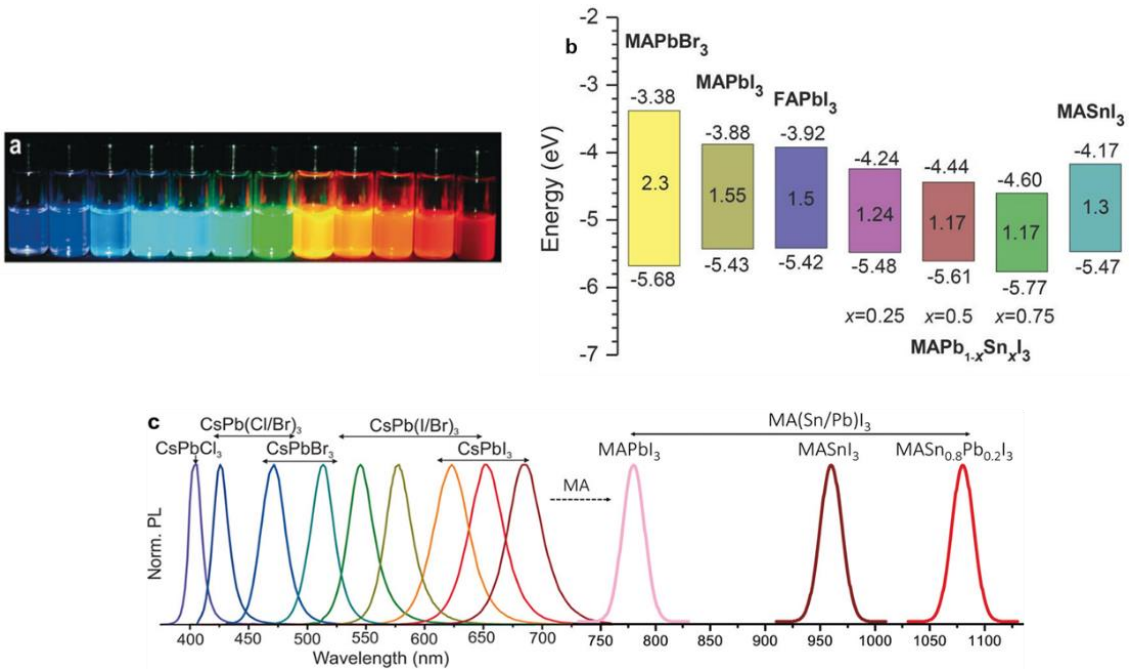

***Figure 2.9**: Tunable band gaps for ABX_3 structures of perovskite with various energy ranges. A colloidal library of $CsPbX_3$ (X = Cl, Br, I) solutions under UV illumination (a). Energy level alignment of representative perovskite compositions: $MAPbBr_3$, $MAPbI_3$, $FAPbI_3$, $MAPb_{1-x}Sn_xI_3$, and $MASnI_3$, (b) reproduced from reference[81] copyright ©2014 WILEY-VCH Verlag GmbH & Co. KGaA, Weinheim (c) Representative PL spectra of $CsPbX_3$ extended to $MA(Sn/Pb)I_3$ perovskites. (a) and (c) reproduced from the reference.[82]*

As shown in Figure 2.9a and c, the colloidal $CsPbCl_3$ and $CsPbI_3$ exhibit PL peaks at 405 nm (3.06 eV) and 700 nm (1.77 eV), respectively. The peaks for $MAPbI_3$ and $MASnPbI_3$ on Sn/Pb metal are at 780 nm (1.59 eV) and 960 nm (1.29 eV), respectively. Remarkably, due to these compounds' band-gap anomaly, $MASn_{0.8}Pb_{0.2}I_3$ exhibits the most significant red-shifted peak at 1080 nm (1.15 eV). Zhao et al. measured the PL peak position in Sn/Pb perovskites.[83]

II) Reducing toxicity: Lead toxicity remains a critical concern in the development

and deployment of perovskite solar cells, prompting extensive research into mitigation strategies. One promising approach involves the partial substitution of Pb with Sn, forming mixed Pb–Sn halide perovskites that reduce the overall Pb content while maintaining high photovoltaic performance. This compositional tuning lowers the overall Pb content of perovskite, thereby reducing its toxicity while preserving high photovoltaic performance.[84] In addition to material substitution, encapsulation techniques are used to prevent lead leakage during operation, including multilayer barrier coatings and self-healing polymers.[85] Lifecycle safety is further addressed through recycling protocols and recovery systems designed to capture and reuse lead from decommissioned devices.[86]

III) Compatible with tandem architectures: Lead–tin mixed perovskites are highly suitable as narrow-bandgap absorbers in monolithic all-perovskite tandem solar cells, owing to their tunable bandgap, improved crystallinity, and enhanced interface quality. Introducing a two-dimensional seed layer to guide vertical crystal growth in $FA_{0.7}MA_{0.3}Pb_{0.5}Sn_{0.5}I_3$ films, significantly improving buried interface contact and charge extraction, key factors for efficient bottom-cell integration.[87] Complementing this, a study by Yang et al. addressed crystallization barriers in Sn–Pb perovskites by optimizing DMSO content, enabling synchronous crystallization and yielding a certified tandem efficiency of 28.87%.[88] Meanwhile, Temitmie et al. reported the use of PTAA as an interlayer between the HTL and the active layer to address the open circuit voltage, resulting in a 0.82 V with a bottom-cell efficiency of 20.3% and applicable for all-perovskite tandem with an efficiency of 25.0%.[89]

2.3.2 Critical Issues Facing Lead-Tin Mixed Perovskite Solar Cells

Instability: One of the most significant challenges to deploying perovskite solar cells for large-scale power generation[90] and achieving high commercial[91] viability is their limited operational stability. This instability is primarily triggered by environmental and operational stressors, including moisture, oxygen exposure,

elevated temperatures, continuous illumination, and ion migration within the perovskite layer, as shown in Figure 2.10a. PSCs degrade in the presence of oxygen and moisture, which is a complex problem. The organic components in PSCs may oxidize if oxygen levels exceed a specific threshold. It was demonstrated that oxygen in a dark atmosphere has no negative effects on PSC stability.[92] Photo-oxidation occurs more frequently when the oxidation rate exceeds the electron transfer rate. In a photo-oxidation comparison study of several PSC topologies, planar structures yielded the most promising results due to faster electron transfer rates.[93]

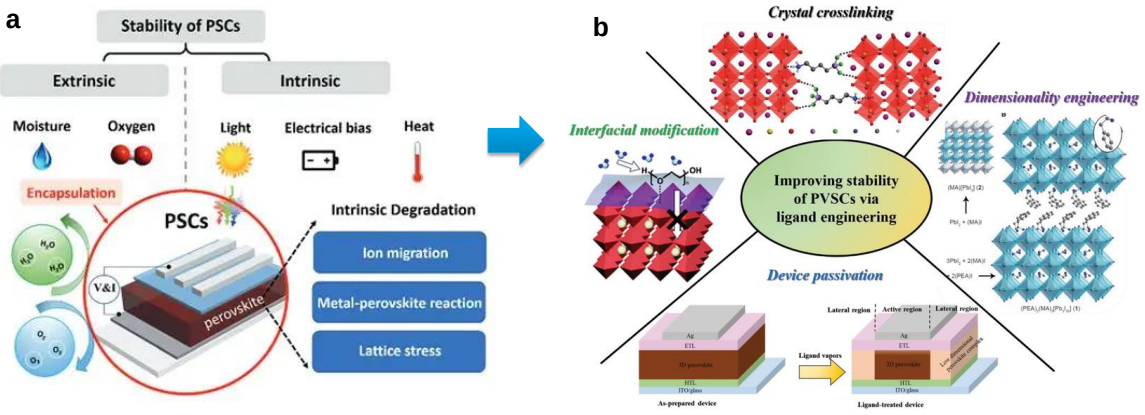

***Figure 2.10**: Key challenges contributing to the instability of perovskite solar cells include intrinsic factors such as electrical bias, heat, and light exposure, and extrinsic factors such as moisture, oxygen, and encapsulation limitations are reproduced from reference[94] (a) and Proposed mitigation strategies to address these issues include interfacial modification, defect passivation, crystal crosslinking, and dimensional engineering (b) reproduced from reference[95] copyright 2018, Royal Society of Chemistry.*

As illustrated in Figure 2.10b, mitigation strategies to address these challenges include interfacial modification, defect passivation, crystal crosslinking, and dimensional engineering. According to the report by Lanzetta et al., the reverse-bias stability of tin–lead perovskite solar cells is significantly enhanced by incorporating a Cr/Cu bilayer at the electron-selective contact, effectively mitigating iodine-induced degradation and increasing the thermal breakdown

voltage.[96] While interfacial engineering strategies such as Cr/Cu bilayers can substantially improve device stability, the overall performance of Pb–Sn perovskite solar cells is also strongly governed by electronic band alignment at the charge-selective contacts. In this context, energy-band misalignment is another critical limitation.

Energy band misalignment: A critical factor affecting the performance of lead-tin mixed perovskite solar cells, particularly in tandem and low-bandgap applications. These mixed perovskites are attractive due to their tunable bandgap and potential for eco-friendly alternatives to lead-only perovskites. However, integrating Sn introduces challenges in energy level alignment, charge transport, and stability. One major challenge arises from the intrinsic p-type doping caused by tin vacancies. This leads to a mismatch in band bending between the surface and bulk of the perovskite film. A recent study by Hu et al. demonstrated that selective surface polishing can reverse band bending and enhance surface electron mobility, thereby mitigating this misalignment and improving charge extraction.[97]

Another critical factor is the alignment between the perovskite layer and adjacent transport layers as presented in Figure 2.11. Simulations by Liu et al. showed that poor energy-level alignment at the perovskite–transport-layer interfaces increase interfacial recombination rates. Optimizing these interfaces, especially by using tailored hole- and electron-transport materials, can significantly reduce energy losses.[98]

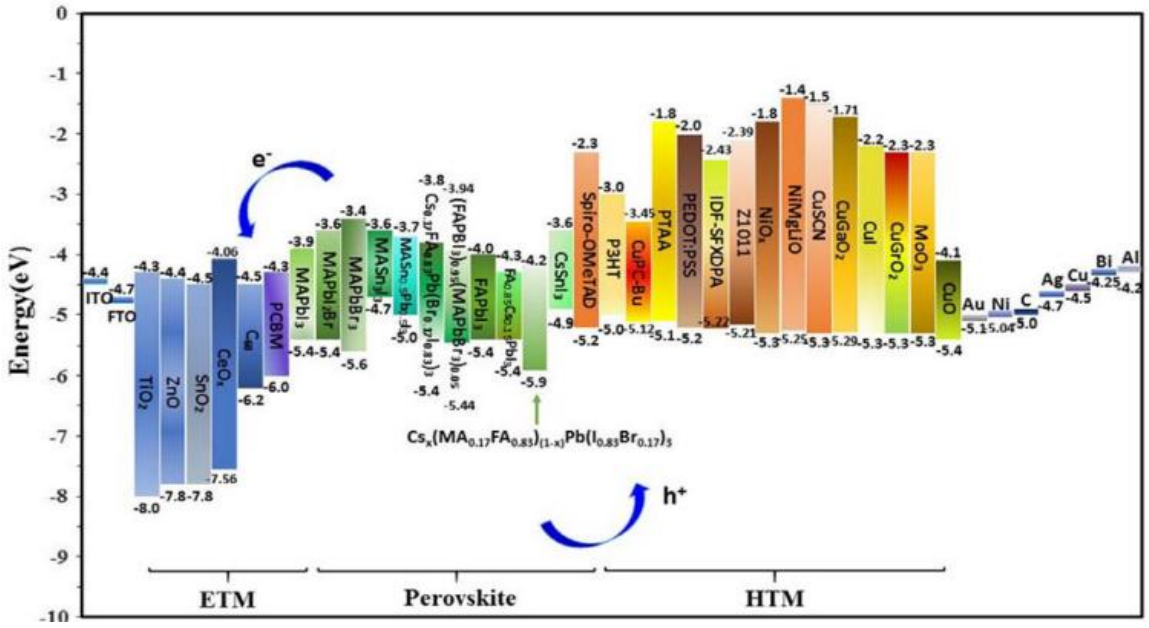

***Figure 2.11**: Energy level alignment between various common HTMs, ETLs, and perovskites.[99] Copyright 2019, Solar RRL.*

Oxidation of Tin (Sn): In lead-tin mixed perovskite solar cells, the oxidation of Sn^{2+} to Sn^{4+} is a significant degradation pathway that directly contributes to the formation of tin vacancies, as shown in Figure 2.12a. These vacancies act as deep-level traps, promoting non-radiative recombination and reducing carrier lifetimes. The presence of Sn^{4+} destabilizes the perovskite lattice and shifts the Fermi level, leading to p-type self-doping and increased background current.

According to the study by Kim et al. (2025), Sn^{4+} formation increases defect density and accelerates device degradation, especially under ambient conditions.[100] In tin-based perovskite solar cells, the inverted (p–i–n) structure is generally more effective at mitigating Sn^{2+} oxidation compared to the conventional (n–i–p) structure. Since holes are oxidizing, their buildup near the tin-based perovskite accelerates the oxidation of Sn^{2+} to Sn^{4+}, a process that degrades the material and reduces device stability. As illustrated in Figure 2.12b, light exposure initiates charge separation, which tends to be more prominent at the

As illustrated in Figure 2.12b, light exposure initiates charge separation, which tends to be more prominent at the $FASnI_3$/ETL interface in the standard device and at the $FASnI_3$/HTL interface in the inverted configuration. This figure suggests that in the standard structure, holes are primarily extracted at the bottom interface, while in the inverted setup, electrons are extracted from the corresponding top interface. Due to this difference, the typical architecture is more prone to Sn^{2+} oxidation driven by hole accumulation, making the inverted structure a more favorable choice for enhancing the stability of tin-based perovskite solar cells. Zhu et al. demonstrated that incorporating SnF_2 as an additive, along with trimethylamine as a co-additive, significantly improved the stability and performance of planar $FASnI_3$-based perovskite solar cells. Their results showed that the inverted device architecture achieved a notably higher power conversion efficiency (PCE) of 7.09%, compared to 4.34% for the standard structure, reinforcing the advantage of the inverted configuration for tin-based PSCs.[101]

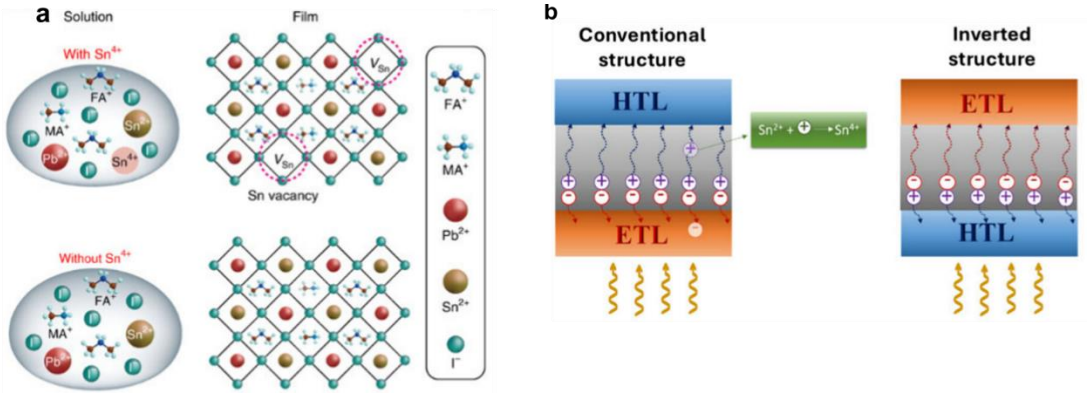

***Figure 2.12**: (a) Schematic depiction of tin (Sn) vacancy defect formation in mixed Pb–Sn perovskites, driven by the presence of Sn^{4+} in the precursor solution. In contrast, Sn vacancy formation is suppressed in tin-reduced formulations due to the absence of Sn^{4+}, and reproduced with permission from.[102] © 2019 Nature Publishing Group (b) Illustration of Sn^{2+} oxidation in Sn-containing PSCs under illumination, comparing conventional and inverted device structures.[103] Copyright © 2019 American Chemical Society.*

Yang et al. introduced sulfaguanidine (SG) as a multifunctional additive to

enhance the performance and stability of Sn–Pb mixed perovskite solar cells. SG plays a dual role: it effectively suppresses the oxidation of Sn^{2+} to Sn^{4+} and simultaneously regulates the crystallization kinetics during film formation. The molecular structure of SG allows it to coordinate with tin ions, stabilizing their oxidation state and reducing the formation of defects. Additionally, SG slows the crystallization process, helping balance the reaction rates between the tin and lead precursors. This additive leads to more uniform crystal growth, improved film morphology, and reduced phase segregation. As a result of these synergistic effects, the modified bottom cell achieved a high and stable power conversion efficiency of 22.70%, highlighting SG's potential as a strategic additive for advancing tin–lead perovskite photovoltaics, and the integrated monolithic tandem device achieved 28.73% efficiency**,** with improved operational stability under AM1.5G illumination.[104]

Defect: Defects in Pb-Sn mixed perovskites play a pivotal role in determining device performance, stability, and carrier dynamics. These defects, both intrinsic (e.g., vacancies, interstitials) and extrinsic (e.g., impurities, grain boundaries), can act as non-radiative recombination centers, trap states, and pathways for ion migration, all of which degrade photovoltaic efficiency. A first-principles study by Liu et al. revealed that intrinsic defects such as tin vacancies and iodine interstitials are particularly detrimental in mixed Pb-Sn systems. These defects distort the local lattice and introduce deep-level trap states, accelerating charge-carrier recombination. Interestingly, the study also showed that Pb incorporation can mitigate some of the dynamic disorder caused by Sn-related defects, improving structural stability.[105]

The distinct chemical properties of lead (Pb) and tin (Sn) contribute to lattice mismatch in Pb–Sn mixed perovskites, posing challenges to structural uniformity. Additionally, the oxidation of Sn^{2+} leads to grain contraction and induces residual strain in the crystal lattice, thereby adversely affecting charge-transport efficiency. Another critical issue arises from the relatively weaker Sn–I bond, as

its lower binding energy compared to Pb–I increases the likelihood of bond breakage. This instability can result in the formation of A-site vacancies, further compromising the structural and electronic integrity of the perovskite layer.[106] Defect passivation strategies are essential to counter these effects. Wang et al. reviewed various passivation approaches, including molecular additives, surface treatments, and interface engineering. They emphasized that defect passivation not only improves carrier lifetimes but also enhances long-term operational stability, especially under illumination and thermal stress.[107] Lin et al. proposed a strategy involving the incorporation of a small amount of tin(II) powder into the precursor solution to mitigate Sn vacancies in low-bandgap Sn–Pb mixed perovskite films. This approach effectively enhanced film quality and device performance, yielding a power conversion efficiency (PCE) of 21.1%.[108]

Open circuit voltage losses: Despite their promise as low-bandgap absorbers for tandem architectures, Pb–Sn mixed perovskite solar cells consistently exhibit V_{OC} losses that limit their practical efficiency. These losses stem from a combination of intrinsic material properties, defect chemistry, and interfacial recombination dynamics. Pb–Sn perovskite solar cells exhibit higher J_{SC} due to their extended photon absorption range; however, this advantage is offset by a compromised V_{OC}, which remains a key performance limitation. This is mainly due to Sn^{+2} oxidation, poor crystallinity, and defects. V_{OC} loss can be expressed as:

$$V_{OC}loss = \frac{E_g}{e} - V_{OC} \tag{2.14}$$

Where E_g is optical bandgap of perovskite with unit of eV, e is elementary charge. A central focus in enhancing the performance of Pb–Sn perovskite solar cells has been the development of strategies to improve their V_{OC}. Reducing V_{OC} losses not only increases V_{OC} levels but also positively affects other key performance metrics of the device. In particular, the oxidation of Sn^{2+} to Sn^{4+}

generates tin vacancies, which act as deep-level traps and facilitate non-radiative recombination, thereby reducing the quasi-Fermi level splitting. This phenomenon is exacerbated by the narrow bandgap (~1.25–1.3 eV) of Pb–Sn alloys, which inherently limits the maximum achievable Voc. My recent study, Temitmie et al., demonstrated that interface engineering is critical to mitigating these losses.[89] By modulating the nucleation dynamics and reducing the density of recombination-active sites, we achieved improved Voc values and enhanced device stability. Furthermore, energy-level misalignment at the perovskite–transport-layer interfaces contribute significantly to interfacial recombination. Addressing these challenges through additive engineering, surface passivation, and tailored interface energetics remains essential for approaching the radiative V_{OC} limit in Pb–Sn mixed perovskite systems.[109,110] Adharsh et al. incorporated DF-C60 into the antisolvent during film formation to create a graded heterojunction, effectively passivating defects in Pb–Sn mixed perovskite layers and achieving a notable V_{OC} of up to 0.89 V.[111]

Uncontrolled crystallization: The crystallization of lead–tin mixed perovskites is a critical process that directly influences film morphology, defect density, and ultimately the performance and stability of perovskite solar cells. Unlike pure lead-based perovskites, Pb–Sn alloys exhibit more complex crystallization dynamics due to the differing ionic radii, oxidation tendencies, and solvation behaviors of Pb^{2+} and Sn^{2+}.

One of the central challenges is the asynchronous crystallization of Pb and Sn precursors. As reported by Zhang et al., this mismatch leads to inhomogeneous nucleation and phase segregation, resulting in poor film uniformity and increased trap densities. To address this, the authors introduced a noncovalent binding agent that selectively binds to unsaturated Sn(II) solvates, thereby synchronizing the crystallization of Pb and Sn species. This strategy yielded high-quality films with reduced defects and enabled a certified PCE of 24.13% in single-junction devices.[112]

In perovskite solar cell fabrication, quenching refers to rapidly supersaturating the precursor solution to induce controlled crystallization. Traditionally, this is achieved using antisolvent dripping. Still, for Pb–Sn mixed perovskites, gas quenching has emerged as a superior alternative due to its enhanced control over film formation and reduced defect density. Gas quenching involves blowing dry inert gas (typically N_2) across the wet perovskite film during spin coating. This rapidly removes solvent, triggering uniform nucleation and crystallization. In Pb–Sn systems, where Sn^{2+} is prone to oxidation and phase segregation, gas quenching offers several advantages: improved film uniformity,[113] and is compatible with large-area deposition and printing techniques, making it attractive for industrial-scale tandem devices.[114]

2.3.3 Strategies to Overcome Issues in Pb-Sn Mixed Perovskite Solar Cells

Lead–tin mixed perovskite solar cells offer a promising pathway toward low-bandgap absorbers, but they face several intrinsic challenges that limit their efficiency and stability. Achieving high-quality Pb–Sn perovskite films remains a significant challenge. To address these issues, researchers have developed a range of mitigation strategies, as shown in Figure 2.13. In recent years, extensive research has focused on enhancing both the perovskite layer and the charge interface in low-bandgap Pb–Sn mixed perovskite solar cells to improve overall device performance.[115,116,117]

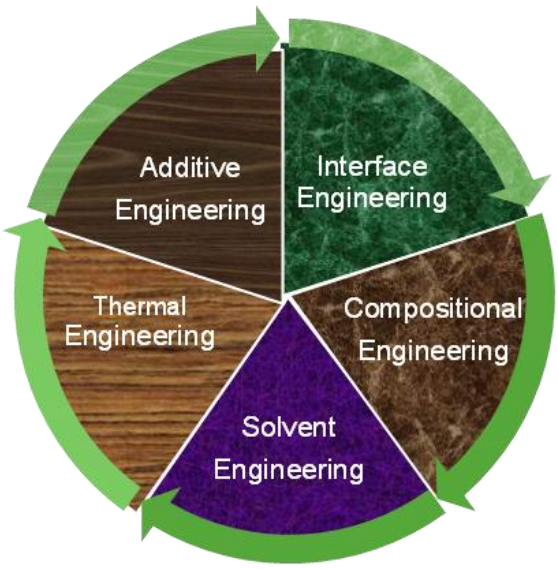

***Figure 2.13**: Schematic summary of five key engineering strategies employed to address the challenges in lead–tin (Pb–Sn) mixed perovskite solar cells: additive engineering to suppress Sn^{4+} and tin vacancy defects; thermal engineering to optimize annealing and improve crystallinity; interface engineering to reduce recombination and enhance charge extraction; compositional engineering to tune bandgap and stabilize the perovskite phase; and solvent engineering to control film morphology and grain growth.*

Additives:

Tin fluoride (SnF_2) is widely used in Pb–Sn mixed perovskite formulations to suppress the oxidation of Sn^{2+} to Sn^{4+}, which otherwise leads to deep-level trap formation and severe non-radiative recombination. SnF_2 acts as a reducing agent and stabilizer, passivating undercoordinated Sn sites and mitigating the formation of tin vacancies. According to Pious et al., SnF_2 tends to accumulate near the surface, where it plays a key role in surface passivation and crystallization control.[118] Additionally, Chen et al. further demonstrated that SnF_2 improves the optoelectronic quality of low-bandgap Pb–Sn films, enabling tandem devices with high efficiency.[119,120] Furthermore, $SnCl_2$ serves as a valuable additive in tin-containing perovskite formulations, primarily due to its ability to suppress tin oxidation and reduce defect density.

The chloride ions, with their high electronegativity, interact with neighboring Sn^{2+} ions in the perovskite lattice, helping to stabilize their oxidation state and prevent

their conversion to Sn^{4+}. This chemical interaction mitigates the formation of tin vacancies, which are known to act as non-radiative recombination centers. Moreover, $SnCl_2$ can influence the crystallization process by promoting more uniform nucleation, thereby improving film morphology and enhancing surface coverage. However, excessive amounts of $SnCl_2$ may lead to phase segregation, with additive-rich domains forming on the surface, which can negatively affect device performance.[121,122,123] The addition of high-purity tin (Sn), particularly in the form of SnI_2 with 99.999% purity, facilitates the formation of high-quality lead–tin (Pb–Sn) mixed perovskite films. This strategy not only improves the incorporation of Sn into the perovskite lattice but also helps suppress defect formation, especially tin vacancies, which are detrimental to charge transport, as shown in Figure 2.12a. As a result, the mixed Pb–Sn perovskite exhibits markedly improved device performance, achieving a PCE of 6.75%, a substantial increase over the 2.90% obtained from the control device using SnF_2 alone.[124]

Passivation and Interface modification: Passivation of both the top surface and buried interfaces is crucial to suppress trap-assisted recombination and improve device longevity. Top-surface passivation often involves chemical polishing or ligand treatments to modulate stoichiometry and reduce surface defects. For example, BDA-based polishing has been shown to minimize non-radiative recombination and improve surface quality.[125] Bottom interface passivation using 2D materials or SAMs helps stabilize the contact and reduce interfacial losses. Li et al. demonstrated that halide-rich treatments and molecular ligands can effectively passivate both bulk and surface defects.[126]

A recent review by Huang et al. emphasized the role of 2D perovskites in interface passivation for high-performance PSCs.[127] Yang et al. demonstrated that a synergistic approach combining compositional, process, and interfacial engineering significantly enhances perovskite film quality. By employing a B-site cation ratio of 75% Pb and 25% Sn, along with varying the A-site cation composition between methylammonium (MA) and formamidinium (FA), they

achieved improved film morphology. The optimal device performance was obtained using the composition $MA_{0.5}FA_{0.5}Pb_{0.75}Sn_{0.25}I_3$, which exhibited a bandgap of 1.33 eV, a PCE of 14.2%, and commendable dark-shelf stability.[128] Liu et al. introduced a ZnO layer as a cathode buffer layer (CBL) between the perovskite and PCBM interface to inhibit silver diffusion into the perovskite layer. This modification effectively minimized the energy level mismatch between the electron-selective layer (ESL) and the perovskite absorber. As a result, the device achieved a PCE of up to 18.1% and an enhanced V_{OC} of 0.78 V.[129]

Quenching techniques: These methods are used to control the crystallization kinetics of Pb–Sn perovskite films, which is vital for achieving uniform morphology and reducing defect formation. Huang et al. first introduced gas quenching as a film formation technique for $MAPbI_3$ perovskite thin films, achieving a power conversion efficiency (PCE) of 17.0%. This approach established gas quenching as a valuable method for enhancing perovskite film quality and device performance.[130]

Gas quenching, using inert gases like N_2, offers better control, reduces Sn^{2+} oxidation, and is scalable for large-area deposition. Vacuum quenching enables uniform solvent removal and is compatible with roll-to-roll processing. Ternes et al. developed a modeling framework comparing all three methods, showing that gas and vacuum quenching outperform antisolvent in terms of film uniformity and defect suppression.[131]

Werner et al. applied a contact engineering strategy to enhance the interface between the perovskite layer and the hole-transport layers by substituting conventional PEDOT: PSS with PTAA. This modification, combined with perovskite film formation via nitrogen (N_2) gas quenching, led to improved thermal stability and enabled the device to achieve a high-power conversion efficiency of approximately 20%. However, the V_{OC} achieved with this strategy remained lower than that obtained with the commonly employed PEDOT: PSS as the hole-selective layer (HTL).[132,133] H. et al. fabricated low-bandgap perovskite

solar cells using a bilayer HTL composed of PEDOT: PSS and PTAA. However, the study lacked sufficient detail regarding the structural and functional characteristics of the PEDOT: PSS/PTAA bilayer interface. The study aimed to enhance the charge carrier diffusion length by introducing a trace amount of cadmium into the perovskite absorber layer.[134] Recent work by Azhar et al. showed that gas quenching enabled high-quality crystallization due to the occurrence of wrinkling in wide-bandgap Pb–Sn alloys.[135] A study by Werner et al. demonstrated that gas-quenching-grown Sn–Pb perovskite films exhibited superior MA-free Sn–Pb perovskite films morphology and reduced trap-assisted recombination compared to antisolvent-treated films.[136]

2.4 All-Perovskite Tandem Solar Cells

These cells consist of at least two active layers. Tandem solar cells are designed to overcome the Shockley–Queisser limit of single-junction devices by stacking multiple absorbers with complementary bandgaps.[137] In perovskite-based tandems, the most common configurations include perovskite–silicon, all-perovskite, and perovskite–CIGS structures. These architectures aim to maximize light harvesting across the solar spectrum, reduce thermalization losses, and improve overall PCE. According to Aziz, M.W. et al., Perovskite-silicon tandem efficiencies exceed 34%, with growing emphasis on stability, scalable fabrication, and interface engineering.[138] However, all-perovskite tandem solar cells' efficiencies are still lower than silicon - perovskite tandems as shown in Figure 2.14. Moreover, it still has challenges when using scalable fabrication methods, e.g., transferring optimized spin coating (lab scale) to the blade coating (industry scale) process. The main challenges are the higher bromide concentrations in wide-bandgap perovskite precursor solutions and the low solubility, which leads to variable crystallization kinetics.[139]

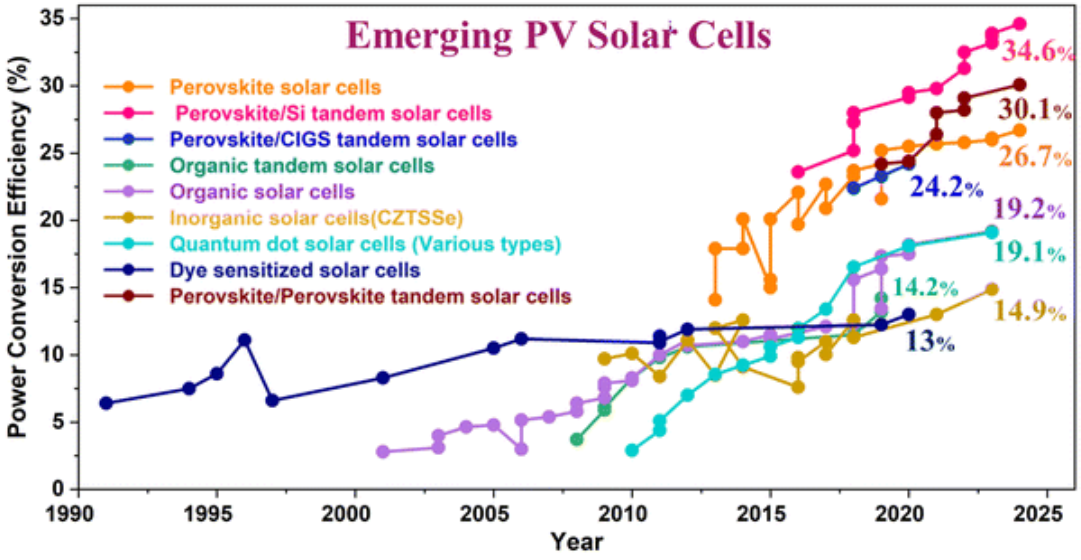

***Figure 2.14**: Recent progress in emerging photovoltaic solar cells (PV SCs), highlighting advancements in perovskite solar cells (PSCs), including record efficiencies in single-junction and tandem configurations, is reproduced from NREL.*[140]

Perovskite–perovskite tandem solar cells are a promising class of next-generation photovoltaics that stack two perovskite layers with complementary band gaps, typically a wide-bandgap (~1.7–1.9 eV) top cell[141,142] and a narrow-bandgap (~1.2–1.3 eV) bottom cell.[143,144]

2.4.1 Four-Terminal All-Perovskite Tandem Solar Cells

As shown in Figure 2.15, the four-terminal (4T) tandem architecture is a mechanically stacked configuration in which two sub-cells, typically a wide-bandgap top cell and a narrow-bandgap bottom cell, operate independently. Unlike monolithic 2-terminal (2T) tandems, 4T designs allow for flexible optimization of each sub-cell without requiring current matching or complex interconnecting layers. This difference makes them ideal for early-stage research and prototyping of perovskite–perovskite tandems. However, challenges remain in terms of optical losses, parasitic absorption, and transparent electrode design.[145] Zhang et al. optimized both wide and narrow-bandgap perovskite compositions and interconnecting layers, significantly improving charge recombination dynamics and overall tandem efficiency. They achieved improved tandem performance with enhanced current matching and reduced

recombination losses.[146]

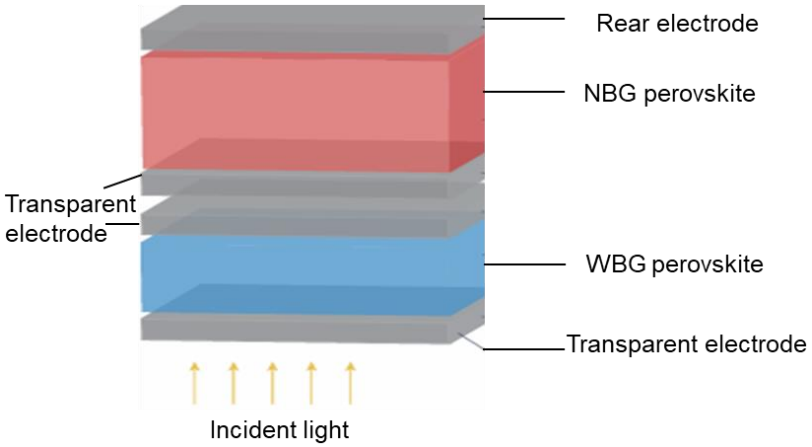

***Figure 2.15**: Four-terminal all-perovskite tandem solar cell architectures, two independent perovskite sub-cells, typically a wide-bandgap top cell and a narrow-bandgap bottom cell, are optically coupled but electrically isolated, are reproduced from reference.[147]*

2.4.2 Two-Terminal All-Perovskite Tandem Solar Cells

As shown in Figure 2.16, the structural and operational principles of two-terminal 2T all-perovskite tandem solar cells, where a WBG perovskite top cell is monolithically stacked over an NBG bottom cell. These sub-cells are electrically connected in series through a common recombination layer, which plays a critical role in facilitating efficient charge transfer between the two junctions while minimizing optical and electrical losses. The device architecture shown in Figure 2.16a presents the vertical integration of the two perovskite absorbers, with careful bandgap selection—typically ~1.80 eV for the WBG top cell and ~1.25 eV for the NBG bottom cell—to ensure optimal current matching and spectral utilization. Figure 2.16b schematically presents the working principles of the 2T tandem configuration, emphasizing the role of the recombination layer in balancing electron and hole flow between the sub-cells and maintaining high open-circuit voltage (V_{OC}) across the tandem stack. The main challenges include

interfacial recombination, Sn^{2+} oxidation in the bottom cell, and phase instability in Br-rich wide-bandgap top cells.[146]

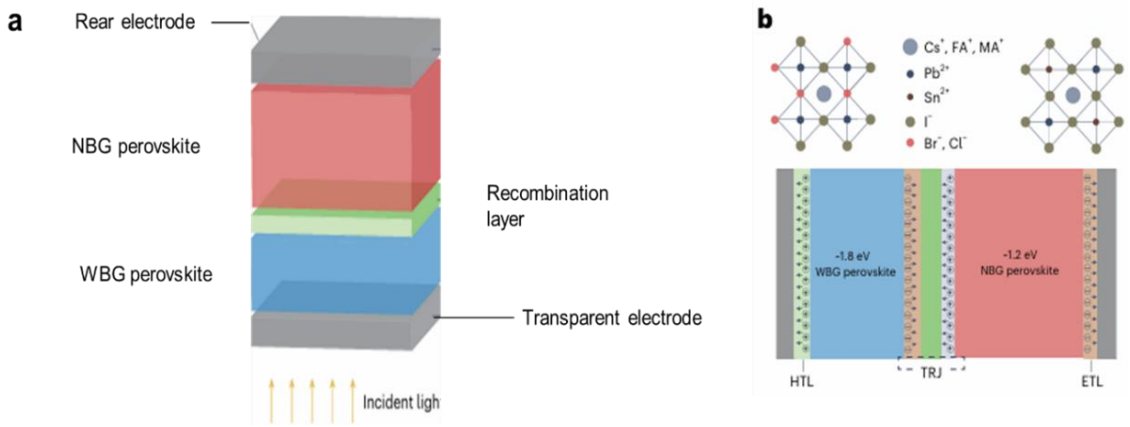

***Figure 2.16**: Two--terminal all-perovskite tandem solar cell architectures, the wide-bandgap as a top cell and narrow-bandgap as a bottom cell are integrated in series, sharing a common recombination layer that facilitates charge recombination and minimizes optical losses. Two-terminal all-perovskite tandem devices (a) and working principles of 2T all-perovskite tandem solar cells (b) are reproduced from reference.[147]*

3 EXPERIMENTAL DETAILS

In this chapter, the experimental methodology employed in the development of NBG perovskite solar cells and all-perovskite tandem architectures is presented. It outlines the materials used, precursor preparation methods, and fabrication strategies, including various quenching techniques, anti-solvent quenching, and gas quenching. The final section presents the characterization methods applied to evaluate both film quality and device performance.

3.1 Materials and Reagents

ITO-coated glass slides (15 Ω/sq) were purchased from Luminescence Technology Corp (thickness, 2 mm). PEDOT: PSS water dispersion under the commercial name of Clevios PVPAI 4083 was purchased from Heraeus. Lead (II) thiocyanate ($Pb(SCN)_2$, 99.5%), tin (II) fluoride (SnF_2, >99%), and magnesium fluoride (MgF_2, 99.9%) were purchased from Sigma-Aldrich. Methylammonium iodide (MAI, >99%) and formamidinium iodide (FAI) (>99%) were purchased from Greatcell Solar. Tin (II) iodide (SnI_2, 99.999%) was purchased from Thermo Scientific. Lead (II) iodide (PbI_2, 99.99%) was purchased from TCI Chemicals. Meo-2PACz (>98%), 2PACz (>98%) purchased from TCI chemicals. Silver (Ag), lead chloride ($PbCl_2$), cesium iodide (CsI, 99.9%), and lead bromide ($PbBr_2$, 99.9%) were purchased from Sigma-Aldrich. Poly[bis(4-phenyl)(2,4,6-trimethylphenyl)amine] (PTAA, >99%), buckminsterfullerene (C_{60}, >98.5%), and bathocuproine (BCP, 99.0%) were acquired from Ossila. Absolute ethanol was purchased from VWR. Dimethylformamide (DMF, anhydrous, 99.8%), dimethyl sulfoxide (DMSO, anhydrous,>99.7%), toluene (anhydrous, 99.8%), Chlorobenzene (CB, anhydrous, 99.8%), and diethyl ether (anhydrous, 99.8%) were purchased from Sigma-Aldrich.

3.2 Preparation of Lead-Tin Mixed Perovskite Precursors

The Sn-Pb perovskite with the composition $(FASnI_3)_{0.6}(MAPbI_3)_{0.4}$ was prepared by mixing $FASnI_3$ and $MAPbI_3$ solutions in a volume ratio of 0.6:0.4, as described Figure 3.1. For the $FASnI_3$ solution at 1.15 M, 18 mg of SnF_2 (10 mol%), 197.8 mg of FAI, and 428.4 mg of SnI_2 were dissolved in a mixture of 800 µL DMF and 200 µL DMSO, and the mixture was stirred overnight at room temperature.

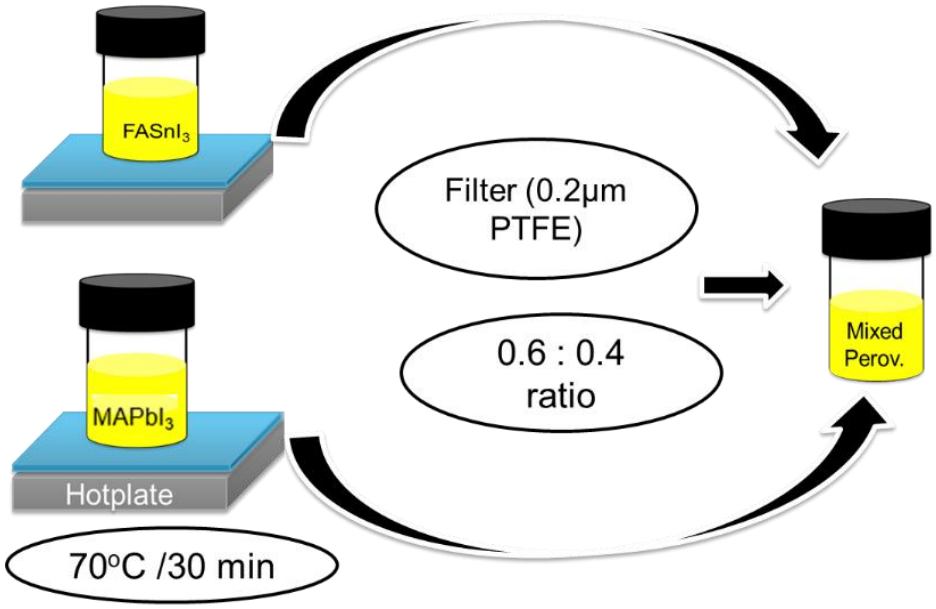

***Figure 3.1**: A general schematic demonstrating the preparation technique for the perovskite precursor solution used in this thesis.*

For the $MAPbI_3$ solution with a concentration of 1.15 M, 530 mg of PbI_2, 183 mg of MAI, and 3.5 mol% Pb $(SCN)_2$ additive were dissolved in 630 µL DMF and 70 µL DMSO, and the mixture was stirred for 30 min at 70°C and then stirred overnight at room temperature. Subsequently, the $FASnI_3$ precursor solution was filtered through a 0.2 µm PTFE filter, and then the two precursors were combined using a 0.6:0.4 $FASnI_3$:$MAPbI_3$ ratio. The resulting Sn-Pb precursor solution was stirred at room temperature for 30 min before use.

3.3 Fabrication of Lead-Tin Mixed Perovskite Solar Cells

The ITO substrates were cleaned for 30 min using detergent, deionized water, acetone, and IPA under ultrasonication in the following order. After being dried by nitrogen flow, the substrates were treated with UV-Ozone for 20 min. For the PEDOT: PSS deposition, the purchased dispersion was filtered through a 0.45 μm PVDF filter. The dispersion was deposited onto the cleaned ITO substrates by spin coating at 8000 rpm for 40 s, followed by annealing at 120°C for 15 min. After the deposition and annealing under ambient air, the substrates were quickly transferred into the glovebox. For PTAA-only devices, the PTAA solution was spin-coated onto the cleaned ITO substrates at 8000 rpm for 40 s, followed by annealing at 100°C for 3 min. For bilayer-based devices, a PTAA thin film was spin-coated onto PEDOT: PSS (bilayer) at 8000 rpm for 40 s, then annealed at 100°C for 3 min. Before perovskite deposition, the device stacks featuring PTAA on top (either PTAA-only or bilayer) were treated with O_2 Plasma for 2.5 s to mitigate PTAA's poor wettability.

3.3.1 Anti-Solvent Method

As shown in Figure 3.2, the perovskite precursor solution (30 μL) was statically deposited and spin-coated onto the HTLs at 4000 rpm for 60 s. Diethyl ether (700 μL) was used as the antisolvent and was dripped onto the film 15 s after the start of the spin-coating process. All perovskite films were then annealed at 100°C for 10 min.

3.3.2 Gas-Quenching Method

After a 30 μL of perovskite precursor solution was statically deposited and spin-coated onto the hole transport layers (HTLs) at 4000 rpm for 60 s, nitrogen gas was employed to induce perovskite crystallization as presents in Figure 3.2. Among the various pressures tested, the optimal results were achieved with a circular nozzle nitrogen gun with a 1 mm diameter and a regulator pressure of approximately 5 bar. The nitrogen gun was positioned perpendicularly, 4-5 cm above the spinning substrate. After 15 s of spinning the precursor solution, the

substrates were subjected to nitrogen gas blowing for 20 s, followed by an additional 25 s of spinning. All perovskite films were subsequently annealed at 100°C for 10 min.

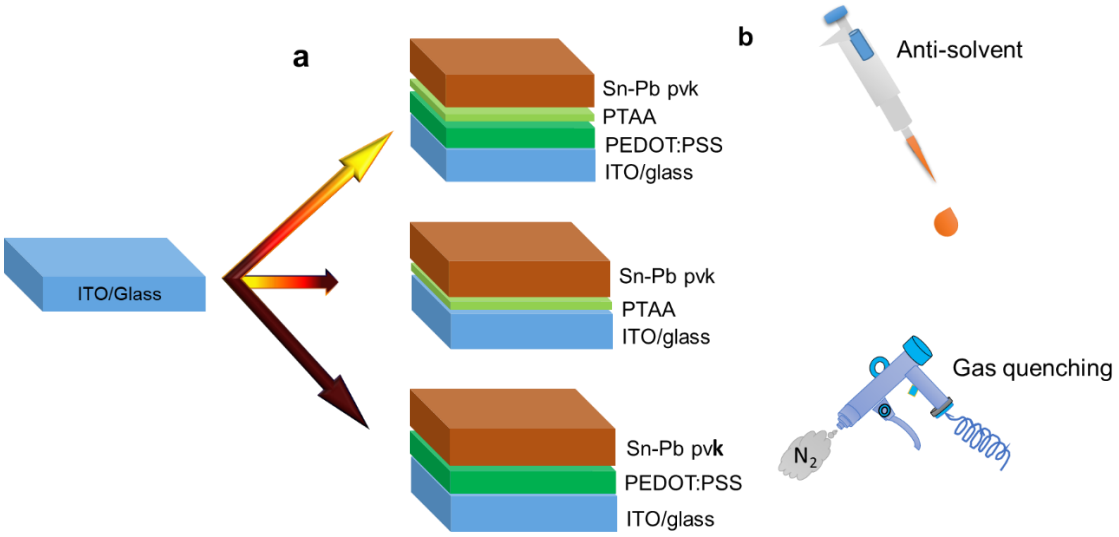

***Figure 3.2**: Schematic illustration of the half-stack architecture of single-junction perovskite solar cells, either a single-layer or bilayer hole transport layer (HTL) (a) and tools for perovskite film crystallization techniques: anti-solvent (AS) treatment and gas quenching (GQ) (b).*

Finally, 25 nm C_{60}, 7 nm BCP, and 100 nm Ag were sequentially deposited on the perovskite films. An optimized 70 nm-thick MgF_2 layer was thermally evaporated on the glass side of PSCs (at a rate of 1 Å/s) as an anti-reflection coating (ARC).

3.4 Fabrication of Wide Bandgap Perovskite Solar Cells

The WBG perovskite solution (1M or 0.9 M) was made by mixing the following precursors in DMF: DMSO (3:1) at around 40°C in a glovebox: $PbCl_2$ (0.02 M), CsI (0.3 M), MAI (0.1 M), FAI (0.6 M), $PbBr_2$ (0.45 M), and PbI_2 (0.55 M). The solution was dissolved entirely and used without any filtering. The WBG PSCs were made on pre-cleaned ITO glass (same as NBG) , and a 0.5 mM equimolar (50:50) mixture of self-assembled monolayers (MeO-2PAC$_Z$ and 2PAC$_Z$) in

ethanol was spin-coated on ITO substrates in a glovebox (3000 rpm for 30 s), followed by annealing at 100°C for 10 min. The perovskite solution (45 µL) was dropped onto a static-cooled ITO substrate, and perovskite crystallization proceeded as follows. A N_2 flushing gun (pressure around 3.5 bar) was placed 2-3 cm above the spinning substrate; N_2 flushing started after 20 s of spinning (after perovskite dropping perovskite solution), and the substrates stayed under N_2 flushing for 15-20 s, until the films turned shiny and dark brown in color. For performance improvement, PEAI (1 or 2 mM) in CB: IPA (9:1) was spin-coated (on spinning substrates) at 5000 rpm for 30 s (no further annealing was carried out). The device stack was completed by sequentially evaporating 25 nm of C_{60} (18 nm for tandem PSCs), 6 nm of BCP, and 100 nm of Ag.

3.5 Fabrication of All-Perovskite Tandem Solar Cells

For tandem PSCs, shown in Figure 3.3a, the device fabrication procedure is the same as that of WBG PSCs until C_{60} deposition (18 nm instead of 25 nm for single junction WBG PSCs). After the deposition of C_{60}, the perovskite films were transferred to an ALD system (Anric AT-410) to deposit SnO_2 in ambient conditions. As a precursor, tetrakis(dimethylamino)tin (IV) (TDMASn) was used at a temperature of 70°C, while water was used as an oxidant. The chamber temperature was set to 70°C. During exposure, a purge flow of 10 sccm was used, while each exposure step was 1 s. One ALD cycle consisted of 3 pulses of precursor, 12 s N_2 purge, two pulses of oxidant, and 15 s N_2 purge. Here, 155 cycles were performed, resulting in thin films with a thickness of 20 nm. The substrates were transferred to a glovebox to deposit Au (0.5 nm) with an edge-covered shadow mask (to avoid shunting between top and bottom cells). The cells were removed to deposit the HTL (PEDOT: PSS) and to build an NBG cell on top. The same NBG cell fabrication procedure (described above) is followed to complete tandem devices.

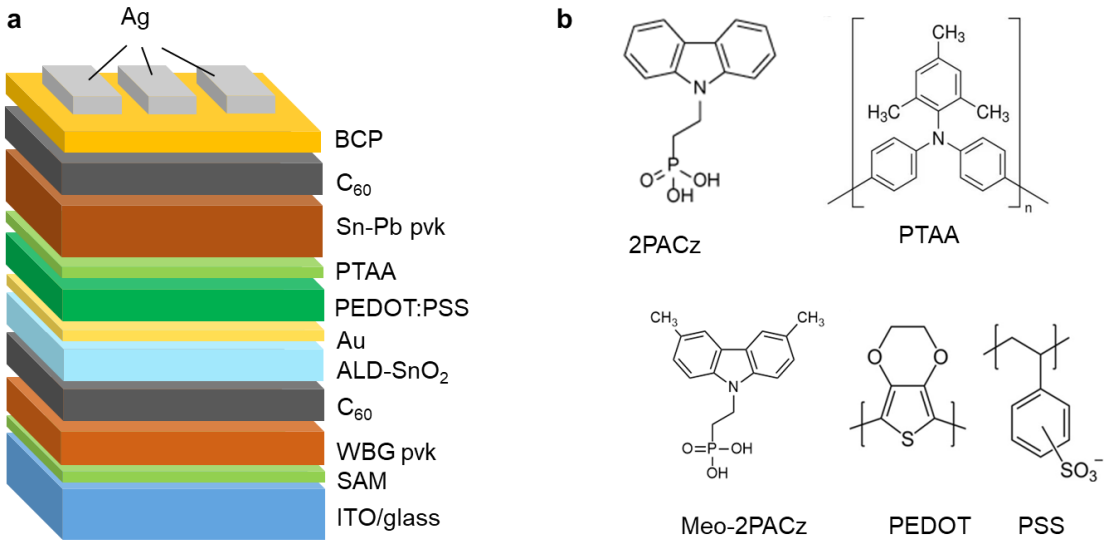

***Figure 3.3**: (a) Schematic illustration of a full-stack all-perovskite tandem solar cell architecture, including a narrow-bandgap perovskite bottom cell and a wide-bandgap perovskite top cell; (b) chemical structure of HTL, 2PACz, Meo-2PACz, Poly (3,4-ethylenedioxythiophene) poly(styrenesulfonate) (PEDOT: PSS), and Poly[bis(4-phenyl) (2,4,6-trimethylphenyl) amine] (PTAA) used in all-perovskite solar cells. Reproduced from reference[89] under CC-BY 4.0*

3.6 Characterization Techniques

This section outlines the analytical methods used to evaluate the optoelectronic properties of perovskite films and solar cell devices. A combination of film-level and device-level characterization techniques was employed to assess material quality, interface behavior, and photovoltaic performance.

3.6.1 Film-Level Characterization Techniques

Photoluminescence quantum yield (PLQY) was measured using a *LuQY Pro* setup from *Quantum Yield Berlin*. Scanning electron microscope (SEM) images were acquired with a *Gemini 500 FESEM* system from *Zeiss* equipped with an in-lens detector. Time-resolved photoluminescence (TRPL) spectroscopy was performed with a *FluoTime 300* setup from *PicoQuant*. An atomic force microscope (AFM) was used in an *NX10* setup from *Park Systems.* Electroluminescence (EL) spectra were measured in a *Phelos* setup from *Fluxim*.

Photoelectron spectroscopy in air (PESA) was conducted on an AC-2 system (Riken Instruments). Furthermore, in-situ transmission measurements were performed during spin coating to monitor film formation dynamics under the two different quenching approaches.

3.6.2 Device-Level Characterization Techniques

The J-V curves of the PSCs were measured under simulated solar illumination at 100 mW cm^{-2}, AM 1.5G equivalent sunlight in a nitrogen-filled glovebox using an assembly made up of a *Keithley* 2400 source-meter unit, a *LOT* 300 W Xenon solar simulator, calibrated with a KG5-filtered Si reference diode (for WBG cells measurement) certified by *Fraunhofer ISE*. Cross-section SEM images were acquired with a *Gemini 500 FESEM* system from *Zeiss* equipped with an in-lens detector. Space-charge limited current (SCLC) measurements were performed by measuring dark J-V curves of hole-only devices with a configuration of (ITO/bilayer/NBG/P3HT/Ag). The external quantum efficiency (EQE) was measured with a Bentham PVE300 setup, by using Arkeo IPCE with tunable (300-1800 nm) light source without light bias and equipped with a 300 W Ozone Free Xe in AC mode having a chopper frequency at 16 Hz. Certified Si (Hamamatsu S1337) and Ge photodiodes were employed for the calibration of the monochromatic light intensity. Maximum power point (MPP) tracking and open-circuit voltage (V_{OC}) rise, and decay analysis were employed to ensure reliable PSC evaluation. Both light and dark J–V curves of the champion device under simulated solar illumination at 100 mW cm^{-2}, AM 1.5G equivalent sunlight and dark condition in a nitrogen-filled glovebox using an assembly made up of a *Keithley* 2400 source-meter unit, a *LOT* 300 W Xenon solar simulator. For the tandem solar cells, the spectra of the two component cells were obtained by applying filtered bias light: red light to saturate the bottom cell and measure the top cell, blue light to saturate the top cell and measure the bottom cell.

4 MITIGATION OF V_{OC} LOSSES IN PB–SN PEROVSKITE SOLAR CELLS

In this chapter, the focus is on the interface between the mixed lead–tin (Pb–Sn) perovskite absorber and the commonly used hole-transport layer (HTL), poly(3,4-ethylenedioxythiophene): polystyrene sulfonate (PEDOT: PSS). To further enhance interfacial properties, a thin layer of poly(triarylamine) (PTAA) is introduced as an interfacial modifier. The study investigates how the presence or absence of this PTAA interlayer influences the open-circuit voltage (V_{OC}) and the overall power conversion efficiency of Pb–Sn mixed perovskite solar cells. By comparing devices with and without the interfacial layer, the analysis highlights the critical role of interface engineering in improving charge extraction and reducing recombination losses, ultimately leading to enhanced photovoltaic performance. The findings discussed in this chapter originate from research published in ACS Materials Letters *and are available under the CC-BY 4.0 license.*

The results presented in this chapter are derived from the article *"Overcoming the Open-Circuit Voltage Losses in Narrow Bandgap Perovskites for All-Perovskite Tandem Solar Cells"*, published in ACS Materials Letters, for which I served as the lead author. This work was carried out in collaboration with Azhar Fakharuddin, Muhammad Irfan Haider, and Daniele T. Cuzzupè, who contributed to data analysis, data visualization, and the preparation of the original manuscript, along with other co-authors. As a prominent author, I contributed by performing experimental work, conducting data analysis, preparing visualizations, and drafting the original manuscript. All co-authors participated in the revision and proofreading of the manuscript, ensuring the quality and clarity of the final publication.

Achieving high-quality Pb–Sn mixed low-bandgap perovskite solar cells is critically hindered by significant open-circuit voltage losses, which pose a central challenge to device performance. The rapid oxidation of Sn^{2+} to Sn^{4+} leads to increased background carrier concentration and self-doping effects, both of

which intensify non-radiative recombination and lower V_{OC} beyond what defect passivation alone can resolve. Moreover, the rapid crystallization typical of low-bandgap perovskites often results in suboptimal film formation and trap-rich surfaces, compounding the V_{OC} deficit rather than simply affecting charge transport. These factors collectively manifest as severe voltage penalties that directly limit power conversion efficiency, even in otherwise promising device configurations. Recognizing this, the present work employs interface engineering to enhance perovskite film quality and effectively suppress surface defects, aiming to boost overall device efficiency.

4.1 Introduction to V_{OC} Loss in Pb–Sn Mixed Perovskite Solar Cells

To date, most highly efficient Sn-Pb mixed PSCs rely on the organic HTL PEDOT: PSS. However, the main problem with relying on PEDOT: PSS as the HTL in highly efficient Sn–Pb mixed perovskite solar cells is that it induces substantial interfacial recombination losses, leading to pronounced open-circuit voltage V_{OC} deficits. PEDOT: PSS has a high intrinsic doping level, which facilitates non-radiative charge-carrier recombination at the perovskite/HTL interface and thus directly limits device efficiency. Furthermore, its acidic nature can compromise the long-term thermal and environmental stability of perovskite devices by promoting degradation reactions, and it often leads to poor energy-level alignment with the absorber, impeding efficient hole extraction. Such limitations can cause compositional segregation within the mixed Pb–Sn perovskite films, degrade film morphology, and reduce crystallinity, thereby further exacerbating V_{OC} loss.[148,149,150] Yang et al. reported that introducing Br^- into the mixed Sn- Pb perovskites can efficiently improve performance and reduce V_{OC} deficits. Solar cells based on the ideal bandgap perovskite, $MAPb_{0.5}Sn_{0.5}(I_{0.8}Br_{0.2})_3$, yielded a PCE of 17.63% with a small V_{OC} deficit of 0.45 V.[151] Using a mixed precursor solution consisting of formamidinium tin iodide

($FASnI_3$) and methylammonium lead iodide ($MAPbI_3$) and a surface passivation strategy using PEABr, the V_{OC} of the devices was improved markedly from 0.71 V to 0.78 V, yielding an efficiency of 15.15%.[152] Yan and coworkers achieved a significant enhancement in the PCE of Sn-Pb PSCs by employing PEDOT: PSS as the HTL, resulting in an impressive PCE of up to 20%.[153]

4.2 Role of PTAA Interlayer Between HTL and Pb-Sn Mixed Perovskite Layer

In this work, we selected poly[bis(4-phenyl) (2,4,6-trimethylphenyl) amine] (PTAA) as an interlayer between the HTLs and the $(FASnI_3)_{0.6}(MAPbI_3)_{0.4}$ perovskite (henceforth termed as “NBG perovskite”) to overcome the open-circuit voltage losses typical of these perovskites and in all-perovskite tandem solar cells, as shown in the next chapter. Hole-transporting layers play a crucial role in perovskite solar cells (PSCs). The choice of the HTL significantly impacts PSC efficiency and stability. Figure 3.3b presents the chemical structures of the four HTLs—2PACz, Meo-2PACz, PTAA, and PEDOT: PSS—used for comparative performance analysis of PSCs. Those HTLs are critical components of inverted p-i-n PSCs, where, alongside hole extraction and transport, they play an essential role in surface passivation, perovskite crystallization, device stability, and cost management.

For this purpose, we systematically compared three-hole transport layer configurations in Pb–Sn perovskite solar cells: devices employing PEDOT: PSS-based, PTAA-based, and bilayer devices incorporating a PTAA interlayer deposited on top of PEDOT: PSS. For the bilayer HTL architecture, we optimized the PTAA concentration by evaluating solutions at 0.1, 0.2, 0.5, 1.0, and 1.5 mg/mL. Our results identified 1.0 mg/mL as the optimal PTAA concentration, yielding the best device performance in terms of open-circuit voltage and overall efficiency. The enhanced efficiency and V_{OC} of the bilayer-based PSCs are attributed to the PTAA layer deposited on top of PEDOT: PSS, which improves

the hole transport properties (compared to PTAA-standalone) and acts as a barrier layer to prevent electron recombination at the perovskite/transport layer interface compared to a PEDOT: PSS-standalone layer, leading to improved charge extraction and reduced recombination losses. The modification of PEDOT: PSS with PTAA also influences the energy-level alignment in perovskite solar cells. The findings demonstrate that a bilayer is an effective way to reduce V_{OC} loss and fabricate efficient PSCs.

4.3 Assessing the Effect of PTAA in Pb-Sn Mixed Perovskite Solar Cells

Screening hole transport layers for high-efficiency PSCs

Initially, a series of HTLs were screened to identify the most effective HTL combination for these devices. The selection criteria included energy-level alignment with the NBG perovskite and consideration of the best-performing HTLs from their Pb-based counterparts. These HTLs included PEDOT: PSS and PTAA, chosen for their potential energy-level alignment with the NBG perovskite and their track record in Pb-PSCs.[154,155] The energy level alignment between the HTL and the perovskite is essential to prevent charge recombination losses. The HTL's valence-band edge should be higher than the perovskite's valence-band edge to enable efficient hole transfer. In comparison, its valence-band edge should be lower than the cathode's conduction-band edge to ensure complete hole extraction.[156]

The ionization energy values of HTLs and NBG perovskite given in Figure S1.2 confirmed a better energy alignment for bilayer and NBG perovskite, assuring a better charge extraction. The PTAA concentrations considered were 0.1, 0.2, 0.5, 1.0, and 1.5 mg/mL, and the corresponding champion V_{OC} values were 0.81 V, 0.79 V, 0.81 V, 0.82 V, and 0.83 V, respectively. While a concentration of 1.5 mg/mL demonstrated the highest V_{OC} among the five concentrations employed in this work, the optimal concentration for achieving a trade-off between V_{OC}, FF, and overall PCE was found to be 1.0 mg/mL. Based on the results shown in

Figure 4.1 (a-d), we chose three HTLs for further investigations, namely PEDOT: PSS-only, PTAA-only (1 mg/mL), and the bilayer HTL employing the PTAA film (concentration of 1 mg/mL) atop PEDOT: PSS.

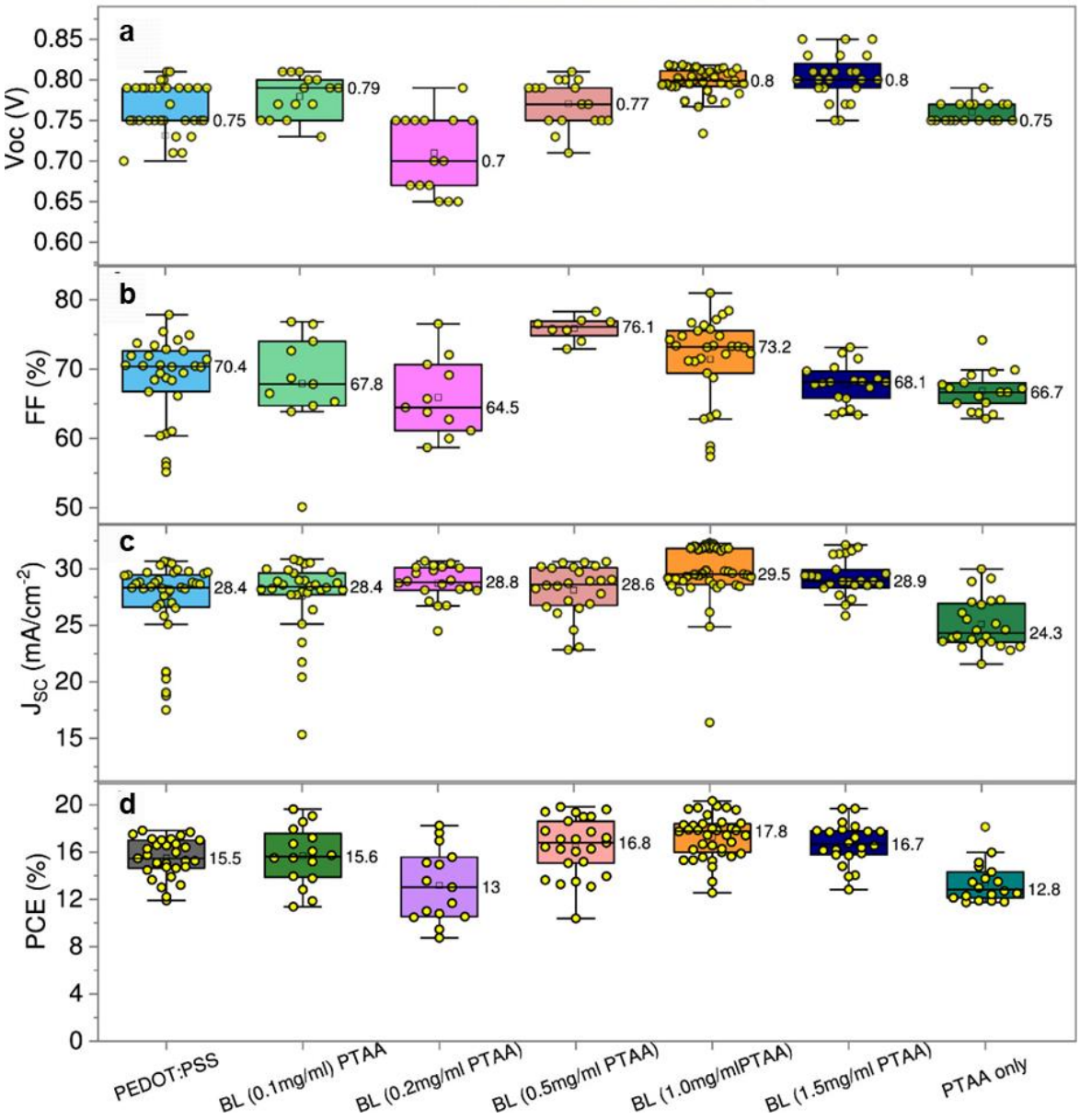

***Figure 4.1**: (a-d) Box chart representing V_{OC}, FF, J_{SC}, and PCE of PSCs employing various HTLs. The data refers to several devices from at least five different batches fabricated in this work. The HTL series 0.1-1.5 mg/mL PTAA refers to the concentration of the HTL precursor solution. The PTAA layers were cast onto PEDOT: PSS to form bilayers (BLs). The concentration of the PTAA-only case is 1.0 mg/mL. The data labels in e-h show mean values. Reproduced from reference[89] under CC-BY 4.0.*

The ionization energy values obtained for the materials investigated in this study are presented in Figure S1.2. PEDOT: PSS exhibits 5.20 eV, consistent with its typical range. The bilayer interface has an energy of approximately 5.06 eV, reflecting the combined properties of both layers. In comparison to other HTLs, the bilayer seemed to be appropriate for efficient charge extraction, owing to well energetic alignment with that of Pb-Sn mixed NBG perovskite. By comparing three HTLs in Figure 4.1(a-d), the bilayer approach yielded the most efficient device, with a champion PCE of 20.3%, J_{SC} of 32.2 mA cm^{-2}, V_{OC} of 0.82 V, and FF of 81.0%. The champion PEDOT−PSS-based device resulted in a PCE of 17.8%, J_{SC} of 30.6 mA cm^{-2}, V_{OC} of 0.81 V, and FF of 78.0%. The champion PTAA-only-based device showed an efficiency of 16.0%, a J_{SC} of 30.0 mA cm^{-2}, a V_{OC} of 0.79 V, and an FF of 69.9%. Each device was coated with a 70 nm-thick MgF_2 antireflective layer, optimized for minimal reflection losses. The role of anti-reflective coating thickness on device performance was further investigated, with data presented in Figure S1.4, demonstrating that a 0–100 nm thickness range maximizes J_{SC} by reducing reflection losses in narrow bandgap PSCs.

To elucidate the impact of different HTLs on device performance, we systematically analyzed key photovoltaic parameters in PSCs incorporating PEDOT: PSS, PTAA, and PTAA/PEDOT: PSS bilayers. The current-voltage (J-V) characteristics and short-circuit current J_{SC} metrics of these three configurations without anti-reflection coatings are shown in Figure S1.3, confirming the improved photocurrent extraction achieved with bilayer architectures. The bilayer HTL configuration exhibits significantly reduced hysteresis, with a hysteresis index of 0.01, compared to 0.08 for the PEDOT: PSS device and 0.03 for the PTAA-based device. These values, calculated from open-circuit voltage measurements, indicate that the higher hysteresis indices observed in the PEDOT: PSS and PTAA counterparts arise from unbalanced charge extraction and limited charge transport,[157] as illustrated in Figure 4.2a. PCE obtained from maximum power point tracking (MPPT) (Figure 4.2b) shows an initial rise in the PCE upon light soaking for PEDOT: PSS or PTAA-HTLs,

whereas the bilayer structure shows a stable PCE for 150 s. To further validate device performance, external quantum efficiency (EQE) measurements were performed on representative PSCs (Figure 4.2c). In an ideal case, EQE analysis provides a reliable cross-check of J_{SC} results and confirms balanced charge extraction. Quantitatively, the J_{SC} and EQE values are 29.4, 27.8, and 27.4 mA cm^{-2} for bilayer, PEDOT: PSS, and PTAA, respectively. These values agree with the J_{SC} measured from J-V curves, as EQE and J-V measurements were performed on devices with and without an antireflection coating, respectively, and show the same relative increase in current when replacing the single HTL with the double HTL. The higher EQE across the entire spectral range for devices with bilayer HTLs indicates improved charge collection compared to their individual HTL counterparts.

The origin of reduced recombination and, hence, the improved V_{OC} and FF can be understood by comparing the dark J-V curves in Figure 4.2d, which show a notable difference in leakage current among the three HTLs. The bilayer-HTL PSCs exhibited nearly 15 times lower leakage current than devices using PEDOT: PSS and PTAA as individual HTLs. For bilayer-based PSCs, the introduction of the PTAA interlayer improves perovskite film coverage and reduces pinhole formation, as confirmed by SEM surface images (Figure 4.4a-b). A lower leakage current in the case of bilayer HTL is attributed to complete HTL coverage over the ITO substrate, which prevents opposite charge carriers from the perovskite layer from recombining with the holes in the HTL, thereby contributing to higher V_{OC} and FF. Tabulated photovoltaic parameters of champion devices (Table S1.1) summarize the performance advantages of the bilayer HTL approach and correlate well with the optoelectronic insights from PL decay fitting.

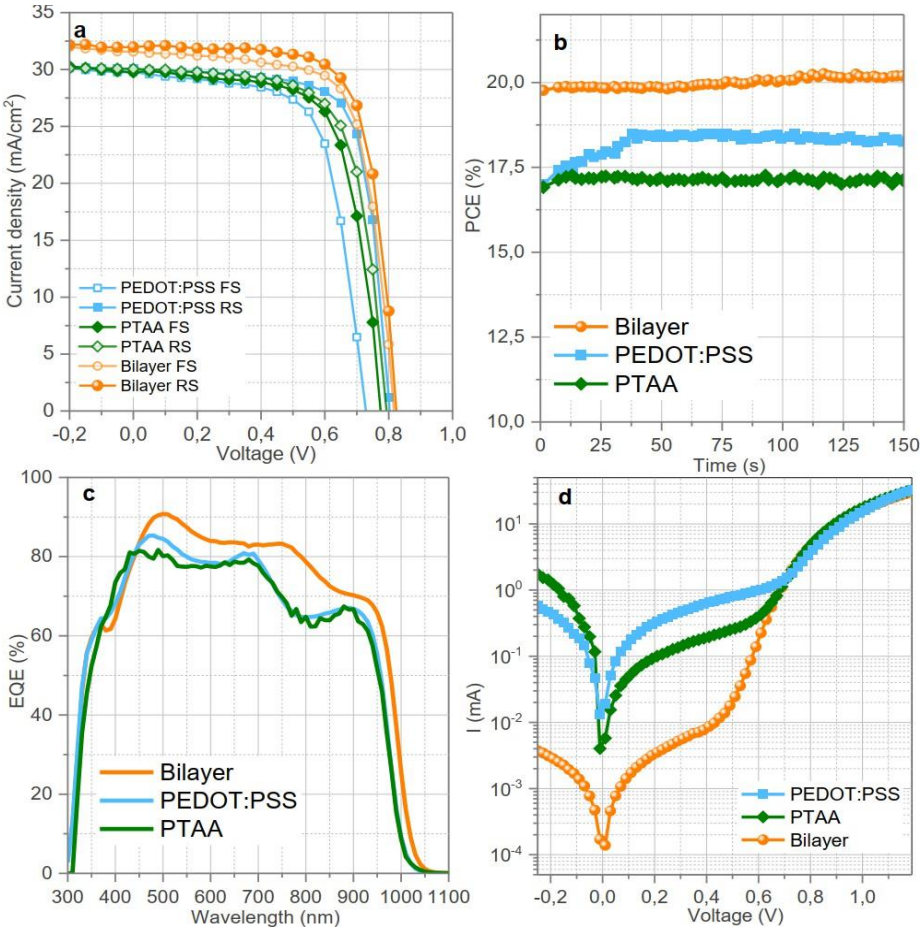

***Figure 4.2**: (a) Current−voltage curves, (b) maximum power point tracking, (c) external quantum efficiency, and (d) dark J-V curves of PSCs employing all three HTLs (with an anti-reflection coating (ARC, MgF_2,70 nm). Reproduced from reference[89] under CC-BY 4.0.*

Interface-driven photophysical phenomena

The photoluminescence quantum yield (PLQY) measurements suggest better interface quality in the bilayer-HTL/perovskite stack, with PLQY around 3-fold higher for bilayer HTL than for the other two HTLs (Figure 4.3a-b). This PLQY measurement also correlates to a higher quasi-Fermi level of splitting (QFLS), also referred to as implied V_{OC}.[158] We further recorded the rise and drop in the V_{OC} of the PSCs at 1-sun conditions employing three HTLs (Figure 4.3c). While the PEDOT: PSS- and PTAA-based HTLs show a slow rise in the V_{OC} over several seconds, this may be due to capacitive effects in the device.[159] The bilayer HTL-based PSC quickly reaches its maximum V_{OC}. In an ideal case, the

device should reach its maximum V_{OC} and show no temporal dependence on light soaking, a trend clearly more pronounced in the bilayer HTL PSCs, hinting at improved interfacial properties with Sn–Pb perovskite.

To confirm the improvement in the bilayer HTL PSCs, we recorded their electroluminescence (EL) spectra. Figure 4.3d and e show EL spectra and EL yields as a function of injection current densities for all three PSCs. The EL measurements at a given current density exclude resistive effects that might be present in the devices due to different energy-level alignments or differences in charge-transport characteristics of the HTLs.[160] The EL spectra at a given current density of 50 mA cm^{-2} show the highest EL for bilayer HTL, followed by PTAA and PEDOT: PSS. This spectrum provides direct confirmation of enhanced radiative recombination in bilayer HTL-based PSCs, arising from improved interfacial properties at the HTL/NBG perovskite interface. The trends in the EL intensity validate the V_{OC} values in the cells. It further suggests a higher EL in the low injection current density, indicative of a significantly lower trap density in these films.[161] In general, PTAA-based HTLs show a saturation of the EL intensity at an elevated injection current density. In contrast, the EL of the PEDOT: PSS-based film shows a drop.

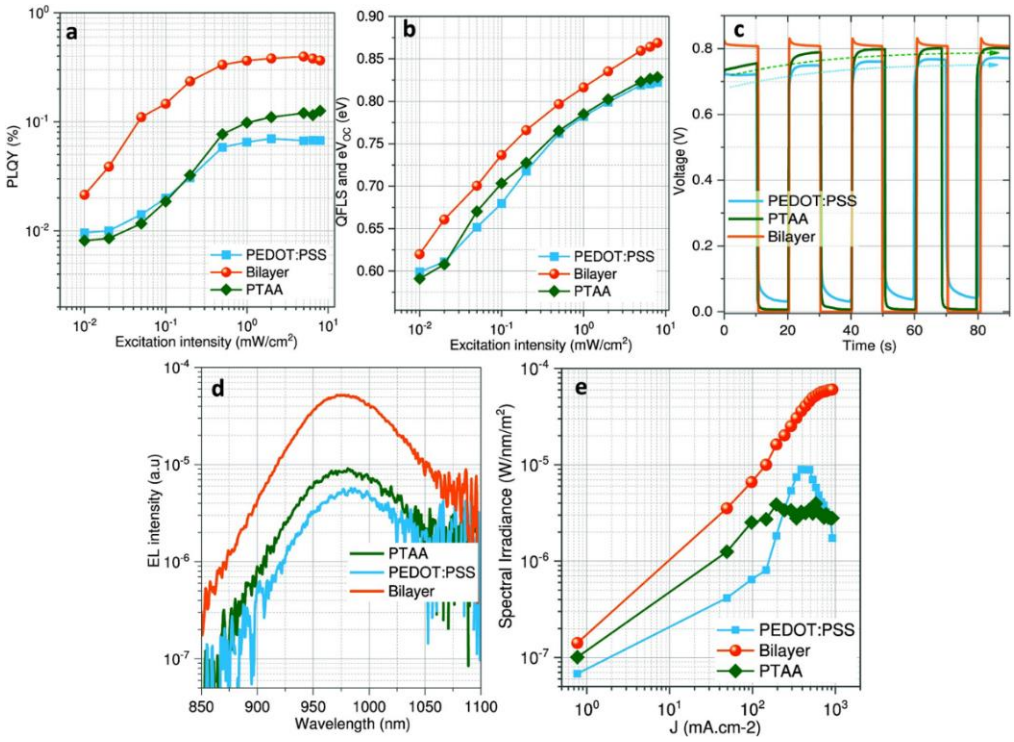

***Figure 4.3**: (a) and (b) show the photoluminescence (PL) quantum yield and QFLS of perovskite films deposited atop three different HTLs. (c) shows the rise and decay of the V_{OC} of the PSCs employing the three HTLs, measured at 1-sun conditions. (d) EL curves of three representative PSCs at an injection current density of 50 mA/cm^2, measured in air. (e) EL intensity as a function of injected current density for all three PSCs and reproduced from reference[89] under CC-BY 4.0.*

Figure 4.4(a-c) confirms the formation of a compact, pinhole-free perovskite film, a crucial prerequisite for achieving high device performance. To assess surface morphology and film uniformity, atomic force microscopy (AFM) measurements were performed, as shown in Figure S1.5. The results reveal that variations in HTL deposition directly influence the topography of the overlying perovskite films. Notably, the bilayer-based perovskite exhibited the lowest surface roughness, with a root mean square (RMS) value of 37.68 nm, compared to 68.32 nm for PEDOT: PSS-based and 44.36 nm for PTAA-based perovskite films.

The higher quality of perovskite films on PTAA HTLs is confirmed by time-resolved PL (TRPL) transients (Figure S1.6a,b). The PTAA-only HTL shows the

highest carrier lifetime, followed by the bilayer HTL. We attribute the lower PCE of PTAA-based devices, despite their longer carrier lifetimes, to poor charge extraction, likely due to low conductivity. On the other hand, the rapid PL decay of the films grown on PEDOT: PSS, combined with the lower efficiency of the PEDOT: PSS-based devices, hints at increased interfacial trapping.[162]

To assess whether different HTLs affect ambient/photostability, we monitored temporal PL in air under continuous laser irradiation for several minutes. TRPL did not show any notable changes in the bilayer, followed by PTAA, whereas the PEDOT: PSS HTL-based perovskite film showed the most pronounced changes (Figure 4.4(d-f)). This higher initial drop in PL intensity for the PEDOT: PSS HTL might be due to increased trapping at the PEDOT: PSS/perovskite interface, leading to a shorter TRPL lifetime. Generally, the performance of perovskite-based devices is attributed to their longer carrier lifetimes, and often, superior-quality films are coupled with slower PL decays.[163] TRPL lifetime for PTAA-only based perovskite films revealed a slow PL decay for the initial measurements, followed by a reasonable drop after 6 min of photoirradiation, hinting that the continuous light exposure leads to the creation of defect states. The bilayer HTL-based perovskite films exhibit consistent TRPL under continuous laser irradiation, even after prolonged exposure, suggesting a high-quality bilayer/perovskite interface. These results are also consistent with the PLQY and EL findings and are complemented by the device performance.

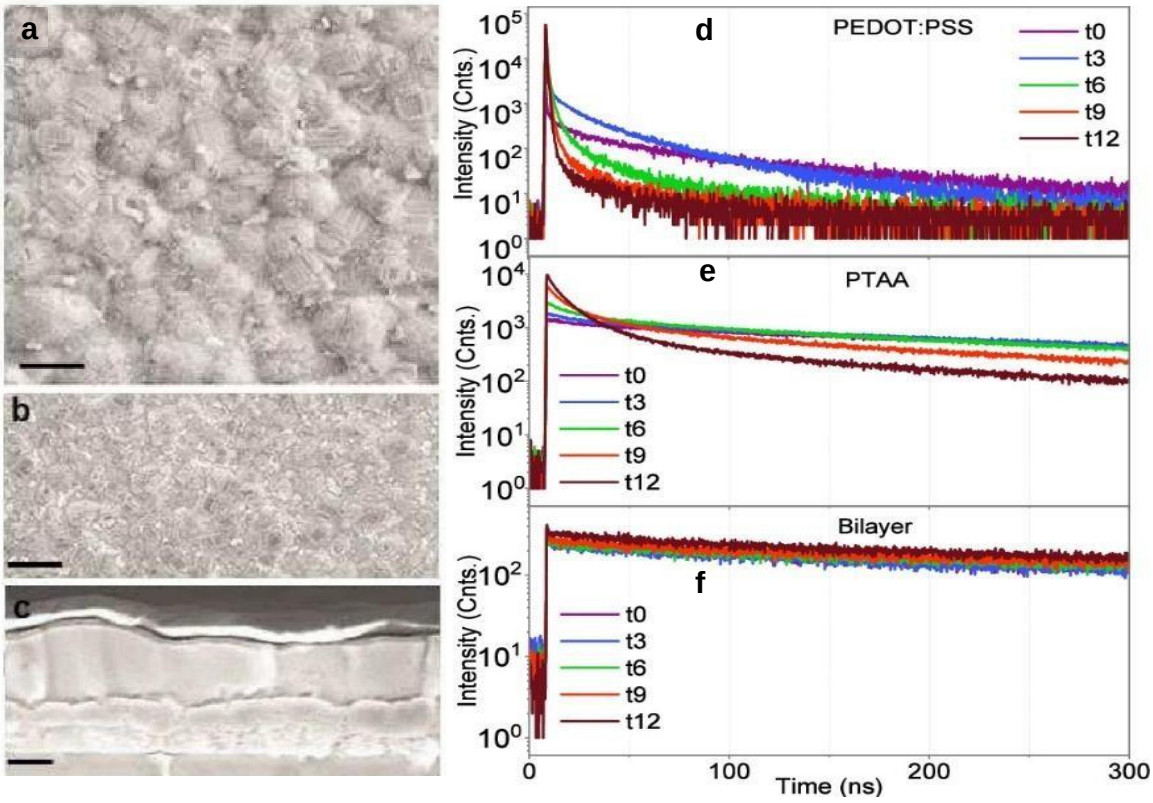

***Figure 4.4**: (a, b) Surface morphology of the perovskite deposited atop bilayer HTL (scale bars 1 µm and 400 nm, respectively). (c) Cross-sectional SEM image of complete PSC stack (scale bar 200 nm). PL transients of the ITO/HTLs/perovskite (d) PEDOT: PSS, (e) PTAA only, and (f) Bilayer, excited from the glass side, measured in air under continuous laser irradiation (pulsed laser, λexc 450 nm, repetition rate 200 kHz). The PL transients were measured every 3 min (t0... t12) and reproduced from reference[89] under CC-BY 4.0.*

5 IMPACT OF NARROW BANDGAP CELLS ON ALL-PEROVSKITE TANDEM ARCHITECTURES

In this chapter, the emphasis is on the application of optimized mixed lead–tin (Pb–Sn) perovskite absorbers, introduced in Chapter 4, for all-perovskite tandem solar cells. The Pb–Sn perovskite, with a bandgap of approximately 1.25 eV, functions as the bottom cell, while a wide-bandgap perovskite with a bandgap of about 1.7 eV serves as the top cell. This tandem configuration is investigated to assess its impact on the open-circuit voltage (V_{OC}) and the overall power conversion efficiency. Building on the previous chapter, this section highlights the importance of bandgap engineering and tandem architectures in advancing the performance of perovskite solar cells. The results presented here are based on work published in ACS Materials Letters, distributed under the CC-BY 4.0 license.

5.1 Introduction to Improved Pb-Sn Mixed Perovskite Solar Cells

Building on the detailed understanding of voltage-loss mechanisms and effective mitigation strategies explained in the previous chapter (Chapter 4), this section focuses on the practical application of these advancements in optimized Pb–Sn mixed PSCs as the foundational subcells in all-perovskite tandem solar architectures. The significant V_{OC} improvements achieved through interface engineering and the implementation of optimized hole-transport layers, such as the bilayer PEDOT: PSS/PTAA configuration, have fundamentally enhanced the photophysical properties and device stability of narrow-bandgap Pb–Sn PSCs. These optimized NBG cells, characterized by reduced non-radiative recombination and superior charge extraction, serve as critical building blocks for tandem devices aimed at overcoming the single-junction performance ceiling and pushing toward higher power conversion efficiencies. Integrating such finely tuned Pb–Sn perovskite absorbers into tandem architectures alongside

complementary wide-bandgap subcells offers a promising pathway to maximize spectral utilization, improve current-voltage matching, and ultimately achieve superior tandem device performance. This chapter thus explores the design, fabrication, and performance implications of incorporating these optimized NBG cells into all-perovskite tandem solar cells, establishing a direct link to fundamental V_{OC} loss mitigation.

5.2 Effect of Narrow Bandgap Perovskite as A Bottom Cell in All-Perovskite Tandem Solar Cells

The schematic structure of all-perovskite tandem solar cells (Figure 5.1a) shows the monolithic integration of WBG and NBG perovskite subcells, separated by a recombination layer that enables efficient charge-carrier recombination and transport between cells. This architecture typically uses a two-terminal configuration, with subcells connected in series, enabling simplified device fabrication and potentially higher voltage outputs than single-junction cells. The gains made in the single-junction NBG cells are applied to fabricate an all-perovskite tandem solar cell (TSCs) that also involves a separately optimized WBG perovskite (Eg =~1.70 eV, $Cs_{0.3}FA_{0.6}MA_{0.1}Pb(I_{0.7}Br_{0.3})_3$) as the top cell and the optimized NBG perovskite (Eg = 1.21 eV) as the bottom cell. Both the WBG and the NBG perovskite layers were processed in a N_2-filled glovebox (except for PEDOT: PSS as the HTL, the recombination layer, and atomic layer deposition of SnOx). The configuration of all perovskite TSCs shown in Figure 5.1a is as follows: ITO/SAMs/WBG/C_{60}/ALD-SnOx/Au/bilayer(PEDOT:PSS/PTAA)/NBG/C_{60}/BCP/ Ag.

In Figure 5.1b, the light J–V characteristics show performance differences among the standalone WBG and NBG devices and the tandem configuration. The tandem solar cell exhibits a higher V_{OC} than either single junction due to the additive voltages of the two subcells, alongside improved current densities and fill factors resulting from optimized layer interfaces and balanced charge extraction. This enhancement reflects the efficient spectral utilization in the tandem device,

with the WBG layer absorbing high-energy photons while allowing lower-energy photons to pass to the NBG subcell, effectively reducing thermalization losses. Thus, the tandem cell leverages complementary absorption profiles to surpass the Shockley-Queisser limit of single-junction devices, thereby advancing photovoltaic efficiency. These results underscore the importance of precise layer engineering, energy band alignment, and interface optimization to maximize the electrical output of all-perovskite tandem architectures and highlight the potential of these devices for next-generation solar energy conversion. The *J-V* curves of the best-performing bilayer-based NBG bottom cell and all-perovskite TSCs with a minimal hysteresis, demonstrating a PCE of 20.3% and 25.1%, V_{OC} of 0.82 and 2.00 V, J_{SC} of 32.3 mA cm^{-2} and 15.9 mA cm^{-2}, and FF of 81.0% and 81.2%, respectively. The high PCE of tandem devices, with a remarkable V_{OC} of 2.00 V, is achieved by using the bilayer HTL discussed in the previous sections for the NBG bottom cell (Figure 4.2a), which, as we have seen, enhances photovoltaic (PV) parameters. Additionally, this value is enabled by the optimization of the WBG top cell, where the gas-quenching method was used to promote perovskite formation.

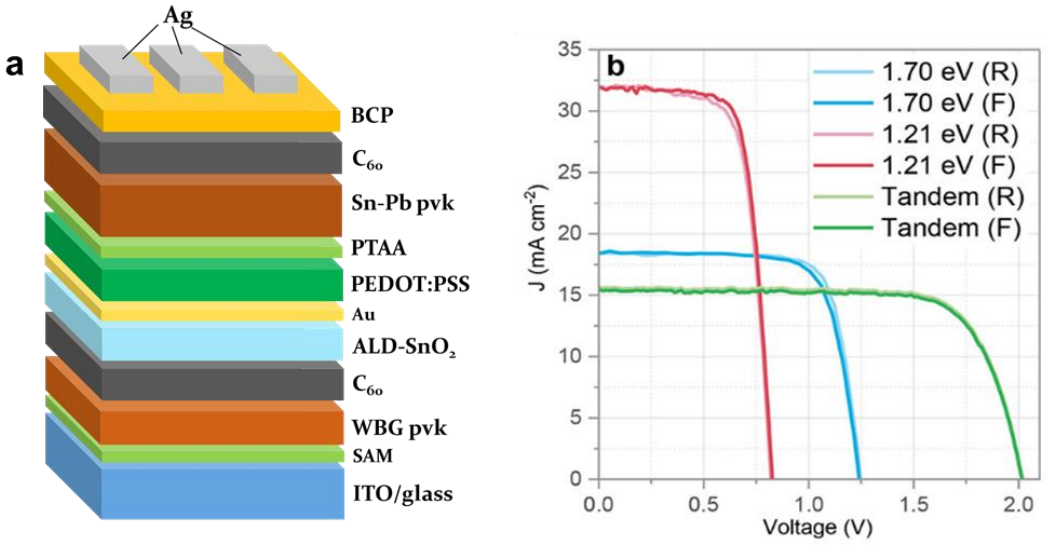

***Figure 5.1**: Schematic structure of all-perovskite tandem solar cells (a) and comparison of light J–V characteristics for narrow-bandgap, wide-bandgap, and tandem configurations (b). Reproduced from reference[89] under CC-BY 4.0.*

The cross-sectional SEM image presented in Figure 5.2a provides a clear visualization of the whole device stack in the all-perovskite tandem solar cell architecture. The image confirms the successful formation of uniform, well-defined layers, including the individual wide-bandgap (top) and narrow-bandgap (bottom) perovskite sub-cells, as well as the recombination layer that enables efficient charge transfer between sub-cells. The precise thickness and integrity of each layer are crucial for minimizing series resistance and facilitating optimal charge extraction, both of which are essential to achieving high device efficiency. The clear separation and good adhesion between layers in the SEM image also indicate practical processing and interface engineering, which are key to device reproducibility. The improved photovoltaic performance of the tandem devices can be closely attributed to the fabrication of crack-free, compact, and high-quality perovskite absorber layers for both the WBG and NBG subcells, as clearly demonstrated in the cross-sectional SEM image of the all-perovskite tandem solar cells. To achieve optimal current matching and reduce J_{SC} mismatch between the top and bottom subcells, the thicknesses of the WBG and NBG absorber layers were carefully optimized to approximately 400 nm and 700 nm, respectively.

In Figure 5.2b, the external quantum efficiency (EQE) spectra of the tandem cell are shown, enabling detailed evaluation of the spectral response and the current generation by each sub-cell. The distinct EQE features of the wide-bandgap and narrow-bandgap absorbers demonstrate that both sub-cells contribute efficiently to the overall photocurrent across a broad wavelength range. The summation of the two sub-cell contributions matches well with the integrated current density, verifying effective current matching—a vital requirement for maximizing tandem device performance. The non-overlapping spectral regions and the high EQE values for each sub-cell highlight the efficiency of bandgap tuning and the success of optimizing individual layers. This spectral separation also minimizes parasitic absorption and recombination losses.

The EQE spectra of the tandem device show distinct contributions from both the top WBG and bottom NBG subcells, while the summed EQE confirms their combined photocurrent. The integrated current densities derived from the EQE curves are 17.8 and 14.1 mA/cm² for the WBG and NBG subcells, respectively, which are in excellent agreement with the mean J_{SC} values obtained from the J–V characterization. This agreement provides strong evidence that the tandem device performance is primarily limited by the NBG subcell, highlighting the critical role of precise thickness control and material quality in tandem architectures. Consequently, these results confirm that the enhanced tandem efficiency arises from a combination of optimized absorber thickness and high-quality perovskite films, which enable effective current matching between the WBG and NBG subcells.

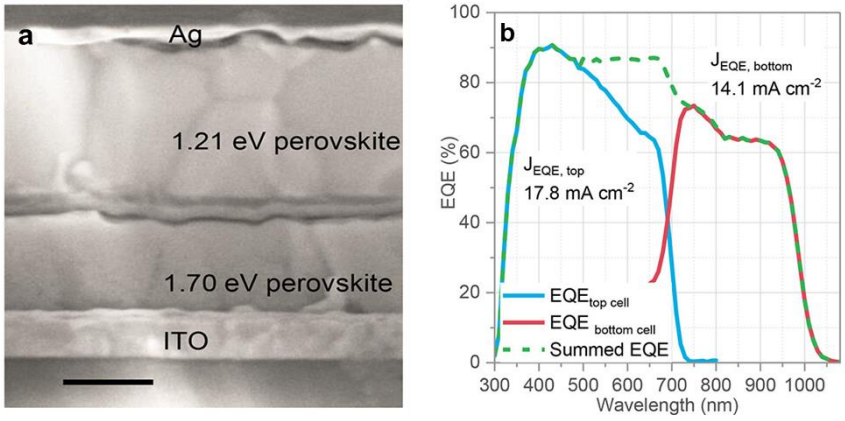

***Figure 5.2**: Cross-sectional SEM image showing the full device stack of the all-perovskite tandem architecture (a) and external quantum efficiency (EQE) spectra of the tandem cell, illustrating the spectral contributions of each sub-cell (b). Reproduced from reference[89] under CC-BY 4.0.*

Figure 5.3 presents a statistical overview of key photovoltaic parameters—short-circuit current density, power conversion efficiency, open-circuit voltage, and fill factor for all-perovskite tandem solar cells, based on measurements from multiple devices. The performance metrics of 28 all-perovskite tandem solar cells (TSCs) reveal key insights into device reproducibility and optimization. The Jsc

distribution, with a mean of 14.47 mA/cm² and a box range of 13.78-14.87 mA/cm², reflects the sensitivity of tandem architectures to current matching between sub-cells. In particular, the narrow bandgap bottom cell—typically based on Sn–Pb perovskites—plays a critical role in harvesting near-infrared photons, and any deviation in its thickness or bandgap tuning can significantly impact the overall current output.

Similarly, the V_{OC} distribution, with a mean of 1947 mV and a box range of 1913-1978 mV, highlights the effectiveness of interfacial engineering in suppressing non-radiative recombination.

The FF distribution, with a mean of 75.5% and a box range spanning from 74.6% to 77.92%, reflects the influence of series resistance and charge extraction efficiency. Devices with suboptimal contact interfaces or interlayer morphology tend to exhibit lower FF, underscoring the importance of precise layer deposition and interface passivation.

Finally, the PCE distribution, with a mean of 22.1% and a box range of 21.29-23.02%, captures the combined influence of V_{OC}, J_{SC}, and FF optimization. The spread in efficiency values reflects device-to-device variability in optical alignment, interfacial quality, and sub-cell balancing, emphasizing the need for scalable fabrication protocols with tight process control.

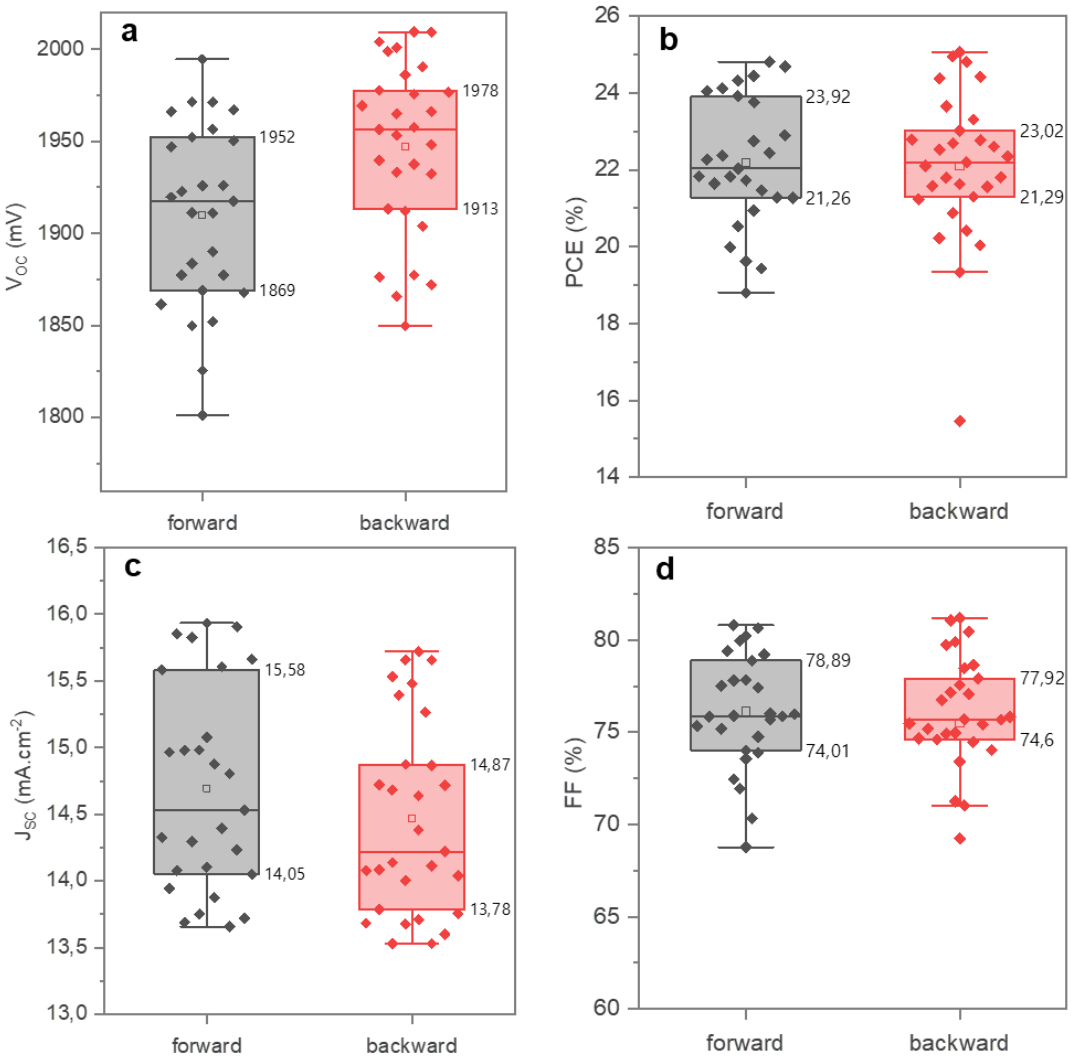

***Figure 5.3**: Statistical analysis of key photovoltaic parameters for all-perovskite tandem solar cells: short-circuit current density (J_{SC}) (a), power conversion efficiency (PCE) (b), open-circuit voltage (V_{OC}) (c), and fill factor (FF) (d). Each box plot displays the mean, maximum, and minimum values obtained from all measured devices, reproduced from reference[89] under CC-BY 4.0*

6 GAS-QUENCHING MEDIATED CRYSTALLIZATION OF LEAD-TIN PEROVSKITES

This chapter focuses on using gas quenching as an alternative to the traditional antisolvent quenching method for fabricating mixed lead–tin (Pb–Sn) perovskite solar cells. Gas quenching enables slower crystallization, resulting in smoother perovskite films and improved device efficiency. The study further investigates the influence of optimal gas pressure on photovoltaic performance, highlighting its role in achieving efficient Pb–Sn mixed perovskite solar cells.

The results presented in this chapter are based on the article "Gas Quenching Mediated Crystallization for Optoelectronic-Grade Pb–Sn Perovskite Films", published in Solar RRL,2025. I served as the primary author of this work, carried out in collaboration with Maria Azhar, Muhammad Irfan Haider, Yenal Yalcinkaya, and others. My contributions included conceptualizing the project, fabricating and evaluating thin films and perovskite solar cell (PSC) devices, and characterizing thin films using PLQY, AFM, and SEM. I also conducted the data analysis and wrote the original manuscript. The co-authors also provided valuable support in conceptualization, characterization, data analysis, and interpretation. In addition, they carried out the review and actively participated in its revision, ensuring the quality and

6.1 Quenching Mechanisms in Lead-Tin Mixed Perovskite Film Formation

Single-junction PSCs with higher efficiencies commonly utilize lead-based perovskite materials.[164,165,166] However, despite their superior PCEs, PSCs face significant challenges, particularly concerning lead toxicity.[167,168]

On the other hand, pure tin-based PSCs seem to overcome toxicity issues; however, their Sn^{2+} ions exhibit high reactivity and are prone to oxidation to Sn^{4+}, which severely compromises device stability. Additionally, pure tin-based perovskites tend to form defect-rich films with poor morphology and stability due

to their high Lewis acidity and low activation energy, often leading to uncontrolled nucleation, increased vacancy defects, and inferior film quality.[169,170,171]

An alternative to lead-based PSCs is lead-tin (Pb–Sn) mixed perovskites, which offer the advantage of reduced toxicity compared to pure lead-based perovskites.[172] They also mitigate stability issues caused by the oxidation of Sn^{2+} to Sn^{4+}, which are more pronounced in pure Sn-based perovskites.[173,174] Additionally, Pb–Sn mixed perovskites exhibit a narrower bandgap (NBG) of approximately 1.1–1.3 eV; this narrowing is attributed to the bandgap bending effect relative to their pure counterparts.[175,176,177] Despite these significant advantages, Pb–Sn mixed NBG PSCs face persistent challenges, such as reproducibility issues.[178,179] These problems stem from faster crystallization, higher defect density, and sensitivity to moisture and oxygen.[180] The crystallization behavior of Sn–Pb mixed perovskite films is crucial for device performance. To understand this issue, it is essential to consider the underlying chemistry. Lanthanide contraction, which results in smaller atomic radii, typically leads to slower oxidation. Tin (Sn) does not experience lanthanide contraction, making it more prone to oxidation and consequently accelerating the crystallization of Sn-containing perovskite films.[181]

To address the rapid crystallization issue, various strategies have been explored. Among them, gas quenching has emerged as a powerful technique for regulating film-forming dynamics, offering an alternative to conventional antisolvent dripping. As illustrated in Figure 6.1, the device fabrication process involves sequential deposition of the perovskite layer, followed by thermal evaporation of the top electrodes, with particular emphasis on the roles of the antisolvent and gas-quenching steps in modulating crystallization kinetics, (Full-stack device shown in Figure 6.2). In addition, for example, Yang et al. demonstrated that the desorption barrier of dimethyl sulfoxide (DMSO) is significantly higher for Sn-based complexes than for Pb-based ones, leading to asynchronous

crystallization. By tailoring the solvent composition, particularly the DMSO content, they achieved synchronized Sn–Pb crystallization and homogeneous film formation.[182] In another study, Cheng Li et al. introduced N-hydroxythiophene-2-carboximidamide (NHC), a multifunctional additive, to control crystallization in tin-based PSCs.[183] Omar E. Solis et al. investigated the incorporation of thiophene-2-ethylammonium halides (TEAX) as additives in tin-based perovskite formulations, significantly enhancing film quality by effectively reducing Sn^{4+} formation and modulating crystallization dynamics.[184] Moreover, iso-pentylammonium tetrafluoroborate ([PNA]BF_4) was employed to selectively anchor Pb^{2+} ions, effectively modulating the crystallization process and resulting in a uniform distribution of Sn and Pb within the perovskite film.[185] While additives can control crystallization, they may also destabilize the crystal structure and cause bandgap fluctuations. Therefore, a mechanistic approach is necessary to control the crystallization rate in Sn-Pb-based perovskites precisely.

In this thesis, to address those issues in Pb-Sn NBG PSCs, the gas quenching (GQ) method, rather than the traditional antisolvent (AS) technique, proved to be a productive approach. GQ has emerged as a more environmentally friendly quenching process.[186,187] Moreover, it eliminates the need for harmful chemicals, offers higher repeatability, and is industrially viable. The GQ method works by gradually drying the perovskite material by exposing it to an inert gas, such as nitrogen.[188,189,190] This controlled crystallization of perovskite films is crucial for producing high-quality films with fewer defects.[191,192] Although researchers have demonstrated the applicability of gas quenching for perovskite film formation already, a detailed in-situ transmission measurement to directly track the rate of crystallization and its effect on grain sizes and how that contributes to the overall performance of devices is still required. Our work resulted in significant improvements in device performance, with the PCE increasing from 18.3% for AS-processed devices to 19.1% for GQ-processed devices. Additionally, GQ enhances device repeatability by providing a wider parameter window for

processing. We carefully investigated and compared AS- and GQ-processed films and devices using photoluminescence quantum yield (PLQY) measurements, atomic force microscopy (AFM), and grain size analysis. Furthermore, in-situ transmittance measurements were used to analyze the effect of GQ on the rate of crystallization, grain sizes, and ultimately the overall device performance.

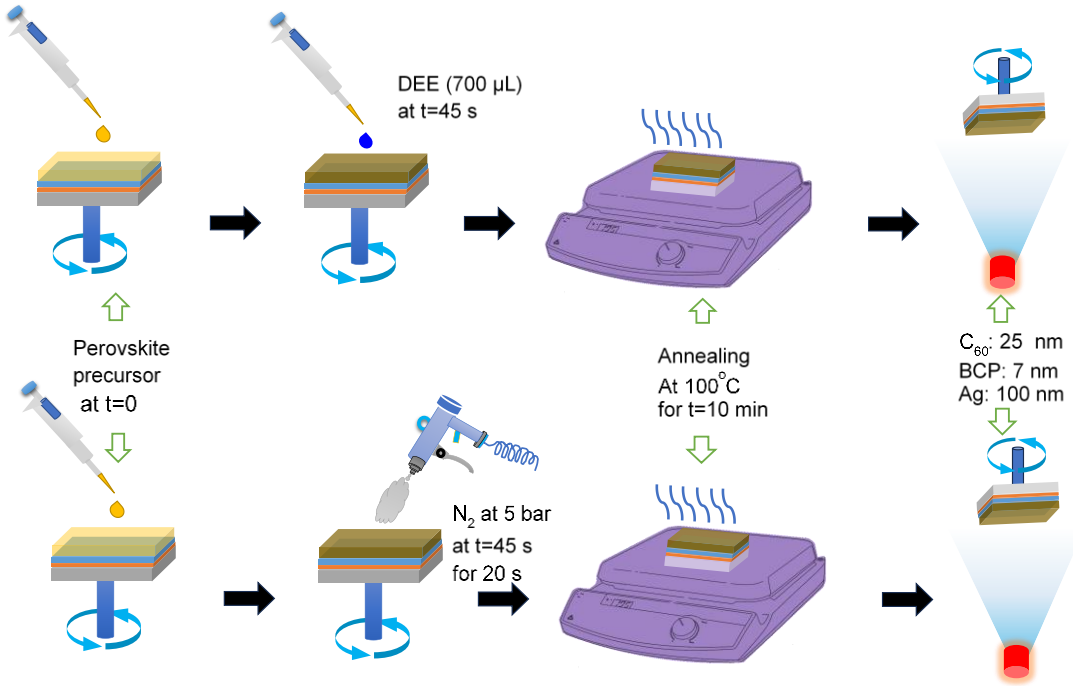

***Figure 6.1**: Schematic representation of device fabrication, illustrating the process from perovskite layer deposition to thermal evaporation of precursors, with emphasis on antisolvent and gas quenching techniques. Reproduced from reference.*[193]

Gas quenching operates by rapidly displacing solvent vapor with an inert or dry gas stream—typically nitrogen thereby inducing supersaturation and promoting uniform nucleation across the substrate. This method enables precise control over solvent evaporation rates and suppresses undesirable phase segregation or wrinkling, which are common in Sn-rich perovskite systems.[135] Recent studies have demonstrated that gas quenching not only improves film coverage and grain uniformity but also enhances optoelectronic properties by reducing trap

density and facilitating vertical charge transport.[194] For instance, modeling frameworks developed by Wang et al. provide quantitative insights into the interplay between gas flow dynamics, solvent removal, and nucleation behavior, offering a mechanistic basis for optimizing quenching protocols.[195]

The reproducibility of gas quenching makes it particularly attractive for the fabrication of low-bandgap sub-cells. Understanding the underlying mechanisms, such as solvent–gas interactions, nucleation thresholds, and nitrogen gas compatibility, is essential for tailoring film formation to achieve high-performance devices. This chapter explores the mechanistic aspects of gas quenching in Pb–Sn mixed perovskites, drawing on recent experimental and theoretical advances to elucidate its role in shaping film morphology, phase purity, and device efficiency.

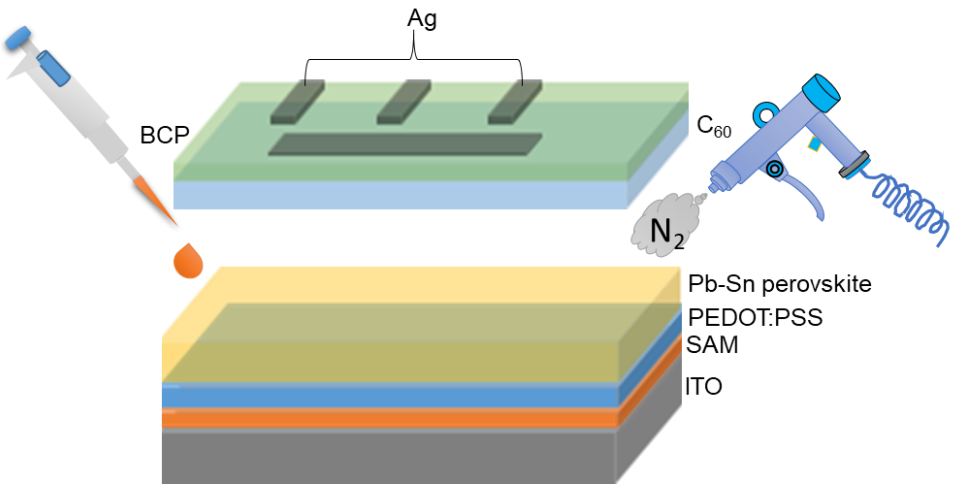

***Figure 6.2**: Schematic of the full-stack Pb-Sn mixed perovskite solar cell architecture, illustrating the layered configuration from substrate to top electrode (ITO/SAM/ PEDOT: PSS/perovskite/C_{60}/BCP/Ag using both anti-solvent and gas quenching methods.*

6.2 Impacts of Gas Quenching Method on Pb–Sn Mixed PSCs and Film Quality

Hereafter, AS films/devices refer to those in which perovskite quenching was

performed using the AS method, whereas GQ films/devices refer to those in which perovskite quenching was performed using the GQ method. Figure 6.3 presents a box plot of the photovoltaic performance of AS and GQ devices, showing open-circuit voltage (V_{OC}), short-circuit current density (J_{SC}), fill factor (FF), and overall power conversion efficiency (PCE). The GQ devices exhibit higher V_{OC}, suggesting reduced defect density, as supported by their higher PLQY values (see Figure 6.6). The FF results appear comparable; however, notably, the data for all parameters–including FF, J_{SC}, V_{OC}, and overall PCE are consistent, showing only slight deviations from the average values for GQ devices. The reproducibility of the GQ method is further demonstrated by the narrow distribution of all photovoltaic parameters in the box plot, which also indicates relatively higher average values for each parameter, highlighting the superior performance of the GQ method.

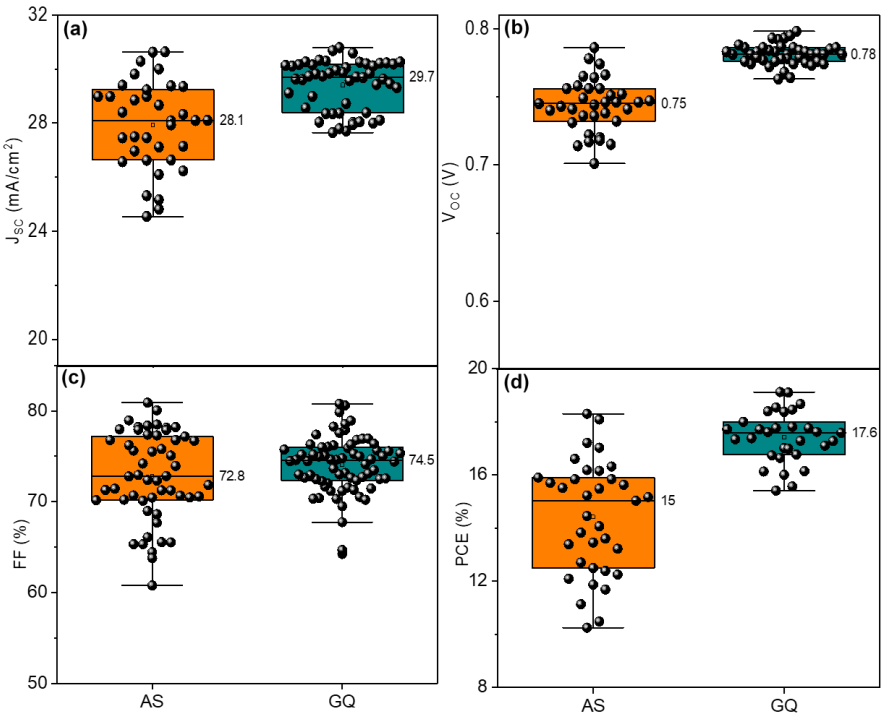

***Figure 6.3**: Boxplots of the photovoltaic parameters of Pb-Sn mixed perovskite solar cells fabricated using AS (left, orange) and GQ (right, green) at a gas pressure of 5 bar. The parameters shown are current density (J_{SC}), open circuit voltage (V_{OC}), fill factor (FF), and power conversion efficiency (PCE) in panels (a-d), respectively. Reproduced from reference.[193]*

As a result, the gas-quenched device exhibits a higher V_{OC} of 0.79 V, resulting in a PCE of 19.1%. In comparison, the AS-treated counterpart shows a lower V_{OC} of 0.77 V, resulting in a reduced PCE of 18.3%. A comprehensive comparison of the photovoltaic parameters for PSCs processed via both AS and GQ methods is presented in Table S2.1. This table summarizes the average and champion values for key device metrics, enabling a precise evaluation of the impact of each processing technique on device performance.

To further investigate the reasons behind the differing performance of AS and GQ devices, V_{OC} rise and decay measurements were conducted under varying illumination conditions (light on/off) at intervals ranging from 0 to 70 seconds, in 10-second increments. Figure 6.4a compares the V_{OC} rise and decay behavior of PSCs prepared using the AS and GQ methods. The V_{OC} response differs notably between the two methods, particularly in the speed of rise upon illumination and the rate of decay after the light is turned off. The GQ devices exhibit a more pronounced and rapid increase in V_{OC}, reaching a maximum of 0.80 V shortly after illumination begins. In contrast, the AS devices show a slower V_{OC} rise, reaching only 0.77 V. During the decay phase, the GQ cells display a sharper decline, with the voltage dropping to 0 V, indicating rapid carrier recombination and minimal trap-assisted retention. Conversely, AS-treated films demonstrate a slower V_{OC} decay, with residual voltage persisting after illumination ceases.

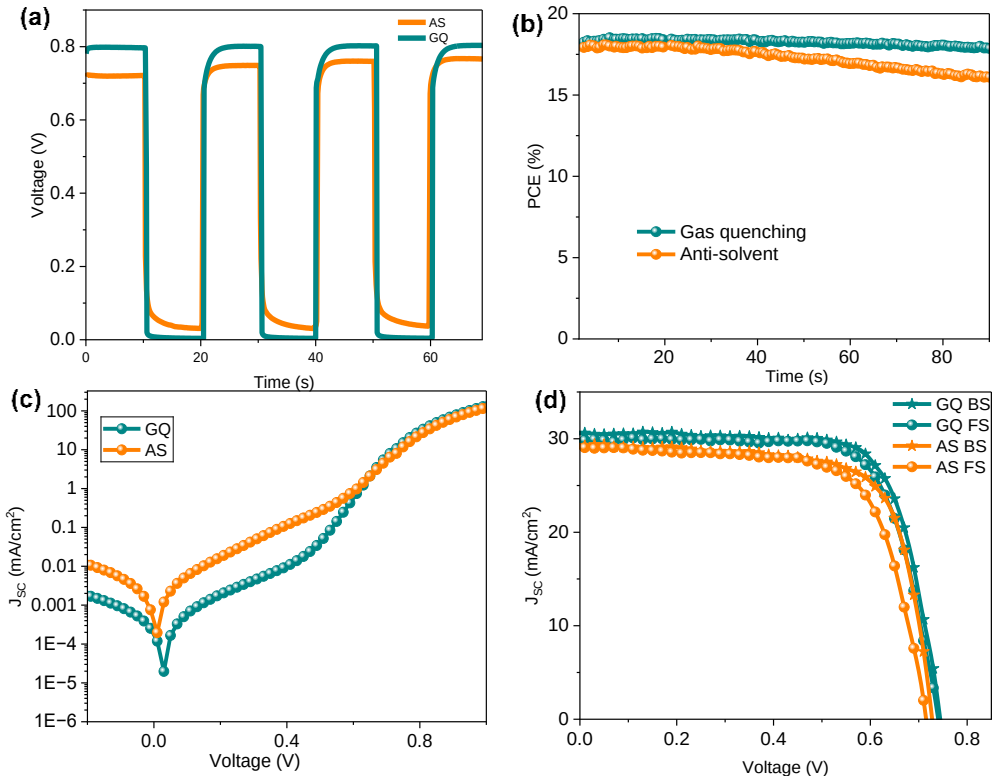

***Figure 6.4**: V_{OC} decay and rise measurements of the best-performing cells in both scenarios (a), MPP tracking of perovskite solar cells for 90 seconds following the initial measurement inside the glovebox (b), dark (c) and light (d) J–V curves of devices fabricated via GQ and AS methods under forward (FS) and backward (BS) scans. Reproduced from reference.**[193]

The maximum power point (MPP) tracking measurements shown in Figure 6.4b were conducted inside a nitrogen-filled glovebox without encapsulation, under continuous illumination for 90 seconds. Devices fabricated via antisolvent quenching exhibit a faster drop in power output than those processed by gas quenching, which can be attributed to inherent instabilities that occur even in an inert glovebox environment, such as residual solvent effects, incomplete crystallization, or interfacial defects formed during processing.[196]

Moreover, the GQ device exhibits a significantly lower dark current compared to the AS devices, with a current density of 1.98×10^{-5} mA/cm² at 0.0 V, indicating reduced leakage. In contrast, the AS device shows a higher dark current density of 1.96×10^{-4} mA/cm² as illustrated in Figure 6.4c. These results confirm that

controlled crystallization via the GQ method leads to improved diode quality and reduced non-radiative losses in the device. In Figure 6.4d, the light J-V curves for both GQ and antisolvent AS devices were measured in both forward (0 V to V_{OC}) and backward (V_{OC} to 0 V) scan directions to assess hysteresis. For the GQ device, the forward and backward scans nearly perfectly overlap, indicating minimal hysteresis, with a hysteresis index of 0.0021, compared to 0.0182 for the AS device; both values were calculated from current density measurements. This minimal hysteresis suggests that the GQ film has efficient charge transport and reduced ion migration, all of which contribute to repeatable, improved, and more stable device performance.[197,198] To confirm that the improved performance is indeed correlated with enhanced film quality, we performed additional measurements.

Repeatability of gas-quenched devices

As discussed earlier and shown in Figure 6.5, GQ devices exhibit higher repeatability than AS devices. The GQ devices exhibit a narrower distribution of solar cell efficiencies, ranging from 15.4% to 19.1% (Δ = 3.7%), whereas the AS method produces a comparatively wider range, from 10.3% to 18.3% (Δ = 8.0%). This 4.3% reduction in spread indicates that the GQ method yields devices that are more consistent and repeatable. This confirmation suggests that GQ is less sensitive to exact processing parameters. As reported by Samantha C. Kaczaral et al., the repeatability of perovskite film formation appears to be enhanced with the GQ method, potentially due to slower, more controlled crystallization dynamics.[199] The timing of perovskite film formation is crucial to ensure that the final film is of high quality and reproducible. As shown in Figure 6.7a, in-situ spectral measurements reveal that the AS method induces rapid nucleation, resulting in a narrower processing window, increased sensitivity to timing variations, and, consequently, reduced repeatability. In contrast, as shown in Figure 6.7b, the GQ method slows and regulates the crystallization process, leading to more uniform spectral evolution and improved reproducibility across

devices. This is confirmed by the performance parameters shown in Figure 6.3, where GQ devices exhibit a higher mean PCE of 17.6% with a standard deviation of 0.9%, compared to AS devices, which show a lower mean efficiency of 15% and a higher standard deviation of 2.1%.

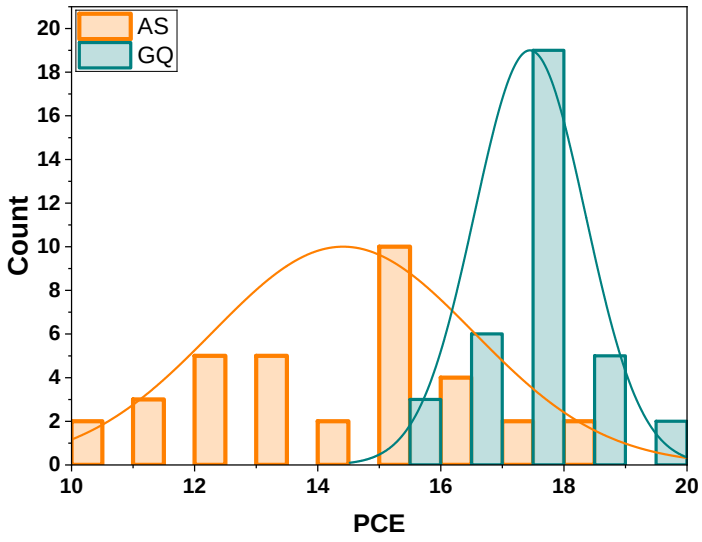

***Figure 6.5**: A comparative statistical distribution of PCE for AS and GQ devices, presenting the mean values and standard deviations to illustrate the consistency and variability of performance across samples. Reproduced from reference.*[193]

Lead-Tin mixed perovskite film analysis

An essential tool for assessing perovskite film quality is the photoluminescence quantum yield (PLQY). Therefore, we conducted a comparative analysis of PLQY and quasi-Fermi level splitting (QFLS) for perovskite films deposited on ITO/SAM/PEDOT: PSS substrates using the AS and GQ methods. This analysis provided valuable insights into film quality and recombination losses in the solar cells. PLQY measurements were performed under varying illumination intensities, ranging from 0.1 to 1 sun in increments of 0.2 sun. The GQ films exhibited a higher PLQY value of 0.28%, with an average of 0.19%, compared to 0.21% and an average of 0.12% for the AS films, as shown in Figure 6.6a. This indicates more efficient radiative recombination and reduced non-radiative losses

in the GQ-processed films. Similarly, Figure 6.6b shows the QFLS values, where the GQ films exhibit a higher QFLS of 0.85 V compared to 0.81 V for the AS films. A higher QFLS suggests that the GQ method produces better-quality perovskite films with fewer defect states, thereby lowering the QFLS. Moreover, since QFLS directly indicates the maximum achievable V_{OC} and reflects the extent of non-radiative losses, the higher QFLS in GQ-processed films implies superior electronic quality and a greater capacity to support photovoltage under illumination. This enhancement likely results from both improved bulk properties and superior interface quality, as the GQ method may promote better contact between the perovskite layer and adjacent charge transport layers, further suppressing interfacial recombination.[200]

In addition to PLQY measurements, AFM is an essential characterization technique for examining nanoscale surface topography and roughness. It offers valuable insights into the surface properties of perovskite films, as shown in Figures 6.6c (AS) and 6.6d (GQ).

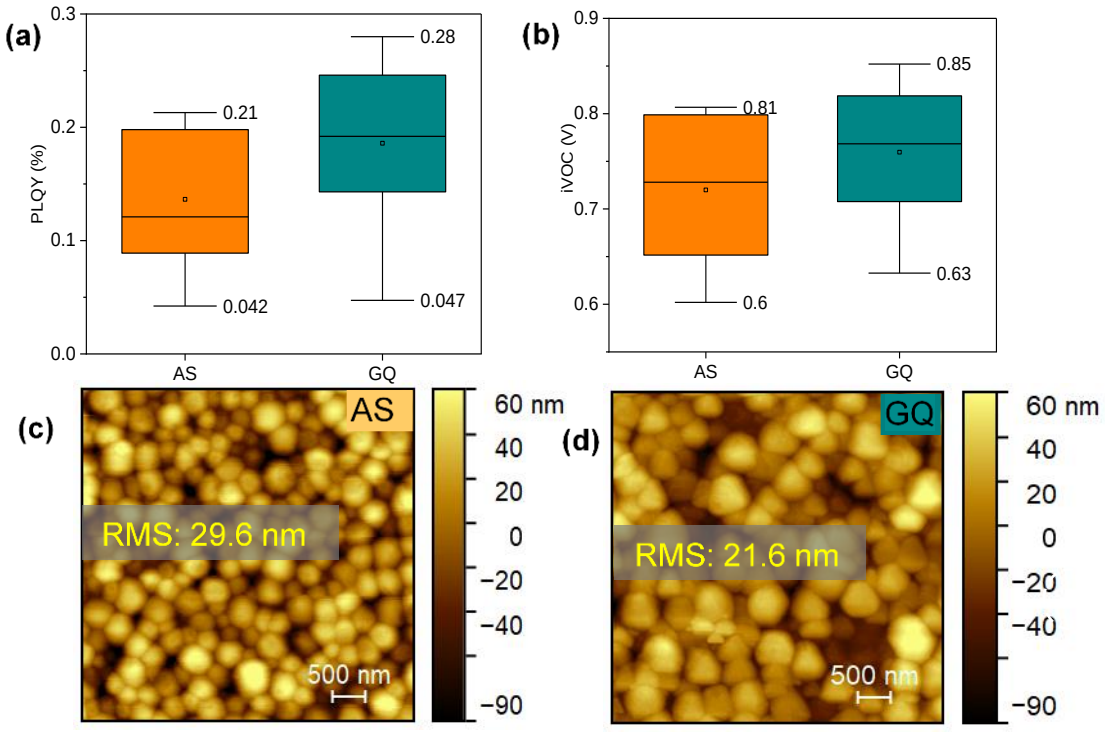

***Figure 6.6**: The photoluminescence quantum yield (a) and the quasi-fermi level splitting (b). Atomic force microscope topography images with root mean square (RMS) surface roughness of the perovskite film, under AS (c) and GQ (d) methods of the perovskite films. Reproduced from reference.[193]*

The film-forming properties of perovskite significantly influence the performance of PSC devices. The morphologies of perovskite layers prepared by the AS and GQ methods were examined using AFM. In both cases, topographic AFM images were obtained for perovskite films deposited on ITO/SAM/PEDOT: PSS substrates. The root mean square (RMS) roughness of the perovskite layer formed via the AS method is 29.6 nm, whereas the GQ-processed film exhibits a reduced RMS roughness of 21.6 nm. The AS film displays a less uniform surface compared to the GQ film. In contrast, the GQ perovskite film exhibits a smoother, more uniform topography, which is advantageous for the deposition of subsequent layers. Table S2.2 in the supporting information (SI) provides RMS and peak-to-valley roughness values corresponding to the AFM surface profiles of perovskite films prepared using the AS and GQ techniques.

In the next step, we investigated the crystallization process in greater detail to understand its role in film morphology. For this purpose, we employed in situ transmission measurements (detailed setup provided in the SI), as shown in Figures 6.7a and 6.7b. These measurements provide valuable insights into the crystallization dynamics of perovskite films processed via the AS and GQ methods, respectively. In the AS method, the antisolvent is dripped onto the spinning substrate within a fraction of a second. In contrast, in the GQ method, perovskite films are continuously dried under a directed nitrogen gas flow for 20 seconds. These differences in quenching type and duration affect the overall quenching rate. To investigate this effect, an in-situ transmittance setup was used to examine how the quenching rate influences the crystallization of the perovskite film. In both cases, in-situ transmittance measurements were conducted for 60 seconds, with the respective treatments applied at 15 seconds. Before this point, the perovskite precursor film remains in a liquid, transparent

state, resulting in high transmittance due to minimal light absorption. Upon dripping the antisolvent after 15 seconds, a rapid and sharp decrease in transmittance over approximately 5 seconds was observed, indicating a fast crystallization rate. This is attributed to the rapid extraction of coordinating solvents (DMF and DMSO) by the antisolvent (diethyl ether, DEE), which induces fast nucleation and crystallization of the perovskite phase. In contrast, GQ films show no significant change in transmittance during the first 5 seconds after quenching. After approximately 10 seconds, an apparent change in the transmission spectrum occurs, followed by another 10-15 seconds of gradual transmission shift. After 40 seconds, the transmission spectra of both films are very similar. These results suggest a comparatively slower crystallization rate for GQ samples. However, the perovskite films produced using the AS and GQ methods have ionization potentials of 5.47 eV and 5.44 eV, respectively. Both processing techniques yield films with relatively similar HOMO values, exhibiting only a slight shift in energy levels, as indicated by the small difference between the two values (see Figure S2.4).

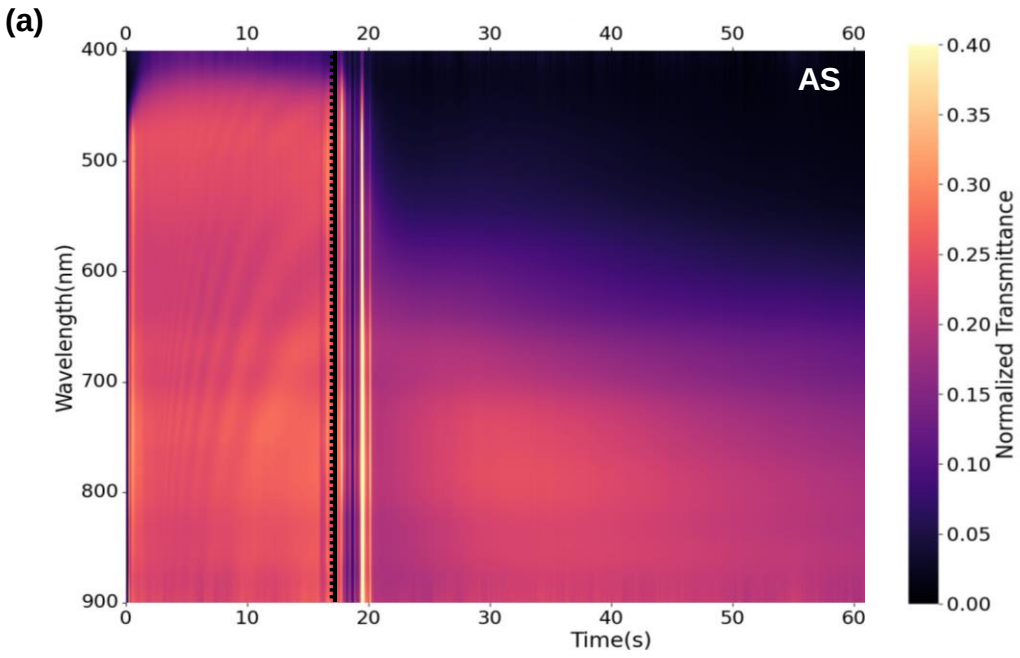

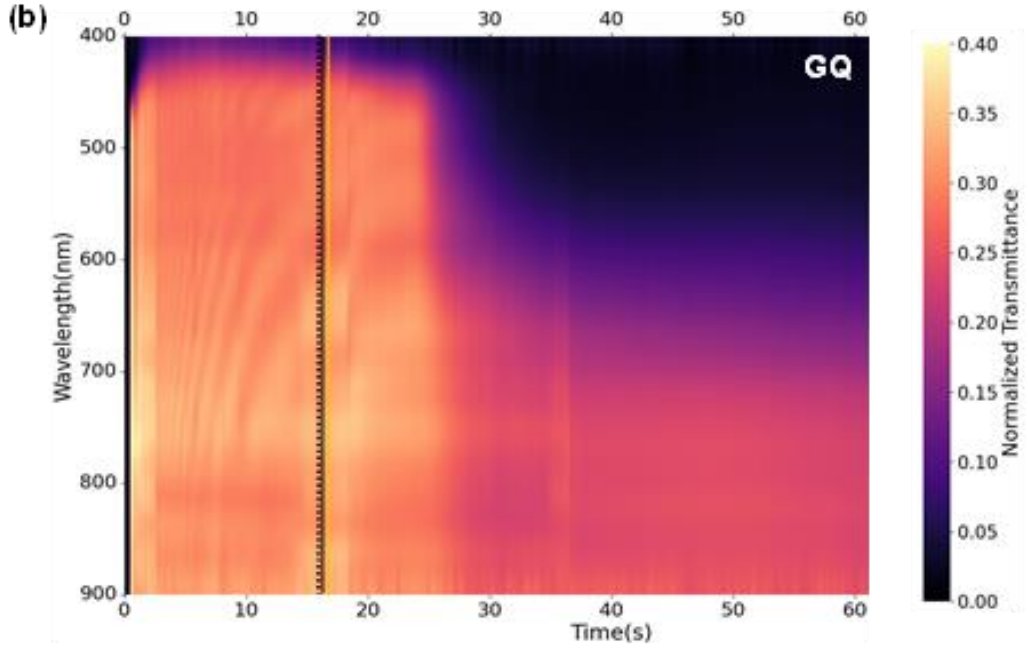

***Figure 6.7**: In-situ transmission spectra of the perovskite film during the spin-coating and quenching processes for the AS (a) and the GQ method (b). In both cases, quenching begins at approximately t = 15 s. Reproduced from reference.*[193]

Rapid crystallization is often induced by antisolvent quenching, which can lead to uncontrolled nucleation. This results in smaller grain sizes and increased defect density, negatively impacting charge transport and recombination.[201]

The slower crystallization process results in a range of grain sizes, as revealed by SEM analysis. Figure 6.8 provides a detailed comparison of the grain morphology of perovskite films deposited on PEDOT: PSS, which is coated on SAM-treated ITO substrates, under both AS and GQ processing conditions. The SEM images in Figures 6.8a (AS) and 6.8d (GQ) were used for grain size extraction, and Figures 6.8b and 6.8e highlight the identified grains via color segmentation. The corresponding histograms in Figures 6.8c and 6.8f, depicting the grain size distribution, reveal a slight difference between the two films: the AS films exhibit a mean grain size of approximately 0.25 μm, whereas the GQ films exhibit a larger mean grain size of roughly 0.3 μm. Although the width of the grain

size distributions is much greater than the difference observed between the GQ and AS samples, other distinct differences are evident in the histograms. A side peak appears at smaller grain sizes in the GQ film (Figure 6.8f), corresponding to smaller structures that form at grain boundaries and appear as light spots in Figure 6.8d.

The presence of these structures in the histogram shifts the mean and median of the GQ sample toward lower values. Therefore, the actual difference in grain sizes between the GQ and AS samples is likely larger than indicated here. This slight increase in grain size in the GQ method could be attributed to a slower crystallization rate, which slows film formation and, consequently, results in larger grains. Larger grains are known to reduce grain boundary density, thereby enhancing charge transport and reducing non-radiative recombination losses. This finding demonstrates a clear correlation among the SEM grain size analysis, PLQY measurements, and AFM topography results presented in this study.

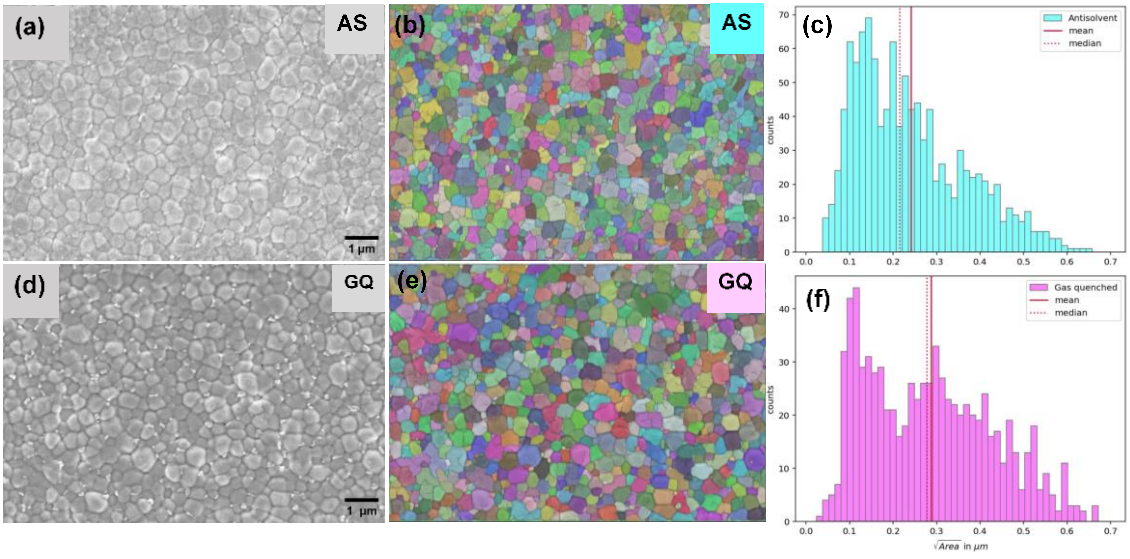

Figure 6.8*: SEM image of perovskite film at 10,000x magnification under AS (a) and GQ methods (d). The color scheme grain identified perovskite for the two techniques are illustrated in (b) and (e). Histogram of grain distribution of perovskite films induced by AS (c) and GQ (f). Reproduced from reference.*[193]

7 CONCLUSION AND OUTLOOK

7.1 Conclusion

This thesis focuses explicitly on the mixed tin–lead perovskite composition $(FASnI_3)_{0.6}(MAPbI_3)_{0.4}$ and the wide-bandgap $Cs_{0.3}FA_{0.6}MA_{0.1}Pb(I_{0.7}Br_{0.3})_3$, which were investigated as absorber layers in both single-junction Pb–Sn mixed PSCs and all-perovskite TSC architectures. These materials were selected for their complementary optoelectronic properties, enabling efficient photon harvesting across the solar spectrum and facilitating current matching in tandem configurations.

In the first project, we investigated the incorporation of an ultrathin PTAA layer atop the conventional HTL, PEDOT: PSS, to enhance charge transport across the HTL/perovskite interface. The resulting bilayer HTL configuration—PEDOT: PSS/PTAA—demonstrated significant improvements in device performance, as evidenced by J–V measurements. These improvements were reflected in the photovoltaic metrics of the fabricated PSCs, with a champion PCE of 20.3%, an improved J_{SC} of 32.3 mA/cm^2, a high FF of ~81%, and a high V_{OC} of 0.82 V. The V_{OC} achieved with the bilayer HTL ranks among the highest reported for Pb–Sn mixed narrow-bandgap PSCs, underscoring the effectiveness of this interfacial strategy. Further analysis revealed that the ionization-energy alignment between the HTLs and the narrow-bandgap perovskite was more favorable in the bilayer configuration, thereby facilitating improved charge extraction. Photoluminescence quantum yield (PLQY) measurements indicated superior interface quality in the PEDOT: PSS/PTAA/perovskite stack compared to single-layer HTLs. Additionally, electroluminescence (EL) measurements confirmed enhanced radiative recombination in bilayer HTL-based PSCs, attributed to the improved interfacial properties at the HTL/perovskite junction.

The second project focused on the structure of all-perovskite tandem solar cells. An optimized PTAA concentration (1.0 mg/mL) in bilayer HTL architectures significantly mitigates V_{OC} losses in Pb–Sn PSCs compared to devices with PEDOT: PSS or PTAA. This improvement results in enhanced photovoltaic parameters, including V_{OC}, J_{SC}, and FF, ultimately increasing overall solar cell efficiency and facilitating integration into high-performance all-perovskite tandem devices. The incorporation of optimized NBG Pb–Sn perovskite subcells, which exhibit reduced V_{OC} losses, into all-perovskite TSC architectures led to a marked enhancement in tandem device performance. The single-junction V_{OC} improvements successfully translated into the tandem configuration, achieving a high overall open-circuit voltage of 2.00 V and a power conversion efficiency exceeding 25%, ranking among the state of the art in the field. This chapter highlights the importance of synergistic optimization at both the material and device levels to achieve complementary subcell performance and voltage matching in tandem cells. The successful demonstration of high-V_{OC} NBG subcells within tandem stacks underscores their efficient photovoltaic performance. It lays the groundwork for future efforts toward commercialization and broader adoption of all-perovskite tandem technologies.

In the third project, we conducted a step-by-step comparison of AS and GQ devices for our Sn-Pb-based NBG perovskite. Devices fabricated using GQ exhibited minimal hysteresis (0.002) in light J-V scans and superior diode characteristics in dark J-V analysis, indicating reduced defect-mediated recombination. In contrast, AS films showed a pronounced hysteresis index of 0.018. Furthermore, GQ devices demonstrated a higher champion of 19.1%, compared to 18.3% for AS devices. Additionally, we observed a slower crystallization rate in perovskites processed with GQ, as evidenced by in-situ measurements. SEM grain analysis revealed that, due to the slower crystallization rate in GQ films, the perovskite grain size was comparatively larger than in AS films. PLQY measurements indicated a higher PLQY for GQ films,

suggesting a lower defect density. AFM analysis showed that GQ films were smoother than AS films. These results underscore the effectiveness of the gas quenching method as a strategy for producing high-performance perovskite solar cells. Gas quenching, in particular, has demonstrated promise in enhancing repeatability and device performance in Pb-Sn mixed perovskites. This factor is very important in the industrial production of such cells. Additionally, GQ offers a more sustainable processing method that does not use solvents. Although this study focuses on Sn-Pb-based films, other results from our group demonstrate that the performance of GQ-processed films also improves for other perovskite compositions. Therefore, GQ is generally preferred over AS treatment because it offers not only a more sustainable, less toxic preparation process, but also a slower crystallization rate, improved film quality, enhanced repeatability, more stable device performance, and superior photovoltaic efficiency.

7.2 Outlook

Building on the findings of this dissertation, future research aimed at reducing open-circuit voltage (Voc) losses in lead–tin (Pb–Sn) mixed perovskite solar cells should prioritize a deeper understanding of non-radiative recombination mechanisms and defect chemistry. This method includes exploring novel additive engineering strategies—such as multifunctional antioxidants with tailored functional groups—to suppress Sn^{2+} oxidation and passivate both bulk and interfacial trap states. A promising strategy involves compositional tuning, in which researchers precisely control the Sn:Pb ratio to optimize the bandgap without sacrificing film stability. Additionally, advanced characterization techniques such as time-resolved photoluminescence (TRPL), Kelvin probe force microscopy (KPFM), and in situ X-ray photoelectron spectroscopy (XPS) can provide critical insights into charge carrier dynamics and interfacial energetics. Investigating the synergistic effects of multiple additives and their influence on long-term stability and device lifetime will also be essential for translating lab-scale improvements into scalable technologies.

To enhance the Voc and power conversion efficiency (PCE) of all-perovskite tandem solar cells, future research should prioritize harmonizing bandgap tuning and interfacial charge extraction across subcells. These methods involve developing new wide-bandgap perovskite compositions with improved phase stability and minimized halide segregation, as well as optimizing narrow-bandgap absorbers through controlled tin (Sn) incorporation and defect passivation. Interface engineering remains crucial; therefore, designing novel interlayers—such as self-assembled monolayers (SAMs), doped organic semiconductors, or two-dimensional (2D) perovskite interphases—can enhance energy-level alignment and suppress interfacial recombination. Additionally, scalable, low-

temperature processing techniques compatible with flexible substrates, such as blade coating or inkjet printing, should be refined to maintain an optimal balance among optical transparency, conductivity, and mechanical robustness.

Finally, the gas-quenching method for perovskite film formation offers a scalable, reproducible approach to fabricating high-quality Pb–Sn mixed perovskite layers. Future research should focus on optimizing gas-flow parameters—including flow rate, direction, and temperature—to control solvent evaporation kinetics and crystallization behavior precisely. Combining gas quenching with additive engineering, such as incorporating passivating agents like phenethyl ammonium iodide (PEAI) or thiol-functionalized molecules, can further reduce defect densities and improve film uniformity. Investigating the compatibility of gas quenching with industrial-scale deposition techniques, such as slot-die coating or roll-to-roll processing, will be crucial for commercial applications. Moreover, understanding how gas-quenching influences interfacial contact with transport layers and its impact on charge extraction and recombination will help refine device architectures. Long-term stability studies under thermal, light, and environmental stress, alongside comprehensive morphological and optoelectronic characterization (e.g., GIWAXS, SEM, and transient absorption spectroscopy), will be essential to validate the robustness of this method. Ultimately, integrating gas quenching with comprehensive device-engineering strategies could set new performance benchmarks for Pb–Sn perovskite solar cells.

SUPPORTING INFORMATION

Appendix 1 Graphics, abstract, and supporting information for Chapter 4

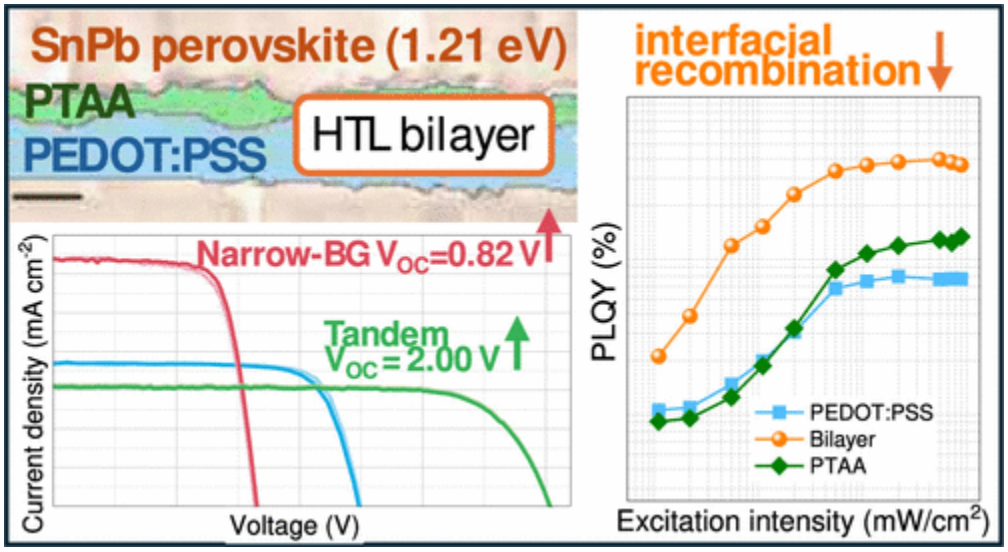

Figure S1.1: *Conceptual overview illustrating the core methodology and objectives of Project One in this thesis. Reproduced from the reference[89] under CC-BY 4.0.*

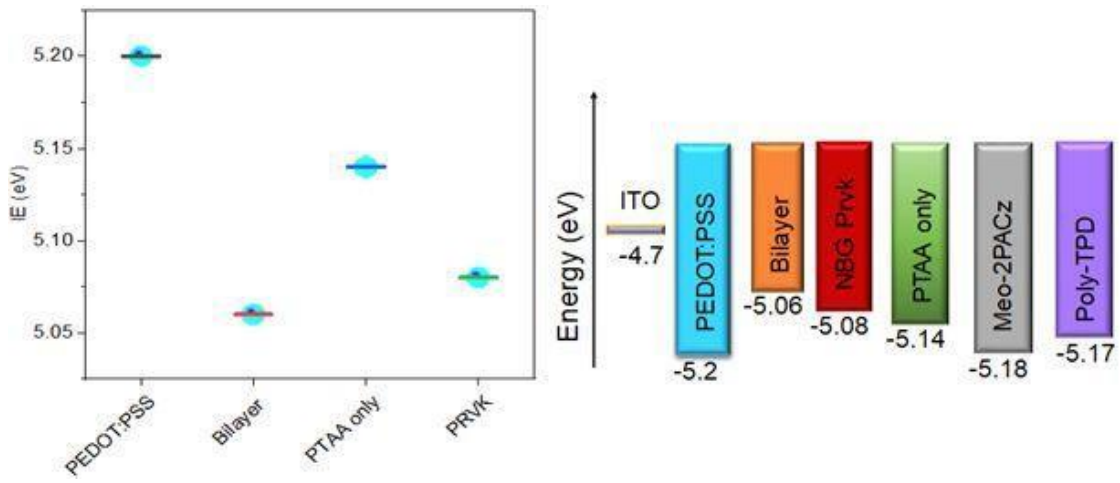

***Figure S1.2**: Ionization energy values of HTLs and NBG perovskite obtained by Photoelectron Spectroscopy in Air (PESA) and energy level alignment. Reproduced from the reference[89] under CC-BY 4.0.*

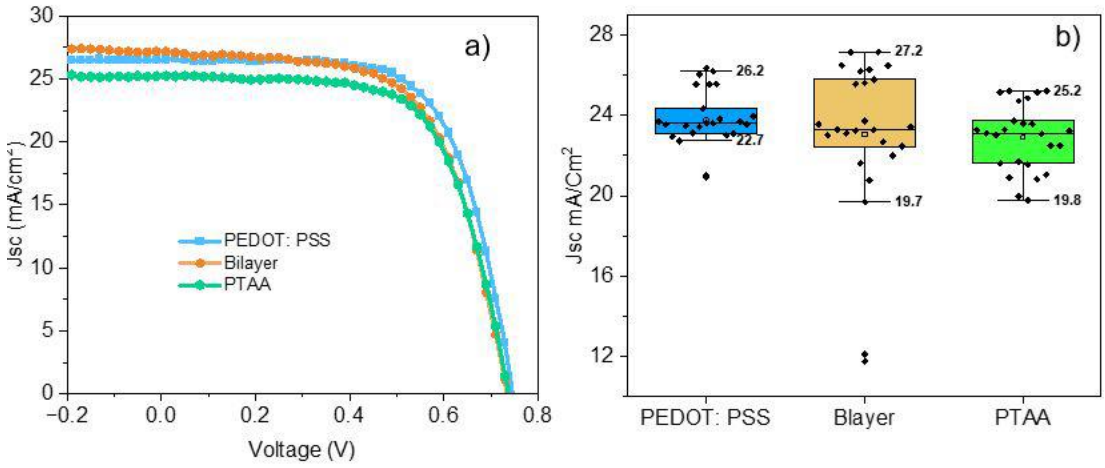

***Figure S1.3**. (a) J-V curves and (b) short circuit current of the three selected HTLs based PSCs without anti-reflection coating. Reproduced from the reference[89] under CC-BY 4.0.*

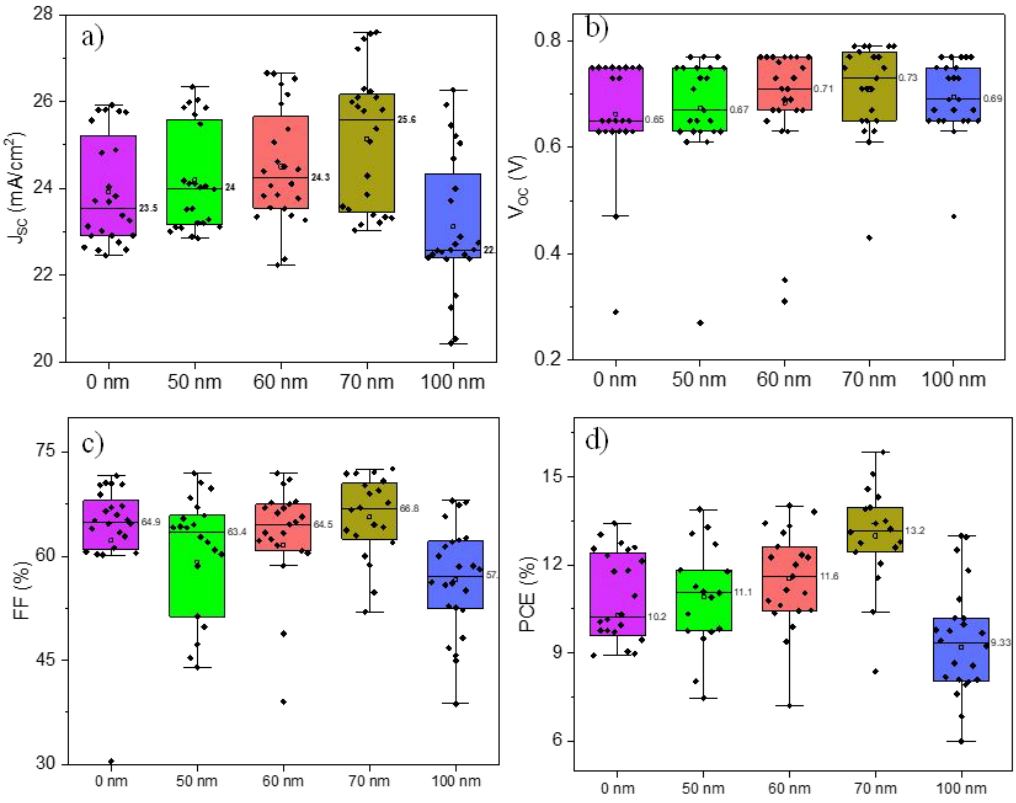

***Figure S1.4**: Influence of antireflective coating thicknesses (0 nm, 50 nm, 60 nm, 70 nm, and 100 nm) on J_{SC} of NBG PSCs. Reproduced from the reference[89] under CC-BY 4.0.*

The presence of an anti-reflection coating (ARC), such as MgF_2, enhances the current density in Sn-Pb PSCs by minimizing reflection and allowing more light to reach the absorber layer, thereby improving electron-hole pair generation and, consequently, PSC performance. In Figure S1.4, the 70 nm-thick MgF_2 appears to balance the reduction in reflection and the interference effects. At an optimized thickness (70 nm), the ARC reduces reflection over a wide range of wavelengths. When the ARC is too thick (100 nm), interference consequences emerge. Interference can cause destructive interference at specific wavelengths, which reduces overall light absorption.

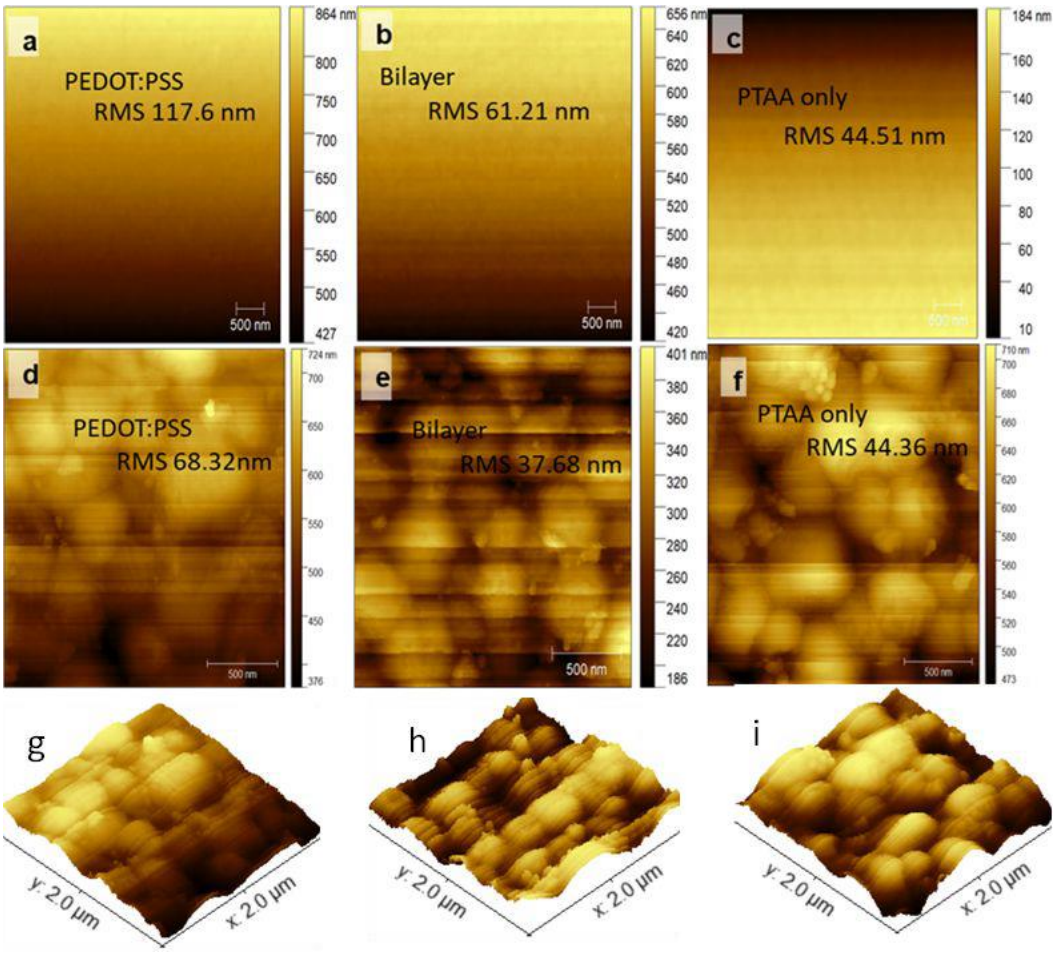

***Figure S1.5**: (a-c) AFM images of the three HTLs deposited on ITO (a) ITO/PEDOT: PSS, (b) ITO/PEDOT: PSS/PTAA, and (c) ITO/PTAA. (d-f) AFM images of the corresponding Sn-Pb perovskite film deposited on the respective HTLs. (g-i)3-D graphs of respective Sn-Pb perovskite film on representative HTLs. Reproduced from the reference[89] under CC-BY 4.0.*

The AFM images in Figure S1.5 represent the surface topography of the respective. Materials, with height variations measured at the nanoscale. From Figure S1.5 (a-c), the highest value (117.6 nm) implies significant roughness, while the subsequent HTLs (bilayer and PTAA only) values decrease, indicating smoother surfaces. The RMS roughness values for the perovskite layer, shown in Figure S1.5 (d-f) (68.32 nm, 37.68 nm, and 44.36 nm), provide insights into its surface quality; the lower RMS values suggest smoother surfaces with fewer irregularities. The three-dimensional AFM images of the three HTL-based perovskites are illustrated in Figure S1.5 (g-i).

***Table S1.1**: Photovoltaic parameters of PEDOT: PSS only, PEDOT: PSS /PTAA (bilayer), and PTAA only based single junction NBG-perovskite champion PSCs. Reproduced from reference[89] under CC-BY 4.0.*

HTLs	Scan directions	J_{SC} (mA/cm²)	V_{OC} (V)	FF (%)	PCE (%)
PEDOT:PSS	Forward	30.2	0.73	71.2	15.7
	Reverse	30.3	0.80	73.5	17.8
Bilayer	Forward	32.2	0.81	77.0	19.8
	Reverse	32.1	0.82	81.0	20.3
PTAA only	Forward	30.4	0.75	60.0	15.7
	Reverse	30.0	0.77	69.6	16.0

Appendix 2 Graphics, abstract, and supporting information for Chapter 6

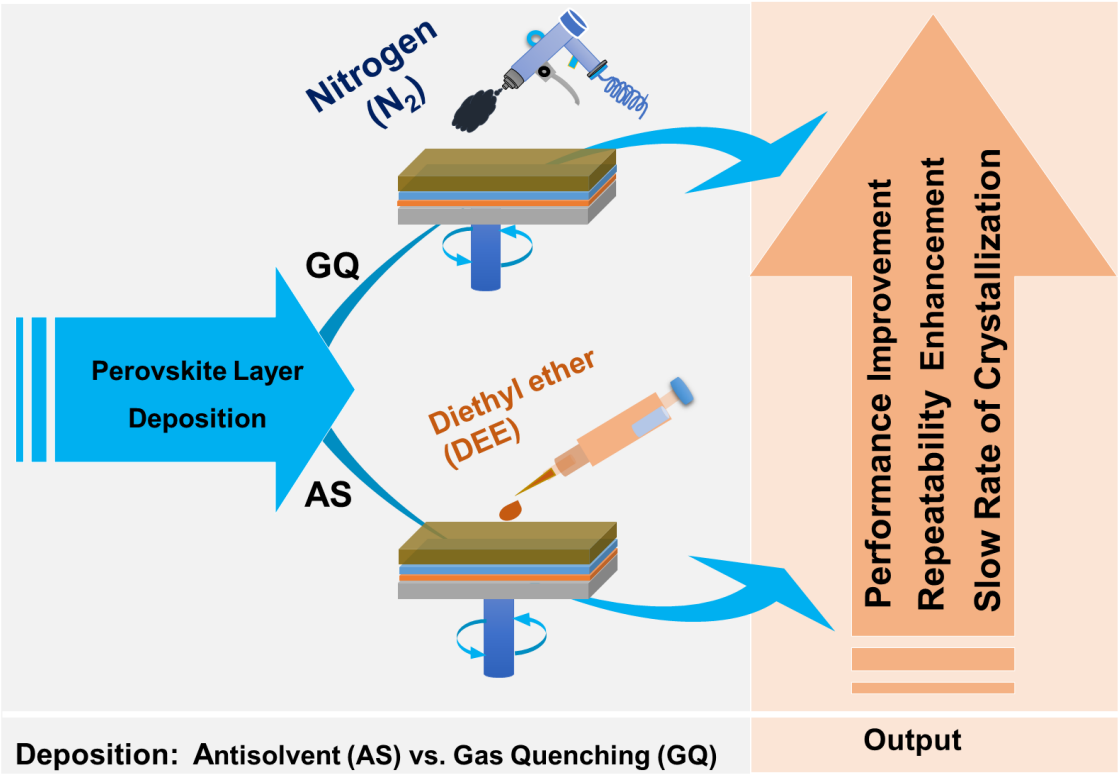

***Figure S2.1**: Schematic comparison of antisolvent dripping and gas quenching techniques for perovskite film formation, highlighting their influence on crystallization dynamics, repeatability, and resulting device performance. Reproduced from* the reference.[193]

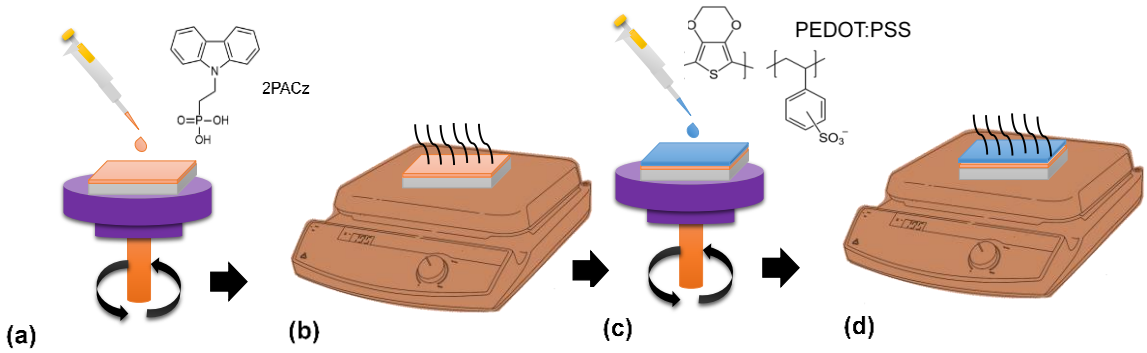

***Figure S2.2**: (a) Deposition of self-assembled monolayer (SAM); (b) Thermal annealing of SAM at 100 °C for 10 minutes; (c) Deposition of PEDOT:PSS layer over the SAM; (d) Annealing of the PEDOT:PSS film at 120 °C for 20 minutes. Reproduced from reference.*[193]

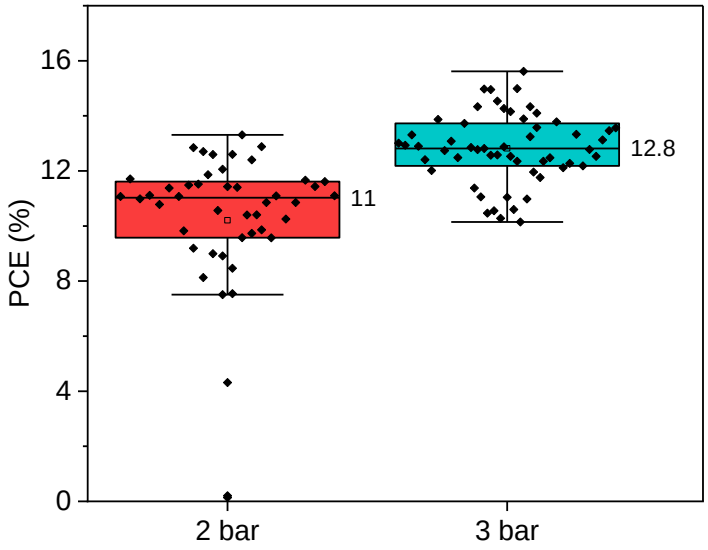

***Figure S2.3**: Box plots comparing the photovoltaic performance of devices fabricated via gas quenching at (a) 2 bar and (b) 3 bar pressures. Each plot represents the distribution of key performance metrics across multiple devices. Reproduced from reference*[193]

Figure S2.3 compares the photovoltaic performance of devices fabricated under different gas quenching pressures, using box plots to visualize the distribution of key metrics. Devices quenched at 2 bar and 3 bar pressures exhibit distinct performance characteristics. The box plots reflect variations in all photovoltaic parameters, such as, power conversion efficiency (PCE), open-circuit voltage

(V_{OC}), short-circuit current density (J_{SC}), and fill factor (FF), offering insights into the reproducibility and optimization of the fabrication process.

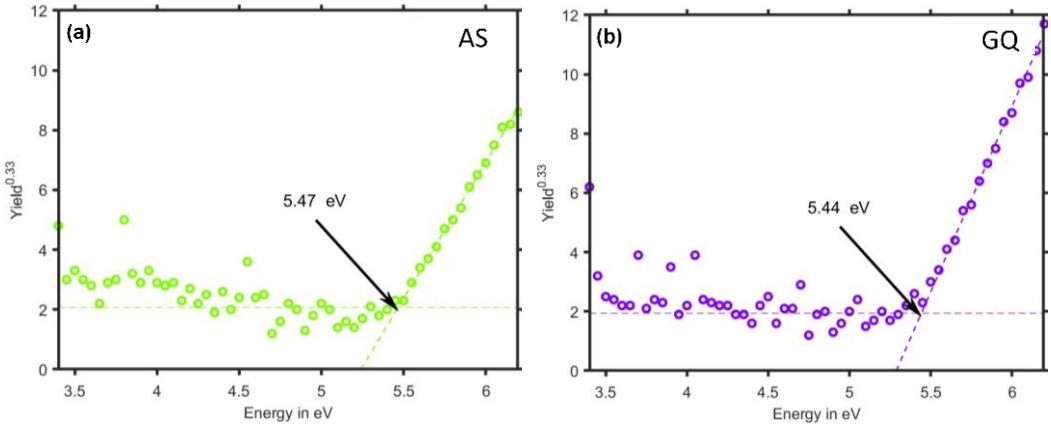

***Figure S2.4**: Work function analysis of perovskite films grown on SAM/PEDOT:PSS layers using photoelectron spectroscopy in air (PESA), comparing samples prepared via anti solvent (AS) and gas quenching (GQ) methods. Reproduced from reference.*[193]

Figure S2.4 shows the work function of perovskite films deposited on SAM/PEDOT:PSS layers, comparing results obtained under ambient conditions using antisolvent (AS) and gas-quenching (GQ) techniques. The work function is a critical parameter that influences energy level alignment. These measurements, typically obtained through techniques such as photoelectron spectroscopy (PESA), underscore the importance of processing conditions in tuning interfacial energetics.

***Table S2.1**: A comprehensive summary of the average and champion values of the photovoltaic parameters for perovskite solar cells. These cells were subjected both AS methods and GQ techniques. Parameters include power conversion efficiency (PCE), open-circuit voltage (V_{OC}), short-circuit current density (J_{SC}), and fill factor (FF). Reproduced from reference.*[193]

Techniques	Average and champion cells value	J_{SC} (mA/cm^2)	V_{OC} (V)	FF (%)	PCE (%)
Antisolvent (AS)	Average	28.1	0.75	72.8	15
	Champion	29	0.77	80.9	18.3
Gas quenching (GQ)	Average	29.7	0.78	74.5	17.6
	Champion	31	0.79	78	19.1

***Table S2.2**: Quantitative analysis of surface roughness parameters. Reproduced from reference.*[193]

Parameters	Antisolvent (AS)	Gas quenching (GQ)
RMS roughness (Sq)	29.66 nm	21.65 nm
RMS (grain: wise)	29.66 nm	21.65 nm
Mean roughness (Sa)	23.68 nm	17.42 nm
Skew (Ssk)	-0.4447	-0.2064
Excess Kurtosis	0.4756	0.1153
Maximum peak height (Sp)	87.3 nm	59.9 nm
Maximum pit depth (Sv)	190.3 nm	94.9 nm

REFERENCES

1. Kamaraj, I. and Kamaraj, S. Introduction to energy storage and conversion. In *Materials for Boosting Energy Storage. Volume 1: Adv. Sustain. Energy Technol.,* **2024,** 1-27, 1477.

2. Raimi, D.; Zhu, Y.; Newell, R.G. and Prest, B.C. Global energy outlook Peaks or plateaus. Resour. Future*.,* **2024**.

3. Bilgen, S.E.L.Ç.U.K. Structure and environmental impact of global energy consumption. Renew. Sustain. Energy Rev*.,* **2014**, *38*, 890-902.

4. Ritchie, H. and Rosado, P. Energy Mix: Explore global data on where our energy comes from, and how this is changing. *Our Word Data,* **2024**.

5. Hassan, Q.; Viktor, P.; Al-Musawi, T.J.; Ali, B.M.; Algburi, S.; Alzoubi, H.M.; Al-Jiboory, A.K.; Sameen, A.Z.; Salman, H.M. and Jaszczur, M. The renewable energy role in the global energy Transformations. Renew. Energy Focus*,* **2024**, *48*, 100545.

6. Florini, A. The International Energy Agency in global energy governance. *Global Pol.,***2011**, *2*, 40-50.

7. McCollum, D.; Gomez Echeverri, L.; Riahi, K. and Parkinson, S. Sdg7: Ensure access to affordable, reliable, sustainable and modern energy for all, **2017**, 127-173.

8. Best research-cell efficiency chart | Photovoltaic research | NREL, url: http s://www.nrel.gov/pv/cell-efficiency (checked on: 05/21/**2025**).

9. Shao, S. and M.A. Loi. *The role of the interfaces in perovskite solar cells.* Adv. Mater. Interfaces, **2020**. 7(1), 1901469.

10. Hurley, S. Opportunities for Solar Energy. Expl. Sci., **2021**.

11. Blum, A.S. and Jähnert, M. The birth of quantum mechanics from the spirit of radiation theory. Stud. Hist. Philos. Sci., **2022**, *91*,125-147.

12. Machín, A. and Márquez, F. Advancements in photovoltaic cell materials: silicon, organic, and perovskite solar cells. *Materials,* **2024**, *17*(5),1165.

13. Mah, O. Fundamentals of Photovoltaic Materials. National Solar Power Research Institute. *Inc., California,* **1998.**

14. Choi, K.; Choi, H.; Min, J.; Kim, T.; Kim, D.; Son, S.Y.; Kim, G.W.; Choi, J. and Park, T. *A short review on interface engineering of perovskite solar cells: a self-assembled monolayer and its roles.* Solar RRL, **2020**. 4(2),1900251.

15. Anizelli, H.; David, T.W.; Tyagi, P.; Laureto, E. and Kettle, J. *Enhancing the stability of perovskite solar cells through functionalisation of metal oxide transport layers with self-assembled monolayers.* Solar Energy, **2020**. 203, 157-163.

16. Lê, K.; Heshmati, N.; Mathur, S. Potential and perspectives of halide perovskites in light emitting devices. Nano Convers. **2023**, 10 (1), 47.

17. Luo, S. and Daoud, W.A. Recent progress in organic-inorganic halide perovskite solar cells: mechanisms and material design. J. Mater. Chem. A., **2015**, 3 (17), 8992−9010.

18. Rudd, P.N. and J. Huang. *Metal ions in halide perovskite materials and devices.* Trends Chem., **2019**. 1(4), 394-409.

19. Wu, W.; Liu, Y.; Yao, J. and Ouyang, X. Mixed-cation halide perovskite doped with Rb+ for highly efficient photodetector. *Materials,* **2023**, *16*(10), 3796.

20. Kojima, A.; Teshima, K.; Shirai, Y. and Miyasaka, T. Organometal halide perovskites as visible-light sensitizers for photovoltaic cells. J. Am. Chem. Soc., **2009,** 131(17), 6050-6051.

21. Burschka, J.; Pellet, N.; Moon, S.J.; Humphry-Baker, R.; Gao, P.; Nazeeruddin, M.K. and Grätzel, M. Sequential deposition as a route to high-performance perovskite-sensitized solar cells. *Nature,* **2013**, *499*(7458), 316-319.

22. Kim, H.S.; Lee, C.R.; Im, J.H.; Lee, K.B.; Moehl, T.; Marchioro, A.; Moon, S.J.; Humphry-Baker, R.; Yum, J.H.; Moser, J.E. and Grätzel, M. Lead iodide perovskite sensitized all-solid-state submicron thin film mesoscopic solar cell with efficiency exceeding 9%. Sci. Rep., **2012**, *2*(1), 591.

23. Lee, M.M.; Teuscher, J., Miyasaka, T.; Murakami, T.N. and Snaith, H.J. Efficient hybrid solar cells based on meso-superstructured organometal halide perovskites. *science*, **2012**, *338*(6107), 643-647.

24. Li, F. and Jen, A.K.Y. Interface engineering in solution-processed thin-film solar cells. *Acc. Mater. Res.*, *3*(3), **2022**, 272-282.

25. Zhou, H.; Chen, Q.; Li, G.; Luo, S.; Song, T.; Duan, H.S.; Hong, Z.; You, J.; Liu, Y. and Yang, Y. 'Interface engineering of highly efficient perovskite solar cells', *Science*, 345(6196), **2014**, 542–546.

26. Sutherland, B.R. and Sargent, E.H. Perovskite photonic sources. *Nat. Photonics*, *10*(5), **2016**, 295-302.

27. Qin, C.; Matsushima, T.; Fujihara, T.; Potscavage Jr, W.J. and Adachi, C. 'Triplet and Singlet Exciton Dynamics in Organometal Halide Perovskites', *Adv. Materials*, **2014**, 26(24), 4059–4063.

28. Qin, Z.; Pols, M.; Qin, M.; Zhang, J.; Yan, H.; Tao, S. and Lu, X. *Over-18%-Efficiency Quasi-2D Ruddlesden–Popper Pb–Sn Mixed Perovskite Solar Cells by Compositional Engineering.* ACS Energy Lett., **2023**, 8(7), 3188-3195.

29. Assirey, E.A.R. *Perovskite synthesis, properties and their related biochemical and industrial application.* Saudi Pharm. J., **2019**, 27(6), 817-829.

30. Rudd, P.N. and J. Huan. *Metal ions in halide perovskite materials and devices.* Trends Chem., **2019**, 1(4), 394-409.

31. Gray, J.L. The physics of the solar cell. *Handb. Photovolt. Sci. Eng.,* **2011**, *2*, 82-128.

32. Becquerel, M.E. Memoir on the electrical effects produced under the influence of solar rays. *Proc. Natl. Acad. Sci. U.S.A.,* **1839**, *9*, 561-567.

33. Einstein, A. On a heuristic point of view concerning the production and transformation of light. *Ann. Phys.,* **1905**, *4*.

34. Meyers, G. Photovoltaic Dreaming 1875-1905: First attempts at commercializing PV. *Sustainable Enterp. Media Inc*., **2014**.

35. Chapin, D.M.; Fuller, C.S. and Pearson, G.L. A new silicon p-n junction photocell for converting solar radiation into electrical power. J. Appl. Phys*.,* **1954**, *25*(5), 676.

36. Burger, B.; 2017. *Fraunhofer institute for solar energy systems ISE*, photovoltaics Report. Tech. Rep, **2025**, accessed on 04.10.25

37. Maldonado, S. The importance of new “sand-to-silicon” processes for the rapid future increase of photovoltaics. ACS Energy Lett., **2020**, 3628–3632, 10.1021.

38. Lunardi, M.M.; Alvarez-Gaitan, J.P.; Chang, N.L. and Corkish, R. Life cycle assessment on PERC solar modules. *Sol. Energy Mater. Sol. Cells*, **2018***, 187*, 154-159.

39. Pastuszak, J. and Węgierek, P. Photovoltaic cell generations and current research directions for their development. Materials **2022**, 15(16).

40. Bhandari, K.P.; Collier, J.M.; Ellingson, R.J. and Apul, D.S. Energy payback time (EPBT) and energy return on energy invested (EROI) of solar photovoltaic systems: a systematic review and meta-analysis. Renew. Sustainable Energy Rev., **2015**, 47, 133–141.

41. Chen, L.X. Organic solar cells: recent progress and challenges. ACS Energy Lett., **2019**, 4(10), 2537–2539.

42. Al-Ashouri, A.; K¨ohnen, E.; Li, B.; Magomedov, A.; Hempel, H.; Caprioglio, P.; M´arquez, J.A.; Morales Vilches, A.B.; Kasparavicius, E.; Smith, J.A.; Phung, N.; Menzel, D.; Grischek, M.; Kegelmann, L.; Skroblin, D.; Gollwitzer, C.; Malinauskas, T.; Jo˘st, M.; Mati˘c, G.; Rech, B.; Schlatmann, R.; Topi˘c, M.; Korte, L.; Abate, A.; Stannowski, B.; Neher, D.; Stolterfoht, M.; Unold, T.; Getautis, V.; Albrecht, S. Monolithic perovskite/silicon tandem solar cell with >29% efficiency by enhanced hole extraction. Science, **2020**, 370 (6522), 1300–1309.

43. Kahmann, S. and Loi, M.A. Hot carrier solar cells and the potential of perovskites for breaking the Shockley–Queisser limit. J. Mater. Chem. C., **2019**, 7(9), 2471–2486.

44. Naimovi˘cius, L.; Bharmoria, P. and Moth-Poulsen, K. Triplet–triplet annihilation mediated photon upconversion solar energy systems. Mater. Chem. Front., **2023**, 7:12, 2297–2315.

45. Wagner, L.; Suo, J; Yang, B.; Bogachuk, D.; Gervais, E.; Pietzcker, R.; Gassmann, A. and Goldschmidt, J.C. The resource demands of multi-terawatt-scale perovskite tandem photovoltaics. Joule, **2024**, 8:4, 1142–1160.

46. Wurfel, P. The chemical potential of radiation. *J. Phys. C: Solid State Phys.*, **1982***, 15*(18), 3967.

47. Auger, P.: Sur les rayons β secondaires produits dans un gaz par des rayons X. Comptes rendusde l'Acad´emie des Sciences, 1923 177, 169–171.

48. Meitner, L. On the origin of the β-beam spectra of radioactive substances. *J. Phys.*, **1922**, *9*(1), 131-144.

49. Shockley, W. The Theory of p-n Junctions in Semiconductors and p-n Junction Transistors. *Bell Syst. Tech. J.*, **1949***, 28*(3), 435-489.

50. Shockley, W. and Queisser, H. Detailed balance limit of efficiency of p–n junction solar cells. In *Renewable energy,* **2018,** 2(35)-2(54).

51. Katz, E.A. Perovskite: name puzzle and German-Russian odyssey of discovery. *Helvetica Chimica Acta*, **2020**, *103*(6), 2000061.

52. Viswanathan, B.; Suryakumar, V.; Venugopal, B.; Roshna, S.H. and Hariprasad, N. Perovskite materials an introduction. *Chennai, Jun,* **2019**.

53. Sharma, D.; Mehra, R. and Raj, B. Comparative study of hole transporting layers commonly used in high-efficiency perovskite solar cells. *J. Mater. Sci.,* **2022**, *57*(45), 21172-21191.

54. Qiu, Z.; Li, N.; Huang, Z.; Chen, Q. and Zhou, H. Recent advances in improving phase stability of perovskite solar cells. *Small Methods,* **2020**, *4*(5), 1900877.

55. Li, Z.; Yang, M.; Park, J.S.; Wei, S.H.; Berry, J.J. and Zhu, K. Stabilizing perovskite structures by tuning tolerance factor: formation of formamidinium and cesium lead iodide solid-state alloys. Chem. Mater., **2016***, 28(1), 284-292.*

56. Valipour, F.; Yazdi, E.; Torabi, N.; Mirjalili, B.F. and Behjat, A. Improvement of the stability of perovskite solar cells in terms of humidity/heat via compositional engineering. *J. Phys. D: Appl. Phys.,* **2020**, *53*(28), 285501.

57. Shen, L.; Song, P.; Zheng, L.; Liu, K.; Lin, K.; Tian, W.; Luo, Y.; Tian, C.; Xie, L. and Wei, Z. Perovskite-type stabilizers for efficient and stable formamidinium-based lead iodide perovskite solar cells. *J. Mater. Chem. A.*, **2021**, *9*(36), 20807-20815.

58. Wehrenfennig, C.; Eperon, G. E.; Johnston, M. B.; Snaith, H. J. and Herz, L. M. High charge carrier mobilities and lifetimes in organo lead trihalide perovskites. *Adv. Mater.,* **2014**, 26, 1584–1589.

59. Snaith, H. J. Perovskites: the emergence of a new era for low-cost, high-efficiency solar cells. *J. Phys. Chem. Lett.,* **2013***,* 4, 3623–3630.

60. Jia, G.; Fang, Y.; Song, X.; Xie, M.; Liao, R.; Geng, T.; Zhang, C.; Zhang, A. and Yu, H. Electron transport layer materials of perovskite solar cells. *J. Mater. Sci.,* **2025**,1-26.

61. Ke, Q.B.; Wu, J.R.; Lin, C.C. and Chang, S.H. Understanding the PEDOT: PSS, PTAA and P3CT-X hole-transport-layer-based inverted perovskite solar cells. *Polymers,* **2022,** *14*(4), 823.

62. Marinova, N.; Valero, S. and Delgado, J.L. Organic and perovskite solar cells: Working principles, materials and interfaces. *J. Colloid Interface Sci.,***2017**, *488*, 373-389.

63. Jung, H.S. and Park, N.G. Perovskite solar cells: from materials to devices. *Small,* **2015**, *11*(1), 10-25.

64. Li, B.; Yao, Y.; Kan, C.; Hang, P.; Xie, J.; Yin, Q.; Zhang, D.; Yu, X. and Yang, D. Promising excitonic absorption for efficient perovskite solar cells. *Joule,* **2025**, *9*(2).

65. Seitz, M.; Magdaleno, A.J.; Alcázar-Cano, N.; Meléndez, M.; Lubbers, T.J.; Walraven, S.W.; Pakdel, S.; Prada, E.; Delgado-Buscalioni, R. and Prins, F. Exciton diffusion in two-dimensional metal-halide perovskites. *Nat. Commun.*, **2020**, *11*(1), 2035.

66. Bohn, B.J. *Exciton Dynamics in Lead Halide Perovskite Nanocrystals: Recombination, Dephasing and Diffusion*. Springer Nature, **2021**.

67. Sum, T.C. and Mathews, N. Advancements in perovskite solar cells: photophysics behind the photovoltaics. *Energy Environ. Sci.,* **2014**, *7*(8), 2518-2534.

68. Nath, B.; Ramamurthy, P.C.; Hegde, G. and Roy Mahapatra, D. Role of electrodes on perovskite solar cells performance: ISSS J. Micro Smart Syst.*,* **2022.**, *11*(1), 61-79.

69. Lukas, T.; Seo, S.; Holzhey, P.; Stewart, K.; Henderson, C.; Wagner, L.; Beynon, D.; Watson, T.M.; Kim, J.S.; Kohlstädt, M. and Snaith, H.J. Charge Extraction Multilayers Enable Positive-Intrinsic-Negative Perovskite Solar Cells with Carbon Electrodes. *ACS Energy Lett.,* **2025**, *10*(6), 2736-2742.

70. Le Corre, V.M.; Stolterfoht, M.; Perdigon Toro, L.; Feuerstein, M.; Wolff, C.; Gil-Escrig, L.; Bolink, H.J.; Neher, D. and Koster, L.J.A. Charge transport layers limiting the efficiency of perovskite solar cells: how to optimize conductivity, doping, and thickness. *ACS Appl. Energy Mater.,* **2019**, *2*(9), 6280-6287.

71. Alkarsifi, R.; Ackermann, J. and Margeat, O. Hole transport layers in organic solar cells: A review. *J. Met. Mater. Miner.,* **2022**, *32*(4), 1-22.

72. Singh, R.; Singh, P.K.; Bhattacharya, B. and Rhee, H.W. Review of current progress in inorganic hole-transport materials for perovskite solar cells. *Appl. Mater. Today,* **2019**, *14*, 175-200.

73. Yang, D.; Zhang, X.; Wang, K.; Wu, C.; Yang, R.; Hou, Y.; Jiang, Y.; Liu, S. and Priya, S. Stable efficiency exceeding 20.6% for inverted perovskite solar cells through polymer-optimized PCBM electron-transport layers. *Nano letters,* **2019**, *19*(5), 3313-3320.

74. Wang, D.; Ye, T. and Zhang, Y. Recent advances of non-fullerene organic electron transport materials in perovskite solar cells. *J. Mater. Chem. A.,* **2020**, *8*(40), 20819-20848.

75. Ramabadran, C.D. and Sudheer, K.S. A Study on the influence of different HTL and ETL layers on the performance of a P3HTI C 60 BA bulk heterojunction organic solar cell: CD Ramabadran and KS Sudheer. *Indian J. Phys.,* **2025**, *99*(1), 273-282.

76. Choi, J.; Song, S.; Hörantner, M.T.; Snaith, H.J. and Park, T. Well-defined nanostructured, single-crystalline TiO2 electron transport layer for efficient planar perovskite solar cells. *ACS nano,* **2016**, *10*(6), 6029-6036.

77. Reis, L.R.D.; Camacho, J.R. and Novacki, D.F. The Newton Raphson method in the extraction of parameters of PV modules. *Renew. Energy Power Qual. J,* **2017**, *1*(15), 634-639.

78. Cao, J.; Liu, C.K.; Xu, Y.; Loi, H.L.; Wang, T.; Li, M.G.; Liu, L. and Yan, F. High-Performance Ideal Bandgap Sn-Pb Mixed Perovskite Solar Cells Achieved by MXene Passivation. *Small,* **2024,** *20*(47), 2403920.

79. Gu, S.; Lin, R.; Han, Q.; Gao, Y.; Tan, H. and Zhu, J. Tin and mixed lead–tin halide perovskite solar cells: progress and their application in tandem solar cells. *Adv. Mater.,* **2020**, *32*(27),1907392.

80. Protesescu, L.; Yakunin, S.; Bodnarchuk, M.I.; Krieg, F.; Caputo, R.; Hendon, C.H.; Yang, R.X.; Walsh, A. and Kovalenko, M.V. Nanocrystals of cesium lead halide perovskites (CsPbX3, X= Cl, Br, and I): novel optoelectronic materials showing bright emission with wide color gamut. *Nano letters,* **2015**, *15*(6), 3692-3696.

81. Jung, H.S. and Park, N.G. Perovskite solar cells: from materials to devices. *Small,* **2015**, *11*(1), 10-25.

82. Saliba, M.; Correa-Baena, J.P.; Grätzel, M. Hagfeldt, A. and Abate, A. Perovskite solar cells: from the atomic level to film quality and device performance. *Angewandte Chemie International Edition,* **2018**, *57*(10), 2554-2569.

83. Zhao, B.; Abdi-Jalebi, M.; Tabachnyk, M.; Glass, H.; Kamboj, V.S.; Nie, W.; Pearson, A.J.; Puttisong, Y.; Gödel, K.C.; Beere, H.E. and Ritchie, D.A. High open-circuit voltages in tin-rich low-bandgap perovskite-based planar heterojunction photovoltaics. *Adv. Mater.,* **2017**, *29*(2), 1604744.

84. Miah, M.H.; Khandaker, M.U.; Hossen, M.J.; Ashrafi, N.E.; Jahan, I.; Shahinuzzaman, M.; Nur-E-Alam, M.; Hanfi, M.Y.; Ullah, M.H. and Islam, M.A. Lead-free alternatives and toxicity mitigation strategies for sustainable perovskite solar cells: a critical review. *Mater. Adv.,* **2025**, 6, 2718-2752.

85. Li, W.; Mi, T.; Tian, T.; Yang, M. and Pang, H. Mitigating Lead Toxicity in Halide Perovskite Solar Cells: Strategies for Sustainable Development. *Inorganics,* **2025**, *13*(4),123.

86. Suo, J., Pettersson, H. and Yang, B. Sustainable approaches to address lead toxicity in halide perovskite solar cells: A review of lead encapsulation and recycling solutions. *EcoMat,* **2025**, *7*(1), 12511.

87. Yang, J.; Wang, Z.; Zhao, X.; Gao, W.; Xing, G.; Wang, X.; Wang, L.; Li, C.; Wang, Y.; Ren, Y.; and Liu, W. Guiding vertical growth and improving the buried interface of Pb–Sn perovskite films with 2D perovskite seeds for efficient narrow-bandgap perovskite solar cells and tandems. *Energy Environ. Sci.,* **2025**, *18*(6), 2883-2894.

88. Yang, X.; Ma, T.; Hu, H.; Ye, W.; Li, X.; Li, M.; Zhang, A.; Ge, C.; Sun, X.; Zhu, Y. and Yan, S. Understanding and manipulating the crystallization of Sn–Pb perovskites for efficient all-perovskite tandem solar cells. *Nat. Photonics,* **2025**, 1-8.

89. Temitmie, Y.A.; Haider, M.I.; Cuzzupè, D.T.; Mercaldo, L.V.; Kraner, S.; Veneri, P.D.; Benor, A.; Fakharuddin, A. and Schmidt-Mende, L. *Overcoming the Open-Circuit Voltage Losses in Narrow Bandgap Perovskites for All-Perovskite Tandem Solar Cells.* ACS Mater. Lett., **2024**, 6, 5190 - 5198.

90. Schmidt-Mende, L.; Kraner, S. and Fakharuddin, A. Organic and hybrid solar cells: An introduction. De Gruyter Textbook Ser. Berlin/Boston, **2016**.

91. Khatoon, S.; Yadav, S.K.; Chakravorty, V.; Singh, J.; Singh, R.B.; Hasnain, M.S. and Hasnain, S.M. Perovskite solar cell's efficiency, stability and scalability: A review. *Mater. Sci. Energy Technol.,* **2023**, *6*, 437-459.

92. Habisreutinger, S.N.; Leijtens, T.; Eperon, G.E.; Stranks, S.D.; Nicholas, R.J. and Snaith, H.J. Carbon nanotube/polymer composites as a highly stable hole collection layer in perovskite solar cells. *Nano letters,* **2014**, *14*(10), 5561-5568.

93. Boyd, C.C.; Cheacharoen, R.; Leijtens, T. and McGehee, M.D. Understanding degradation mechanisms and improving stability of perovskite photovoltaics. *Chem. rev.,* **2018**, *119*(5), 3418-3451.

94. Cheng, Y. and Ding, L. Pushing commercialization of perovskite solar cells by improving their intrinsic stability. *Energy Environ. Sci.,* **2021**, *14*(6), 3233-3255.

95. Zhang, H.; Ren, X.; Chen, X.; Mao, J.; Cheng, J.; Zhao, Y.; Liu, Y.; Milic, J.; Yin, W.J.; Grätzel, M. and Choy, W.C. Improving the stability and performance of perovskite solar cells via off-the-shelf post-device ligand treatment. *Energy Environ. Sci.,* **2018**, *11*(8), 2253-2262.

96. Lanzetta, L.; Huerta Hernandez, L.; Vishal, B.; Xu, H.; Sharma, A.; De Wolf, S. and Baran, D. Tin–Lead Perovskite Solar Cells with Enhanced Reverse Bias Stability. *ACS Energy Lett.,* **2025**, *10*(5), 2093-2095.

97. Hu, Y.; Yuan, H.; Zhang, W.; Guo, X.; Sun, N.; Li, W.; Cui, Z.; Li, X. and Fang, J. Band bending reversal and enhanced electron mobility at the film surface achieved through a selective polishing strategy in tin–lead perovskite solar cells. *J. Mater. Chem. A.,* **2025**, *13*(22), 16508-16515.

98. Liu, L.; Liu, W.; Liu, Q.; Chen, Y.; Yang, X.; Zhang, Y. and Yi, Z. Synergistic Energy Level Alignment and Light-Trapping Engineering for Optimized Perovskite Solar Cells. *Coatings,* **2025**, *15*(7), 856.

99. Yang, Z.; Babu, B.H.; Wu, S.; Liu, T.; Fang, S.; Xiong, Z.; Han, L. and Chen, W. Review on practical interface engineering of perovskite solar cells: from efficiency to stability. *Solar RRL,* **2020**, *4*(2), 1900257.

100. Kim, J.H.; Im, S.H., Jeong, J. and Song, C.E. 2D materials and additives: a dual approach to high-performance tin perovskite solar cells. *Microstructures,* **2025**, *5*(3).

101. Zhu, Z.; Chueh, C.C.; Li, N.; Mao, C. and Jen, A.K.Y. Realizing Efficient Lead-Free Formamidinium Tin Triiodide Perovskite Solar Cells via a Sequential Deposition Route. *Adv. Mater,* **2018**, *30*, 1703800.

102. Lin, R.; Xiao, K.; Qin, Z.; Han, Q.; Zhang, C.; Wei, M.; Saidaminov, M.I.; Gao, Y.; Xu, J.; Xiao, M. and Li, A. Monolithic all-perovskite tandem solar cells with 24.8% efficiency exploiting comproportionation to suppress Sn (ii) oxidation in precursor ink. *Nature Energy,* **2019**, *4*(10), 864-873.

103. Diau, E.W.G.; Jokar, E. and Rameez, M. Strategies to Improve Performance and Stability for Tin-Based Perovskite Solar Cells. *ACS Energy Lett.,* **2019**, *4*, 1930–1937.

104. Yang, M.; Tian, R.; Sun, K.; Meng, Y.; Bai, Y.; Zhou, S.; Pan, H.; Gao, J.; Lu, X.; Wang, J. and Han, B. Achieving efficient all-perovskite tandem solar cells through the modulation of crystallization in Sn-Pb perovskite solar cells. *Sci. China Chem.,* **2025**, 1-9.

105. Liu, Q.; Li, A.; Chu, W.; Prezhdo, O.V. and Liang, W. Influence of intrinsic defects on the structure and dynamics of the mixed Pb–Sn perovskite: first principles DFT and NAMD simulations. *J. Mater. Chem. A.,* **2022**, *10*(1), 234-244.

106. Lv, S.; Gao, W.; Liu, Y.; Dong, H.; Sun, N.; Niu, T.; Xia, Y.; Wu, Z.; Song, L.; Ran, C. and Fu, L. Stability of Sn-Pb mixed organic–inorganic halide perovskite solar cells: Progress, challenges, and perspectives. *J. Energy Chem.,* **2022**, *65*, 371-404.

107. Wang, Z.; Gao, H.; Wu, D.; Meng, J.; Deng, J. and Cui, M. Defects and defect passivation in perovskite solar cells. *Molecules,* **2024**, *29*(9), 2104.

108. Lin, R.; Xiao, K.; Qin, Z.; Han, Q.; Zhang, C.; Wei, M.; Saidaminov, M.I.; Gao, Y.; Xu, J.; Xiao, M. and Li, A. Monolithic all-perovskite tandem solar cells with 24.8% efficiency exploiting comproportionation to suppress Sn (ii) oxidation in precursor ink. *Nature Energy,* **2019**, *4*(10), 864-873.

109. Ghimire, N.; Bobba, R.S.; Gurung, A.; Reza, K.M.; Laskar, M.A.R.; Lamsal, B.S.; Emshadi, K.; Pathak, R.; Afroz, M.A.; Chowdhury, A.H. and Chen, K. Mitigating open-circuit voltage loss in Pb–Sn low-bandgap perovskite solar cells via additive engineering. *ACS Appl. Energy Mater.,* **2021**, *4*(2), 1731-1742.

110. He, Z.; Wang, F.; Dong, Y.; Zhang, Y.; Yu, R.; Gao, F. and Tan, Z.A. Redox energy barrier management for efficient tin-lead perovskite solar cells. *Natl. Sci. Rev.,* **2025**, *12*(5), nwaf097.

111. Rajagopal, A.; Liang, P.W.; Chueh, C.C.; Yang, Z. and Jen, A.K.Y. Defect passivation via a graded fullerene heterojunction in low-bandgap Pb–Sn binary perovskite photovoltaics. *ACS Energy Lett.,* **2017**, *2*(11), 2531-2539.

112. Zhang, Y.; Li, C.; Zhao, H.; Yu, Z.; Tang, X.; Zhang, J.; Chen, Z.; Zeng, J.; Zhang, P.; Han, L. and Chen, H. Synchronized crystallization in tin-lead perovskite solar cells. *Nat. Commun.,* **2024**, *15*(1), 6887.

113. Werner, J.; Moot, T.; Gossett, T.A.; Gould, I.E.; Palmstrom, A.F.; Wolf, E.J.; Boyd, C.C.; van Hest, M.F.; Luther, J.M.; Berry, J.J. and McGehee, M.D. Improving low-bandgap tin–lead perovskite solar cells via contact engineering and gas quench processing. *ACS Energy Lett.,* **2020**, *5*(4), 1215-1223.

114. Li, X.; Nasti, G.; Dreessen, C.; Dagar, J.; Meitzner, R.; Amoroso, D.; Maffettone, P.L.; Kirchartz, T.; Unger, E.; Abate, A. and Dimitrov, S.D. Printing of tin perovskite solar cells via controlled crystallization. *Sustainable Energy & Fuels,* **2025**, *9*(8), 2063-2071.

115. Green, M.A.; Hishikawa, Y.; Dunlop, E.D.; Levi, D.H.; Hohl-Ebinger, J. and Ho-Baillie, A.W. Solar cell efficiency tables (version 52). *Progress in photovoltaics: Res. Appl.,* **2018**, *26*(7), 427-436.

116. Ghimire, N.; Bobba, R.S.; Gurung, A.; Reza, K.M.; Laskar, M.A.R.; Lamsal, B.S.; Emshadi, K.; Pathak, R.; Afroz, M.A.; Chowdhury, A.H. and Chen, K. Mitigating open-circuit voltage loss in Pb–Sn low-bandgap perovskite solar cells via additive engineering. *ACS Appl. Energy Mater.,* **2021**, *4*(2), 1731-1742.

117. Xu, X., Chueh, C.C., Yang, Z., Rajagopal, A., Xu, J., Jo, S.B. and Jen, A.K.Y. Ascorbic acid as an effective antioxidant additive to enhance the efficiency and stability of Pb/Sn-based binary perovskite solar cells. *Nano Energy,* **2017**, *34*, 392-398.

118. Kurisinkal Pious, J.; Zwirner, Y.; Lai, H.; Olthof, S.; Jeangros, Q.; Gilshtein, E.; Kothandaraman, R.K.; Artuk, K.; Wechsler, P.; Chen, C. and Wolff, C.M. Revealing the role of tin fluoride additive in narrow bandgap Pb-Sn perovskites for highly efficient flexible all-perovskite tandem cells. *ACS Appl. Mater. Interfaces,* **2023**, *15*(7), 10150-10157.

119. Chen, Q.; Luo, J.; He, R.; Lai, H. Ren, S.; Jiang, Y.; Wan, Z.; Wang, W.; Hao, X.; Wang, Y. and Zhang, J. Unveiling roles of tin fluoride additives in high-efficiency

low-bandgap mixed tin-lead perovskite solar cells. *Adv. Energy Mater.,* **2021**, *11*(29), 2101045.

120. Li, C.; Zhu, M.; Jiang, H.; Zhang, S.; Cheng, J.; Cao, H.; Wang, T. and Zhou, Z. Multiple active site additive-mediated suppression of Sn 2+ oxidation and regulation of crystallization for high-performance Sn–Pb mixed perovskite solar cells. *Materials Horizons,* **2025**, *12*(13), 4813-4821.

121. Lee, S. J.; Shin, S. S.; Kim, Y. C.; Kim, D.; Ahn, T. K.; Noh, J. H.; Seo, J. and Seok, S.I. Fabrication of Efficient Formamidinium Tin Iodide Perovskite Solar Cells through SnF 2 – Pyrazine Complex. *J. Am. Chem. Soc.,* **2016**, *138*, 3974– 3977.

122. Liao, W.; Zhao, D.; Yu, Y.; Grice, C. R.; Wang, C.; Cimaroli, A. J.; Schulz, P.; Meng, W.; Zhu, K. and Xiong, R.-G. Lead-Free Inverted Planar Formamidinium Tin Triiodide Perovskite Solar Cells Achieving Power Conversion Efficiencies up to 6.22%. *Adv. Mater.,* **2016**, *28*, 9333– 9340.

123. Tai, Q.; Guo, X.; Tang, G.; You, P.; Ng, T.-W.; Shen, D.; Cao, J.; Liu, C.-K.; Wang, N.; Zhu, Y. and Lee, C.S. Antioxidant Grain Passivation for Air-Stable Tin-Based Perovskite Solar Cells. *Angew. Chem., Int. Ed.,* **2019**, *58*, 806–810.

124. Zhu, M.; Cao, G. and Zhou, Z. Recent progress toward highly efficient tin-based perovskite (ASnX3) solar cells. *Nano Select,* **2021**, *2*(6), 1023-1054.

125. Pan, Y.; Wang, J.; Sun, Z.; Zhang, J.; Zhou, Z.; Shi, C.; Liu, S.; Ren, F., Chen, R., Cai, Y. and Sun, H. Surface chemical polishing and passivation minimize non-radiative recombination for all-perovskite tandem solar cells. *Nat. Commun.,* **2024**, *15*(1), 7335.

126. Li, T.; Ma, F.; Hao, Y.; Wu, H.; Zhu, P.; Li, Z.; Li, F.; Yu, J.; Liu, M.; Lei, C. and Liang, T. Defect Passivation for Highly Efficient and Stable Sn-Pb Perovskite Solar Cells. *Crystals,* **2024**, *14*(9), 802.

127. Huang, H.; Zhang, X.; Zhou, W.; Huang, Y.; Zheng, Z.; Chen, X.; Zhang, Y. and Yan, H. Interface passivation strategies for high-performance perovskite solar cells using two-dimensional perovskites. *Mater. Chem. Front.,* **2024**, *8*(21), 3528-3557.

128. Yang, Z.; Rajagopal, A.; Chueh, C.C.; Jo, S.B.; Liu, B.; Zhao, T. and Jen, A.K.Y. Stable low-bandgap Pb-Sn binary perovskites for tandem solar cells. *Adv. Mat.,* **2016**, *28* (DOE-UW-Jen-33).

129. Liu, M.; Chen, Z.; Yang, Y.; Yip, H.L. and Cao, Y. Reduced open-circuit voltage loss for highly efficient low-bandgap perovskite solar cells via suppression of silver diffusion. *J. Mater. Chem. A.,* **2019**, *7*(29), 17324-17333.

130. Huang, F.; Dkhissi, Y.; Huang, W.; Xiao, M.; Benesperi, I.; Rubanov, S.; Zhu, Y.; Lin, X.; Jiang, L.; Zhou, Y. and Gray-Weale, A. Gas-assisted preparation of lead iodide perovskite films consisting of a monolayer of single crystalline grains for high efficiency planar solar cells. *Nano energy,* **2014**, *10*, 10-18.

131. Ternes, S.; Laufer, F. and Paetzold, U.W. Modeling and fundamental dynamics of vacuum, gas, and antisolvent quenching for scalable perovskite processes. *Adv. Sci.,* **2024**, *11*(14), 2308901.

132. Rajagopal, A.; Yang, Z.; Jo, S.B.; Braly, I.L.; Liang, P.W.; Hillhouse, H.W. and Jen, A.K.Y. Highly efficient perovskite–perovskite tandem solar cells reaching 80% of the theoretical limit in photovoltage. *Adv. Mater.,* **2017**, *29*(34), 1702140.

133. Zhu, H.L. and Choy, W.C. Crystallization, Properties, and Challenges of Low-Bandgap Sn–Pb Binary Perovskites. *Solar RRL,* **2018**, *2*(10), 1800146.

134. Yang, Z.; Yu, Z.; Wei, H.; Xiao, X.; Ni, Z.; Chen, B.; Deng, Y.; Habisreutinger, S.N.; Chen, X.; Wang, K. and Zhao, J. Enhancing electron diffusion length in narrow-bandgap perovskites for efficient monolithic perovskite tandem solar cells. *Nat. Commun.,* **2019**, *10*(1), 4498.

135. Azhar, M.; Yalcinkaya, Y.; Cuzzupè, D.T.; Temitmie, Y.; Haider, M.I. and Schmidt-Mende, L. Perovskite Thin Films Solar Cells: The Gas Quenching Method, **2025,** 1(1), 5, 2982-2785.

136. Werner, J.; Moot, T.; Gossett, T.A.; Gould, I.E.; Palmstrom, A.F.; Wolf, E.J.; Boyd, C.C.; van Hest, M.F.; Luther, J.M.; Berry, J.J. and McGehee, M.D. Improving low-bandgap tin–lead perovskite solar cells via contact engineering and gas quench processing. *ACS Energy Lett.,* **2020**, *5*(4), 1215-1223.

137. Wen, J.; Hu, H.; Chen, C.; McMeekin, D.P.; Xiao, K.; Lin, R.; Liu, Y.; Snaith, H.J.; Tang, J.; Paetzold, U.W. and Tan, H. Present status of and future opportunities for all-perovskite tandem photovoltaics. *Nat. Energy,* **2025**, 1-16.

138. Aziz, M.W.; Ahmad, N.A. and Hamed, H.W. An Overview of High-Efficiency Perovskite and Perovskite-Based Tandem Solar Cells: Progress in 2025. Sci. J. Eng. Technol.*,* **2025**, *2*(2), 114-118.

139. Lim, J.; Park, N.G.; Seok, S.I. and Saliba, M. All-perovskite tandem solar cells: from fundamentals to technological progress. *Energy Environ. Sci.,* **2024**, *17*(13), 4390-4425.

140. Miah, M.H.; Khandaker, M.U.; Hossen, M.J.; Ashrafi, N.E.; Jahan, I.; Shahinuzzaman, M.; Nur-E-Alam, M.; Hanfi, M.Y.; Ullah, M.H. and Islam, M.A.

Lead-free alternatives and toxicity mitigation strategies for sustainable perovskite solar cells: a critical review. *Mater. Adv.,* **2025** , 6, 2718-2752.

141. Ferrara, C.; Patrini, M.; Pisanu, A.; Quadrelli, P.; Milanese, C.; Tealdi, C. and Malavasi, L. Wide bandgap tuning in Sn-based hybrid perovskites through cation replacement: the FA 1− x MA x SnBr 3 mixed system. J. Mater. Chem. A*.,* **2017**, *5*(19), 9391-9395.

142. Li, Q.; Chai, W.; Luo, X.; Zhu, W.; Chen, D.; Zhou, L.; Xi, H.; Dong, H.; Zhang, C. and Hao, Y. Wide-Bandgap Subcells for All-Perovskite Tandem Solar Cells: Recent Advances, Challenges, and Future Perspectives. *Energies,* **2025**, *18*(10), 2415.

143. Hu, S.; Thiesbrummel, J.; Pascual, J.; Stolterfoht, M.; Wakamiya, A. and Snaith, H.J. Narrow bandgap metal halide perovskites for all-perovskite tandem photovoltaics. Chem. Rev*.,* **2024**, *124*(7), 4079-4123.

144. Lee, J.Y.; Lee, S.; Ryu, J. and Kang, D.W. Bandgap engineering via doping strategies for narrowing the bandgap below 1.2 eV in Sn/Pb binary perovskites: unveiling the role of Bi3+ incorporation on different A-site compositions. *Nanomaterials,* **2024**, *14*(19), 1554.

145. Rafiq, M.; Li, H. and Yang, J. Four-terminal perovskite tandem solar cells. *iEnergy,* **2024**, *3*(4), 216-241.

146. Zhang, Q.; Chen, X.; Lim, E.L.; Shi, L. and Wei, Z. Advancing all-perovskite two-terminal tandem solar cells: optimization of wide-and narrow-bandgap perovskites and interconnecting layers. Energy Environ. Sci*.,* **2025,**18**,** 3060-3084.

147. Wen, J.; Hu, H.; Chen, C.; McMeekin, D.P.; Xiao, K.; Lin, R.; Liu, Y.; Snaith, H.J.; Tang, J.; Paetzold, U.W. and Tan, H. Present status of and future opportunities for all-perovskite tandem photovoltaics. Nat. Energy*,* **2025**, 1-16.

148. Chin, Y.C.; Daboczi, M.; Henderson, C.; Luke, J. and Kim, J.S. Suppressing PEDOT: PSS doping-induced interfacial recombination loss in perovskite solar cells. ACS Energy Lett*.,* **2022**, *7*(2), 560-568.

149. Qi, Y.; Almtiri, M.; Giri, H.; Jha, S.; Ma, G.; Shaik, A.K.; Zhang, Q.; Pradhan, N.; Gu, X.; Hammer, N.I. and Patton, D. Evaluation of the passivation effects of PEDOT: PSS on inverted perovskite solar cells. Adv. Energy Mater*.,* **2022**, *12*(46), 2202713.

150. Sun, Q.; Li, Z.; Cheng, T.; Ma, G.; He, D.; Su, G.; Chen, H.; Yin, L. and He, Z. Unveiling Popular PEDOT: PSS-Derived Composition Segregation Effect in Tin–Lead Mixed Perovskite Solar Cells and Elimination. *J. Phys. Chem. Lett.,* **2025**, *16*(9), 2348-2356.

151. Yang, Z.; Rajagopal. and A.; Jen, A. K. Y. Ideal Bandgap Organic-Inorganic Hybrid Perovskite Solar Cells. *Adv. Mater.,* **2017**, *29* (47), 1704418.

152. Zeng, L.; Chen, Z.; Qiu, S.; Hu, J.; Li, C.; Liu, X.; Liang, G.; Brabec, C.J.; Mai, Y. and Guo, F. 2D-3D heterostructure enables scalable coating of efficient low-bandgap Sn–Pb mixed perovskite solar cells. *Nano Energy,* **2019**, *66*, 104099.

153. Tang, H.; Shang, Y.; Zhou, W.; Peng, Z. and Ning, Z. Energy Level Tuning of PEDOT: PSS for High Performance Tin-Lead Mixed Perovskite Solar Cells. *Solar RRL,* **2019**, *3*(2), 1800256.

154. Lee, S.; Woo, M. Y.; Kim, C.; Kim, K. W.; Lee, H.; Kang, S. B.; Im, J. M.; Jeong, M. J.; Hong, Y.; Yoon, J. W. Buried interface modulation via PEDOT: PSS ionic exchange for the Sn Pb mixed perovskite based solar cells. Chem. Eng. J.*,* **2024**, *479*, 147587.

155. Li, S.; Cao, Y.-L.; Li, W.H. and Bo, Z.S.A brief review of hole transporting materials commonly used in perovskite solar cells. *Rare Metals,* **2021**, *40* (10), 2712-2729.

156. Qin, Z.; Pols, M.; Qin, M.; Zhang, J.; Yan, H.; Tao, S. and Lu, X. Over-18%-Efficiency Quasi- 2D Ruddlesden– Popper Pb–Sn Mixed Perovskite Solar Cells by Compositional Engineering. ACS Energy Lett.*,* **2023**, *8* (7), 3188-3195.

157. Qiu, C.; Wei, Y.; Lei, Y.; Li, S.; Zhuang, K.; An, B. and Li, H. Obviously decreased hysteresis index originated from enhanced grain size with ETL modification for improved performance of perovskite solar cells. *J. Mater. Sci.: Mater. Electron.*, **2024**, *35*(22), 1505.

158. Caprioglio, P.; Stolterfoht, M.; Wolff, C. M.; Unold, T.; Rech, B.; Albrecht, S. and Neher, D. On the Relation between the Open-Circuit Voltage and Quasi-Fermi Level Splitting in Efficient Perovskite Solar Cells. *Adv. Energy Mater.,* **2019**, *9* (33), 1901631.

159. Herterich, J.; Unmüssig, M.; Wagner, L.; Loukeris, G.; Faisst, J.; List, M.; Kohlstädt, M. and Würfel, U. Decoupling of Implied and External V OC Due to Ionic Movement Explaining Transient VOC Overshoot in Perovskite Solar Cells. *Energy Technol.,* **2022**, *10*(2), 2100868.

160. Wong, K. K.; Fakharuddin, A.; Ehrenreich, P.; Deckert, T.; Abdi-Jalebi, M.; Friend, R. H. and Schmidt-Mende, L. Interface-Dependent Radiative and Nonradiative Recombination in Perovskite Solar Cells. *J. Phys. Chem. C,* **2018**, *122* (20), 10691– 10698.

161. Fakharuddin, A.; Qiu, W.; Croes, G.; Devižis, A.; Gegevičius, R.; Vakhnin, A.; Rolin, C.; Genoe, J.; Gehlhaar, R. and Kadashchuk, A.Reduced efficiency roll-off and

improved stability of mixed 2D/3D perovskite light emitting diodes by balancing charge injection. *Adv. Funct. Mater.,* **2019**, *29* (37), 1904101.

162. Levine, I.; Al-Ashouri, A.; Musiienko, A.; Hempel, H.; Magomedov, A.; Drevilkauskaite, A.; Getautis, V.; Menzel, D.; Hinrichs, K.; Unold, T. and Albrecht, S. Charge transfer rates and electron trapping at buried interfaces of perovskite solar cells. *Joule,* **2021**, *5*(11), 2915-2933.

163. de Quilettes, D. W.; Vorpahl, S. M.; Stranks, S. D.; Nagaoka, H.; Eperon, G. E.;Ziffer, M. E.; Snaith, H. J. and Ginger, D. S. Impact of microstructure on local carrier lifetime in perovskite solar cells. *Science,* **2015**, *348* (6235).

164. Jeong, J.; Kim, M.; Seo, J.; Lu, H.; Ahlawat, P.; Mishra, A.; Yang, Y.; Hope, M. A.; Eickemeyer, F. T.; Kim, M. and Yoon, Y.J. Pseudo-halide anion engineering for α-FAPbI3 perovskite solar cells. *Nature,* **2021**, *592* (7854).

165. Tao, S.; Schmidt, I.; Brocks, G.; Jiang, J.; Tranca, I.; Meerholz, K. and Olthof, S. Absolute energy level positions in tin- and lead-based halide perovskites. Nat. Commun.*,* **2019**, *10* (1).

166. Li, S.; Jiang, Y.; Xu, J.; Wang, D.; Ding, Z.; Zhu, T.; Chen, B.; Yang, Y.; Wei, M.; Guo, R. and Hou, Y. High-efficiency and thermally stable FACsPbI3 perovskite photovoltaics. *Nature,* **2024,** 635, 82-88.

167. Yin, Y.; Yang, L.; Zhang, X. and Zhang, J. Pernicious effects and management of lead leakage from perovskite solar cells. *J. Mater. Chem. A.,* **2023**, *11*(47), 25825-25848.

168. Mokabane, P.T.; Lukong, V.T. and Jen, T.C. A review of the effect of stability issues and wide-bandgap in the application of perovskite solar cells. *Mater. Renew. Sustain. Energy,* **2025**, *14*(2), 34.

169. Hao, F.; Stoumpos, C.C.; Guo, P.; Zhou, N.; Marks, T.J.; Chang, R.P. and Kanatzidis, M.G. Solvent-mediated crystallization of CH3NH3SnI3 films for heterojunction depleted perovskite solar cells. J. Am. Chem. Soc.*,* **2015**, *137*(35),11445-11452.

170. Dong, H.; Ran, C.; Gao, W.; Sun, N.; Liu, X.; Xia, Y.; Chen, Y. and Huang, W. Crystallization dynamics of Sn-based perovskite thin films: Toward efficient and stable photovoltaic devices. *Adv. Energy Mater.,* **2022**, *12*(1), 2102213.

171. Zhang, Z.; Liang, J.; Zheng, Y.; Wu, X.; Wang, J.; Huang, Y.; Yang, Y.; Zhou, Z.; Wang, L.; Kong, L. and Reddy, K.M. Balancing crystallization rate in a mixed Sn–Pb perovskite film for efficient and stable perovskite solar cells of more than 20% efficiency. *J. Mater. Chem. A,* **2021**, *9*(33), 17830-17840.

172. Xiao, L.; An, T.; Deng, C.; Xu, X. and Sun, H. On biosafety of Sn-containing halide perovskites. Energy Environ. Sci., **2023**, 16(5), 2120-2132.

173. Lanzetta, L.; Webb, T.; Zibouche, N.; Liang, X.; Ding, D.; Min, G.; Westbrook, R. J. E.; Gaggio, B.; Macdonald, T. J.; Islam, M. S. and Haque, S.A. Degradation mechanism of hybrid tin-based perovskite solar cells and the critical role of tin (IV) iodide. *Nat. Commun.,* **2021**, 12 (1), 2853.

174. Correa-Baena, J.-P.; Saliba, M.; Buonassisi, T.; Grätzel, M.; Abate, A.; Tress, W. and Hagfeldt, A. Promises and challenges of perovskite solar cells. Science, **2017**, 358 (6364), 739−744.

175. Lee, H.; Kang, S.B.; Lee, S.; Zhu, K. and Kim D.H. Progress and outlook of Sn–Pb mixed perovskite solar cells. Nano Converg.*,* **2023**, *10*(1), 27.

176. Goyal, A.; McKechnie, S.; Pashov, D.; Tumas, W.; van Schilfgaarde, M. and Stevanović, V. Origin of Pronounced Nonlinear Band Gap Behavior in Lead–Tin Hybrid Perovskite Alloys. *Chem. Mater.,* **2018**, *30* (11), 3920-3928.

177. Im, J.; Stoumpos, C. C.; Jin, H.; Freeman, A.J. and Kanatzidis, M.G. Antagonism between Spin–Orbit Coupling and Steric Effects Causes Anomalous Band Gap Evolution in the Perovskite Photovoltaic Materials CH3NH3Sn1–xPbxI3. *J. Phys. Chem. Lett.,* **2015**, *6* (17), 3503-3509.

178. Farrar, M.D. Improving the performance and reproducibility of lead-tin perovskite absorbers toward all-perovskite tandem solar cells, **2022** (Doctoral dissertation, University of Oxford).

179. Yu, Y.; Zhang, F.; Hou, T.; Sun, X.; Yu, H. and Zhang, M. A Review on Gas-Quenching Technique for Efficient Perovskite Solar Cells. *Solar Rrl*, **2021***,* 5(10),2100386.

180. Li, T.; Ma, F.; Hao, Y.; Wu, H.; Zhu, P.; Li, Z.; Li, F.; Yu, J.; Liu, M.; Lei, C. and Liang, T. Defect Passivation for Highly Efficient and Stable Sn-Pb Perovskite Solar Cells. *Crystals,* **2024**, *14*(9), 802.

181 . Byranvand, M.M.; Zuo, W.; Imani, R.; Pazoki, M. and Saliba, M. Tin-based halide perovskite materials: properties and applications. *Chem. Sci.,* **2022**, *13*(23), 6766-6781.

182. Yang, X.; Ma, T.; Hu, H.; Ye, W.; Li, X.; Li, M.; Zhang, A.; Ge, C.; Sun, X.; Zhu, Y. and Yan, S. Understanding and manipulating the crystallization of Sn–Pb perovskites for efficient all-perovskite tandem solar cells. Nat. Photonics*,* **2025**,1-8.

183. Li, C.; Zhu, M.; Jiang, H.; Zhang, S.; Cheng, J.; Cao, H.; Wang, T. and Zhou, Z. Multiple active site additive-mediated suppression of Sn 2+ oxidation and regulation of crystallization for high-performance Sn–Pb mixed perovskite solar cells. Mater. Horiz.*,* **2025,** *12*(13), 4813-4821.

184. Solis, O.E.; Mínguez-Avellán, M.; Betancur, P.F.; Sánchez-Alarcón, R.I.; Rodriguez, I.; Martínez-Pastor, J.P.; Ripolles, T.S.; Abargues, R. and Boix, P.P. Adjusting the crystallization of tin perovskites through thiophene additives for improved photovoltaic stability. ACS Energy Lett.*,* **2024**, *9*(11), 5288-5295.

185. Zhang, Z.; Liang, J.; Zheng, Y.; Wu, X.; Wang, J.; Huang, Y.; Yang, Y.; Zhou, Z.; Wang, L.; Kong, L. and Reddy, K.M. Balancing crystallization rate in a mixed Sn–Pb perovskite film for efficient and stable perovskite solar cells of more than 20% efficiency. *J. Mater. Chem. A.,* **2021**, *9*(33), 17830-17840.

186. Chen, J.; Liu, J.; Li, Y.; Xu, P.; Xie, L.; Meng, Y.; Wu, H.; Shang, X.; Zhao, S.; Pan, J. and Xiao, C. Ultrasonic-Assisted Processing Combined with Gas Quenching for Fabricating High-Performance and Stable Inverted Perovskite Solar Cells. *Adv. Funct. Mater,* **2024**, 34(26), 2314652.

187. Tang, S.; Bing, J.; Zheng, J.; Tang, J.; Li, Y.; Mayyas, M.; Cho, Y.; Jones, T.W.; Yang, T.C.J.; Yuan, L. and Tebyetekerwa, M. Complementary bulk and surface passivations for highly efficient perovskite solar cells by gas quenching. Cell Rep. Phys. Sci.*,* **2021**, *2*(8), 100511.

188. Babayigit, A.; D'Haen, J.; Boyen, H.G. and Conings, B. Gas quenching for perovskite thin film deposition. *Joule,* **2018**, *2*(7), 1205-1209.

189. Yu, Y.; Zhang, F.; Hou, T.; Sun, X.; Yu, H. and Zhang, M. A Review on Gas-Quenching Technique for Efficient Perovskite Solar Cells. *Solar Rrl,* **2021**, *5*(10), 2100386.

190. Yang, F.; Jang, D.; Dong, L.; Qiu, S.; Distler, A.; Li, N.; Brabec, C.J. and Egelhaaf, H.J. Upscaling solution-processed perovskite photovoltaics. Adv. Energy Mater.*,* **2021**, *11*(42), 2101973.

191. Werner, J.; Moot, T.; Gossett, T.A.; Gould, I.E.; Palmstrom, A.F.; Wolf, E.J.; Boyd, C.C.; van Hest, M.F.; Luther, J.M.; Berry, J.J. and McGehee, M.D. Improving low-bandgap tin–lead perovskite solar cells via contact engineering and gas quench processing. *ACS Energy Lett.,* **2020**, *5*(4),1215-1223.

192. Hadipour, A. Enhancing gas-quenching method for fabrication of perovskite-based photovoltaics. *Kuwait J. Sci.,* **2025**, *52*(2),100387.

193. Temitmie, Y.A., Azhar, M., Haider, M.I., Yalcinkaya, Y., Schütz, E.R., Mayer, T., Benor, A. and Schmidt-Mende, L., 2025. Gas Quenching-Mediated Crystallization for Optoelectronic-Grade Pb–Sn Perovskite Films. *Solar RRL*, p.e202500713.

194. Conings; Bert; Aslihan Babayigit; Matt Klug; Sai Bai; Nicolas Gauquelin; Nobuya Sakai; Jacob Tse-Wei Wang; Jo Verbeeck; Hans-Gerd Boyen; and Henry Snaith. Getting rid of anti-solvents: gas quenching for high performance perovskite solar cells." In *2018 IEEE 7th World Conference on Photovoltaic Energy Conversion (WCPEC)(A Joint Conference of 45th IEEE PVSC, 28th PVSEC & 34th EU PVSEC)*, **2018**, 1724-1729.

195. Ternes, S.; Laufer, F. and Paetzold, U.W. Modeling and fundamental dynamics of vacuum, gas, and antisolvent quenching for scalable perovskite processes. *Adv. Science,* **2024**, *11*(14), 2308901.

196. Miah, M.H.; Rahman, M.B.; Nur-E-Alam, M.; Islam, M.A.; Shahinuzzaman, M.; Rahman, M.R.; Ullah, M.H. and Khandaker, M.U. Key degradation mechanisms of perovskite solar cells and strategies for enhanced stability: issues and prospects. *RSC advances,* **2025**, *15*(1), 628-654.

197. Nogueira, G.L.; Lopez-Richard, V.; Meneghetti Jr, L.A.; Hartmann, F. and Graeff, C.F. Exploring Charge Transport and Hysteresis Effects in Perovskite Solar Cells Through Dynamic Measurements and Analytical Modeling. *Solar RRL,* **2025**, 202500562.

198. Chen, B.; Yang, M.; Priya, S. and Zhu, K. Origin of J–V hysteresis in perovskite solar cells. *J. Phys. Chem. Lett.,* **2016**, *7*(5), 905-917.

199. Kaczaral, S.C.; Morales, D.A.; Schreiber, S.W.; Martinez, D.; Conley, A.M.; Herath, R.; Eperon, G.E.; Choi, J.J.; McGehee, M.D. and Moore, D.T. Improved reproducibility of metal halide perovskite solar cells via automated gas quenching. *APL Energy*, **2023**, *1*(3), 036112.

200. Butler-Caddle, E.; Jayawardena, K.I.; Wijesekara, A.; Milot, R.L. and Lloyd-Hughes, J. Distinguishing carrier transport and interfacial recombination at perovskite/transport-layer interfaces using ultrafast spectroscopy and numerical simulation. *Phys. Rev. Appl.,* **2024**, *22*(2), 024013.

201. Azhar, M.; Cuzzupè, D.T.; Yalcinkaya, Y.; Haider, M.I.; Schütz, E.R.; Schupp, S.M.; Temitmie, Y.A.; Hooijer, R.; Aydin, E. and Schmidt-Mende, L. Impact of Antisolvent and Gas Quenching on Wrinkling in Cs0. 15FA0. 85Pb (I0. 6Br0. 4) 3 Perovskite Films. *ACS Appl. Mater. Interfaces,* **2025***,* 17, 42, 58501–58511.